

Relative wave measurement concepts for Oksøy/Alta and Skjold class vessels

Sigurd Weidemann Løvseth, Asbjørn Kleivstul and Hans Erling Torkildsen

Forsvarets forskningsinstitutt/Norwegian Defence Research Establishment (FFI)

14 May 2008

FFI-rapport 2008/01029

3467

ISBN 978-82-464-1377-8

Keywords

Havbølger

Skipsbevegelser

Elektrisk ledningsevne

Elektroder

Induksjonspoler

Elektromagnetiske bølger - Forplantning

Radiobølger - Forplantning

Radiodetektorer

Hydrodynamikk

Lidar

Approved by

Hans Erling Torkildsen

Project Manager

Nils Størkersen

Director of Research

John-Mikal Størdal

Director

English Summary

Sudden horizontal decelerations in rough seas due to wave diving/green water on deck may pose a serious risk to crew safety as well as to hull integrity on the new Skjold class fast patrol boats. FFI plans to develop a system for structural health monitoring of the Skjold class, and aims to include tools that could warn the crew when the ship is at risk of getting green water on deck. In the planned project, FFI will analyze data from the inertial navigation system (INS) and, if possible, develop a bow diving warning tool based on the INS. However, it is believed that a sensor that measures the distance between the wet deck and sea surface close to the bow of the ship will increase the quality of such a warning system. Also the hull monitoring system of the Oksøy/Alta class mine sweeper/hunter class will benefit from an accurate relative wave measurement. In a previous report, an evaluation of three commercial instruments based on non-contact microwave and ultrasound technology was described. Unfortunately, none of the evaluated instruments or technologies had the required reliability during rough weather.

In this report, a range of alternative and some novel techniques are evaluated. They utilize the differences in electromagnetic, mechanical, and optical properties between sea water and air to estimate the relative wave height. Most of the techniques considered here are based on distributed or array sensors mounted at different heights in, behind or on the outside of the hull. I.e., the presence of water is assessed locally around the hull-mounted sensor, and by comparing the data from all sensors of the array or the whole distributed sensor string the water level is found.

Of all the considered options discussed in this report, we think five techniques are promising. Since air is an isolator, whereas sea water is electric conductive, the perhaps simplest technique is just to measure the conductivity between two electrodes. Due to the variable conductance of sea water, conductance measurements should be performed over an array of detectors rather than using a single pair of wire running top-down on the outer hull surface. Measurement errors due to water film between the conductors can mostly be avoided by using a sufficiently large distance between the electrodes. This report also suggests some mounting solutions that we believe will be robust enough to overcome the large tear and wear outside the hull close to the bow.

Another consequence of the conductivity of sea water is that an application of time-varying electromagnetic fields will induce eddy currents that in turn will weaken the applied field. This effect is the basis of two promising sensor principles considered here. A well-established technology in other applications is inductive sensors, where the magnetic field set up by the eddy currents is measured and analyzed. Alternatively, in our case, the attenuation of the electromagnetic RF (radio) field as a function of water depth due to the eddy currents can be detected using an antenna array. Although several induction sensor designs are suggested in this report, we believe that characterization of the radio attenuation profile has the largest potential, since it requires the weakest field and can use a simpler antenna design.

The fourth promising, but rather obvious, technique for the measurement of the relative wave considered here is the use of a pressure sensor array. Pressure sensor technology is quite mature, and small, robust sensors with a large dynamic range are available. This report gives a few examples of how the sensors could be mounted in a robust manner

Finally, it is probably possible to map the waves in front of the ship in a very detailed manner using a pulsed laser with beam scanning. However, the development and probably also hardware of such a system would probably be too expensive for the given application

We recommend that the next step in the development of a relative wave measurement is realistic on-ship prototype trials of the conductance, the radio antenna, or the pressure sensor array. The apparent advantage of the pressure and conductance sensor array is that the technologies are proven, but mechanical robustness and the effect of splashing waves etc. have to be studied in a realistic test. For the radio antenna, the big advantage is that the whole sensor system can be placed inside the ship, but the technology itself has to be proven. If the prototypes are made simple enough, it could also be a possibility to test more than one principle simultaneously. Probably, the same holes can be used both for the pressure and conductance sensors.

Sammendrag

På de nye MTB-fartøyene i Skjold-klassen kan grønn sjø på dekk føre til brå nedbremsing og utgjøre en trussel mot mannskapets sikkerhet og skrogets integritet. FFI planlegger å utvikle et skrogovervåknings-system for Skjold-klassen, og tar sikte på å inkludere verktøy som kan varsle mannskapet når det er risiko for å få grønn sjø på dekk. I det planlagte prosjektet, vil FFI analysere data fra treghetsnavigasjonssystemet (INS) og, hvis mulig, utvikle et varslingsystem mot baugdykking basert på INS. Det er imidlertid sannsynlig at en sensor som kan måle avstanden mellom våtdekket og sjøoverflaten forut vil øke ytelsen på et slikt varslingsystem. Også skrogovervåkningssystemet som utvikles for Oksøy/Alta-klassen vil kunne gi bedre varsler om det suppleres med en slik sensor. En tidligere rapport ga en evaluering av kommersielt tilgjengelige ultralyd- og mikrobølgealtimeter. Dessverre viste det seg at ingen av instrumentene eller teknologiene var til å stole på for vårt bruk.

I denne rapporten blir en rekke alternative og noen nye måleideer diskutert. De utnytter forskjeller i de elektromagnetiske, optiske og mekaniske egenskapene mellom luft og sjøvann. Flesteparten av teknikkene som er blitt overveid baserer seg på distribuerte eller en rekke sensorer montert på forskjellige høyder bak, i eller på utsiden av skrogplatene. Tilstedeværelsen av vann blir målt lokalt rundt sensoren, og ved å sammenligne data fra alle enkeltsensorene i rekken, evt. fra den distribuerte sensoren, finnes vannivået på skroget.

Av alle de forskjellige teknikkene som er diskutert i denne rapporten, synes vi fem er lovende. Siden luft er en isolator, mens sjøvann er elektrisk ledende, er kanskje den enkleste teknikken å bare måle strømmen mellom to spenningsatte elektroder. Selv om en kunne tenke seg å bare bruke ett trådpar langs skutesiden, bør man bruke en rekke sensorpar siden ledningsevnen til saltvann er sterkt varierende. Selv om en tynn sjøvannsfilm mellom elektrodene også vil være svakt ledende, kan dette problemet stort sett unngås ved å ha stor nok avstand mellom elektrodene. Denne rapporten foreslår også monteringsmetoder som vi tror vil være robuste nok mot den store påkjenningen sensorene vil utsettes for utenfor skroget nær baugen.

En annen konsekvens av sjøvannets ledningsevne er at et tidsvarierende elektromagnetisk felt vil sette opp virvelstrømmer og tilhørende motfelt som vil svekke det opprinnelige påførte feltet. Denne effekten er grunnlaget for to lovende teknikker. Såkalte induktive sensorer brukes i en rekke anvendelser, og er basert på å måle og analysere motfeltet som blir induisert i en leder. I vårt tilfelle kan man alternativt måle svekningen av et utsendt elektromagnetisk RF (radio) felt ved hjelp av en antennerække. Selv om mange forskjellige induktive sensorutformninger blir foreslått i denne rapporten, tror vi at måling av radiosignalers dempningskarakteristikk er mest attraktiv. I forhold til induktive teknikker kreves svakere felt og enklere antenner kan brukes.

Den fjerde lovende, man ganske innlysende, metoden å måle relativbølger på er å benytte en rekke med trykksensorer. En fordel er at små men robuste trykksensorer med stor dynamikk basert på moden teknologi er kommersielt tilgjengelige. Rapporten gir noen eksempler på hvordan trykksensorene kan bli montert på en robust måte.

Til slutt vil det også være mulig å måle en detaljert bølgeprofil foran skipet ved å bruke en pulset laser med strålesveiping. Vi tror imidlertid at både utviklings- og komponentkostnadene for et slikt system vil være for høy for den noe spesielle problemet vi ønsker å løse.

Vi anbefaler at det neste steget i utviklingen av relativbølgemålingsutstyr er en realistisk test av en enkel motstandsmåler-, radioantenne- eller trykksensorrekke langs skutesiden på et av de aktuelle skipene. En fordel med trykk- eller motstandsmåling er at teknikkene er veletablerte på andre områder, men mekanisk robusthet og virkningen av sjøsprøyt etc. må studeres i en realistisk test. Den store fordelen med radiomåling er at alle delene av systemet kan plasseres på innsiden av skroget, men vi må også få bekreftet at teknikken virker i praksis. Hvis prototypene blir laget enkle nok, kan man kanskje også teste flere alternativ samtidig. Sannsynligvis kan man da bruke de samme skroghullene for både trykk- og konduktansmåling.

Contents

1	Introduction	7
2	Electromagnetic Techniques	10
2.1	Conductance Sensors	10
2.1.1	Operating Principle and Theoretical Considerations	10
2.1.2	Hardware Configurations	20
2.2	Inductance Sensors	24
2.2.1	Analyzed IB configurations	25
2.2.2	Theoretical Considerations	27
2.2.3	Experiments	47
2.2.4	Concluding Remarks Regarding Inductive Techniques	50
2.3	Capacitive Techniques	50
2.3.1	Operating Principle and Theoretical Considerations	50
2.3.2	Experiments	52
2.4	Radio Attenuation Detection Array	55
2.4.1	Concept and Theoretical Considerations	55
2.4.2	Experimental Investigations	83
2.4.3	Signature of the proposed sensor system	83
2.4.4	Alternative Configurations	84
2.4.5	Conclusions Regarding Radio Attenuation Detection Array	84
2.5	Directive RF/microwave reflectivity sensor	84
3	Techniques based on static and acoustic pressure	86
3.1	Pressure sensor array	86
3.2	Subsurface acoustic techniques	89
4	Optical techniques	89
4.1	Reflectivity sensor	89
4.2	Lidar	92
4.3	Triangulation	93
4.3.1	Triangulation above surface	93
4.3.2	Triangulation below surface	94
5	Conclusions	94
	References	95

1 Introduction

The Royal Norwegian Navy is currently renewing their fast patrol boat fleet, and the new Skjold class will offer stealth properties and velocity that are currently unprecedented. The ship will be equipped with a fiber optic structural health monitoring system. Due to the design and high velocity of the ship, possible wave diving is a threat to safety as well as hull integrity.

In order to predict, and thus avoid, unwanted diving events, it could be necessary to continuously measure the distance between the front portion of the wet deck and the sea surface. One of the main objectives of FFI Oppdrag 3467 has been to investigate the feasibility of including such a sensor in the structural health monitoring systems of both the Oksøy/Alta class and Skjold class vessels.

In reference [1], several commercial sensors were investigated based on ultrasound and microwave techniques. These instruments were to be mounted at the bow of the vessels. Unfortunately, none of the commercial available systems provided the desired degree of reliable measurements, especially in difficult weather. Further, robustness of both the microwave and ultrasound altimeters was an issue.

In this report, the further effort in FFI Oppdrag 3467 to come up with, analyze, and in some instances make preliminary experiments of new concepts for relative wave measurement is documented. In the report, the various techniques are divided up according to which of the physical property of sea water is utilized to divide between air and water, since sea water has markedly different electromagnetic, mechanical and optical properties than air.

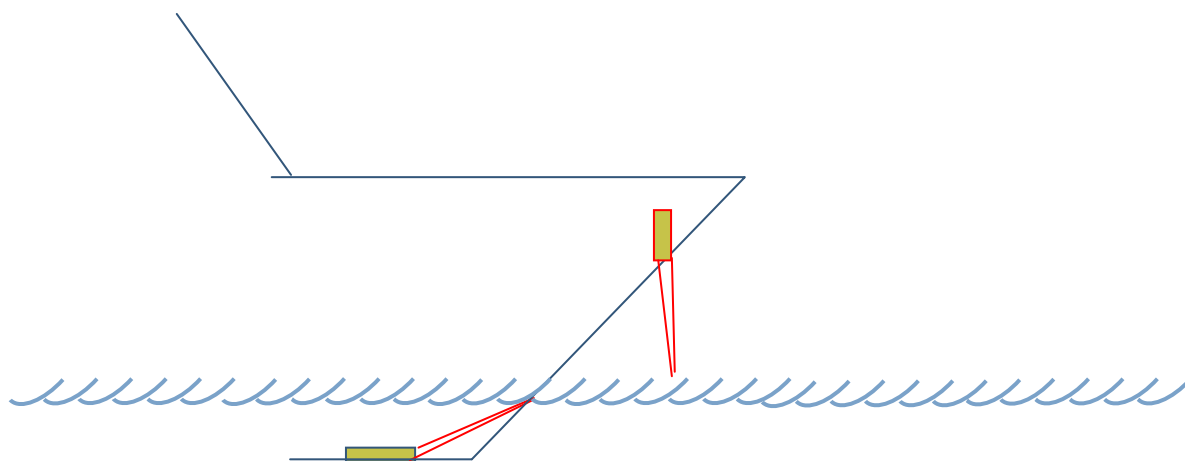


Figure 1.1 Time of flight technique

Across the sections of this report, there are two or three principle methods of measuring the relative wave height. The method utilized in the commercial instruments tested earlier in the project, have all been some flavor of time-of-flight. In this case, a beam of some sort is directed towards the sea surface, and with the hope that some of the beam is reflected back to a nearby

receiver. The roundtrip time, and hence distance, is measured using either fast electronics or some kind of interferometric or mixing technique. Possible pitfalls of this method is, as discussed in reference [1], are that beam is blocked for instance by sea spray, that the reflectance of the water surface is low, or that the beam is reflected away from the receiver due to the inclination of the sea surface. As illustrated in Figure 1.1, the beam in a time-of-flight instrument can also be directed against the sea surface from below, in which case for instance sea spray disturbance in most cases will cease to be a problem.

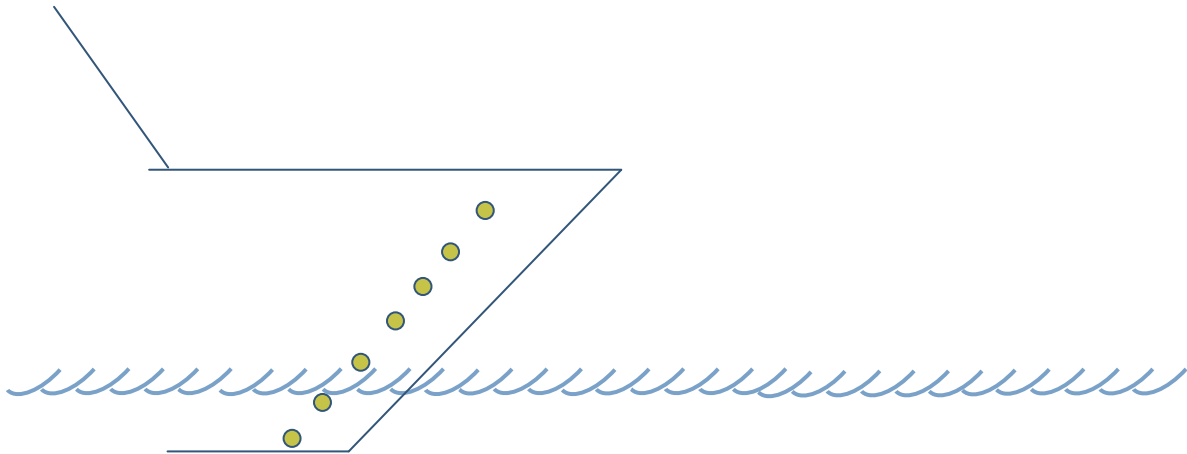


Figure 1.2 An array of discrete, hull-mounted sensors

A majority of the sensors principles of this report work in a quite different mode. Rather than measuring the distance with a single sensor, the relative wave height is deduced from a distributed measurement of the local environment along the hull, or by an array of discrete sensors as illustrated in Figure 1.2. In this case we are no longer dependent on a clean reflected surface, however, sea spray, bow wave or water film on the hull might still impair the quality of the measurement.

As illustrated in Figure 1.3, such sensors can either be placed in front of the bow, or just behind the sacrificial bow, either at the inside or outside of the hull. Placement at the front of the bow is advantageous because the bow wave would make minimal disturbance here, but a placement here would be difficult with most of the techniques discussed in this document. Placing sensor arrays or a distributed sensor along both bows of the vessels would increase reliability and give a more detailed measurement, but might not be required. A suggested distribution of a discrete or semi-discrete sensor array is given in Table 1.1

Table 1.1 Suggested discrete or semidiscrete relative wave sensor distribution

Description	Height over base line		Sensor interval	Number of sensors
	Oksøy/Alta	Skjold		
Base line	< 2.6 m	< 2.5 m	0.5 – 1.0 m	2 – 5
Below wet deck - 0.5 m				
Wet deck in front of the bow	2.6 – 4.0 m	2.5 – 3.9 m	0.1 – 0.3 m	4 – 14
Top of the bow	4.0 – 6.0 m	4.0 – 5.8 m	0.5 – 1.0 m	2 – 3
Total number of sensors				8 – 22

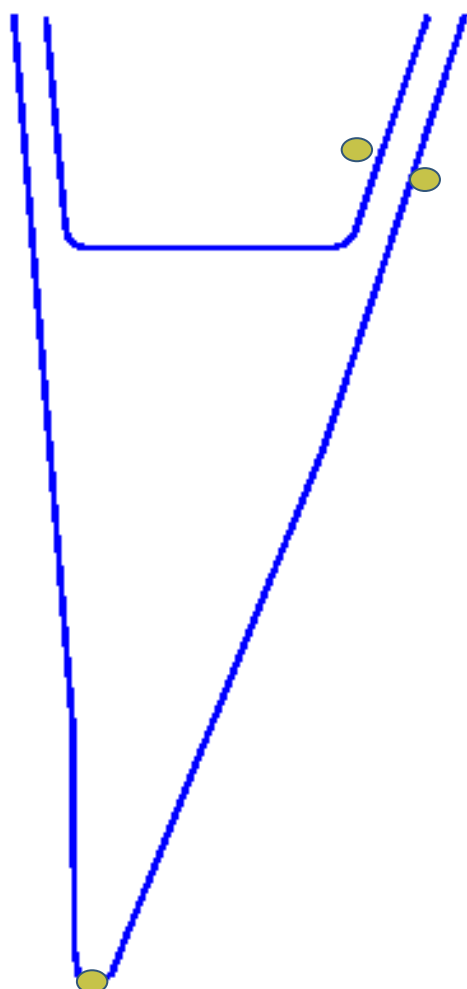


Figure 1.3 Possible placement of distributed or discrete relative wave height sensors.

The current plan for the new Skjold class hull monitoring FFI project does not include a relative wave measurement due to the cost involved in developing such a sensor. Instead the new project will attempt to develop a warning system against bow diving based on analyzing data from the existing inertial navigation system (INS). However, there is currently no guarantee that this

approach will succeed, and it may be necessary during the project to reconsider the ideas presented in this report.

2 Electromagnetic Techniques

The conductivity of sea water is of the order of 4 S/m, while air is an insulator except at very high (ionizing) field strengths. This aim of all the techniques based in this section is to utilize this difference in conductivity to measure the relative wave height close to the bow of the vessel.

At the bottom of the keel a high resolution is probably not required; however around the wet deck a higher resolution is needed. When the relative wave is above the wet deck at the bow, but below the top of the bow, a notable negative acceleration can probably be detected by the INS, and probably a lower density of relative wave sensors are needed. Some of the sensors suggested below will not only detect whether or not there are water outside the sensing point, but also to some degree the water level. In these semidiscrete cases, the distance between the sensors can be somewhat larger.

2.1 Conductance Sensors

2.1.1 Operating Principle and Theoretical Considerations

The principle behind this sensor is simply to measure the conductance between two points outside the hull by using two electrodes and measuring the current (i.e. conductance) that runs between them. At 10 °C and a salinity of 3.5 % (weight), the conductivity of sea water is 3.8 S/m. However, the conductivity is roughly proportional to salt content, and is also almost two times larger at 25 °C than at 0 °C. A standard table of electrical conductivity of sea water can be found here [2]. However, both the salinity and temperature typically varies a lot both from place to place and with depth in the coastal areas the Skjold and Oksøy/Alta class will operate. Perhaps the extreme conductivity values can be found in the Persian Gulf and the Gulf of Bothnia. In some bays of the Persian Gulf can have a salinity of up to 4.4 % and have a water temperature up to 34 °C, yielding a conductivity of roughly 7.75 S/m, i. e. twice the normal value. In the Gulf of Bothnia, on the other hand, the salinity of the northernmost part can be down to 0.3 %, and with a surface temperature of 0 °C, the conductivity value is as low as 0.26 S/m. Worse even, both salinity and temperature is expected to vary with water depth.

Thus, the probably simplest configuration, using a single pair of wire electrodes from the top to the bottom of the hull, will be difficult to calibrate. Instead, we propose to use several point electrodes (i.e. discrete sensors), or several shorter wires (i.e. semidiscrete sensors). Possible configurations will be discussed in Subsection 2.1.2.2. Even though we probably will not use a single pair of electrodes, we have investigated this case theoretically, since the main results for this simplest case also are applicable for more advanced electrode configurations.

2.1.1.1 Analysis of single parallel pair wire electrode conductance sensors

In this case, you have a pair of parallel wires going along the hull from somewhere around the top of the bow down to a point close to the bottom of the keel. The conductance between the wires can be measured by applying a potential difference between the two wires, for instance from their top end. Then there will run current between the parts of the wires that are immersed in sea water, whereas there will be little current between the wires above the water surface. Also here there could be finite current, though, due to for instance a thin sea water film on the hull surface between the wires.

Calculating the current running through and between the wires means solving an electromagnetic problem involving the conductivity of the sea water, σ_{sw} , the thickness of the water film above surface, t , the distance between the wires, d , the wire diameter (assuming they are circular), r , the length of wires running along the hull, L , the height of the water surface on the wires, h , and the conductivity of the metal wires, σ_M . These quantities are illustrated in Figure 2.1.

In general, this is a problem with no analytical solution. However, A solution can be found by idealizing the problem, assuming:

- σ_{sw} is uniform and constant
- σ_M is independent of height
- $\sigma_M \gg \sigma_{sw}$
- t is uniform above the water surface ($z > h$)
- $L \gg d, r_w$
- $T \ll d, r_w$
- $t \ll d$

If we further assume that the wire electrodes are perpendicular to the water surface, the electric field lines running through the water/air will have a negligible vertical (z -) component, i.e. as if the wires were infinite. For two infinitely long wires with opposite surface potential $\pm V_{r_w}$ in a uniform medium, it can be shown that the electric field running between the wires is given by:

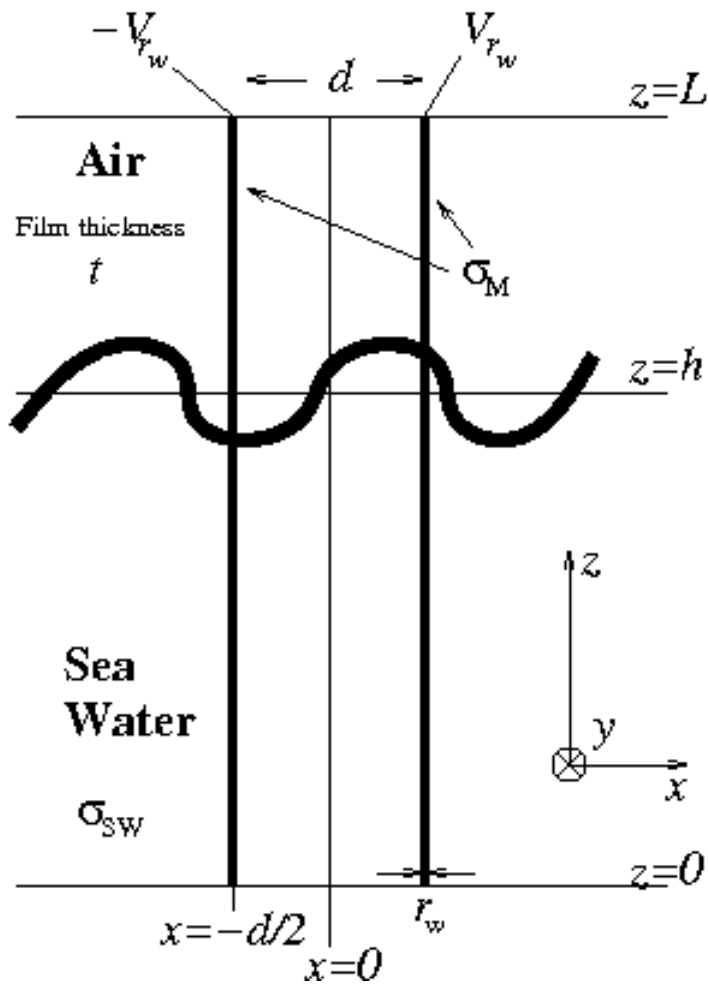


Figure 2.1 Definition of symbols in single pair wire conductance measurement

$$\vec{E} = \frac{V_{r_w}}{\ln\left(\frac{r_w}{d-r_w}\right)} \left\{ \left[\frac{x-d/2}{(x-d/2)^2 + y^2} - \frac{x+d/2}{(x+d/2)^2 + y^2} \right] \hat{x} + y \left[\frac{1}{(x-d/2)^2 + y^2} - \frac{1}{(x+d/2)^2 + y^2} \right] \hat{y} \right\} \quad (2.1)$$

Here the coordinates are defined as in Figure 2.1, i.e. with the wires located in the xz -plane at $x=\pm d/2$, and \hat{x} and \hat{y} are unit vectors in the x and y directions, respectively. In our case, the medium is not uniform around the wires neither below nor above the water surface level $z=h$. However, because sea water is conducting whereas the hull is an isolator, the electric field has to be parallel to the hull close to the hull/sea water interface. In practice, this means that surface charges ensures that equation (2.1) is valid below the water surface. The current per length, $I/\Delta z$, can be found by integrating along a contour around one of the wires in the xz -plane the normal component of the current density \vec{J} . The simplest such contour is along the line $x=0$, i.e.:

$$\begin{aligned}
I_{bw}/\Delta z &= \int_0^{\infty} J_x(x=0) dy = \sigma_{sw} \int_0^{\infty} E_x(x=0) dy = \sigma_{sw} \int_0^{\infty} E_x(x=0) dy \\
&= \frac{\sigma_{sw} V_{r_w} d}{\ln\left(\frac{r_w}{d-r_w}\right)} \int_0^{\infty} \frac{1}{(d/2)^2 + y^2} dy = \frac{\sigma_{sw} V_{r_w} \pi}{\ln\left(\frac{r_w}{d-r_w}\right)}
\end{aligned} \tag{2.2}$$

The conductance per length between the wires below the water surface, $G_{bw}/\Delta z$, can now easily be found:

$$G_{bw}/\Delta z = \frac{|I|}{2V_{r_w} \Delta z} = -\frac{\sigma_{sw} \pi}{2 \ln\left(\frac{r_w}{d-r_w}\right)} \tag{2.3}$$

Above the water surface all conduction takes place in the water film of thickness t . The electric field, the current per length and the conductance per length between the wires above the water surface can easily be found from:

$$\bar{E} = -\frac{2V_{r_w}}{d-2r_w}, \quad -d/2+r_w < x < d/2-r_w \tag{2.4}$$

$$I_{aw}/\Delta z = \int_0^t J_x(x=0) dy = \sigma_{sw} \int_0^t E_x(x=0) dy = -\frac{2\sigma_{sw} V_{r_w} t}{d-r_w} \tag{2.5}$$

$$G_{aw}/\Delta z = \frac{|I|}{2V_{r_w} \Delta z} = \frac{\sigma_{sw} t}{d-r_w} \tag{2.6}$$

Since the conductivity of the wire material is finite, V_{r_w} will generally be spatially varying.

Assuming that the resistivity of the wires is uniform, implying among other things that there is no oxide layer at the surface of the wires, and that $L \gg r_w$, we can find $V_{r_w}(z)$ from the following

criteria:

- I. $V_{r_w}(z)$ is continuous
- II. $V'_{r_w}(z)$ is continuous
- III. $V_{r_w}(L) = V_0$
- IV. $V'_{r_w}(z) = \frac{dV_{r_w}}{dz} = I_w \gamma_w = \frac{I_w}{\pi r_w^2 \sigma_M}$

$I_w(z)$ is the current running through the wires, and is the sum of the currents running between the wires below z . γ_w is the resistance per length of the wire. Since it is assumed that all fields and hence currents are normal to the wires, it follows that $I_w(0) = 0$, and, from criteria IV that $V'_{r_w}(0) = 0$. From equations (2.2) and (2.5) and criteria I - IV it can be deduced that the wire current at the top, $I_w(L)$, and hence the conductance between the wire pairs, G , is given by:

$$G = \frac{I_w(L)}{2V_0} = \frac{k_{aw}}{2\gamma_w} \times \frac{k_{bw} \tanh k_{bw} h \cosh k_{aw} (L-h) + k_{aw} \sinh k_{aw} (L-h)}{k_{aw} \cosh k_{aw} (L-h) + k_{bw} \tanh k_{bw} h \sinh k_{aw} (L-h)}, \tag{2.7}$$

where

$$k_{bw} = \sqrt{\frac{\sigma_{sw} \pi \gamma_w}{-\ln\left[r_w/(d-r_w)\right]}}, \tag{2.8}$$

$$k_{aw} = \sqrt{\frac{2\sigma_{sw}\gamma_w t}{d - r_w}}. \quad (2.9)$$

It would be beyond the scope of this text to give a detailed derivation of equation (2.7). When $k_{aw} \ll k_{bw}$, which it will be if $t \ll d$, and $k_{aw}(L-h) \ll 1$, G is approximately given by:

$$G \approx \frac{1}{2\gamma_w} \times \frac{k_{bw} \tanh k_{bw} h + k_{aw}(L-h)}{1 + k_{bw}(L-h) \tanh k_{bw} h}. \quad (2.10)$$

When there is no water film present, i.e. $t = k_{aw} = 0$; we get:

$$G_0 = \frac{1}{2\gamma_w} \times \frac{k_{bw} \tanh k_{bw} h}{1 + k_{bw}(L-h) \tanh k_{bw} h}. \quad (2.11)$$

When $k_{aw}(L-h)$ and $k_{bw}h$ both are small, i. e. when the resistance of the wires is not significant, the conductance of the sensor is approximately given by:

$$G \approx \frac{hk_{bw}^2 + (L-h)k_{aw}^2}{2\gamma_w}. \quad (2.12)$$

Thus, when additionally $k_{aw} \ll k_{bw}$ the conductance is proportional to the length of wire immersed in water, h , as one would intuitively expect.

2.1.1.2 Estimation of water surface height h

The system has no a priori knowledge of the water film thickness t and thus k_{aw} . In theory it may be possible to measure k_{bw} using a reference sensor, although this is probably difficult in practice due to variation in water temperature and electrode corrosion. During the remainder of this subsection, we will estimate the response of a system that assumes that k_{aw} is zero, and measures k_{bw} . Then an estimate can be calculated from equation (2.11) assuming:

$$G_{meas}(h) \approx G_0(h_{meas}) \quad (2.13)$$

where G_{meas} is the measured conductance, and h_{meas} is the measured/estimated value of h from equation (2.11). Equation (2.13) can be solved using numerical techniques. It is clear that this method will lead to an overestimation of h_{meas} with the presence of a finite water layer/film between the wires above the water surface.

In the following, we will evaluate impact of the different parameters that affect the conductivity on the accuracy of the assumption (2.13). The conductivity can be estimated from equation (2.10) for a given set of parameters, and we define difference between the measured and actual water level:

$$\Delta h = h_{meas} - h \quad (2.14)$$

as a figure of merit for the sensor. Unless otherwise specified, the parameter values given in Table 2.1.

Table 2.1 Default parameters used in the calculations used to produce figures Figure 2.1-
Figure 2.8

Parameter	Value	Comment
σ_M	62.9 MS/m	Conductivity of pure silver
σ_{SW}	3.8 S/m	Conductivity at 10 °C and 3.5 % salinity
D	0.3 m	Wire separation
r_w	3 mm	Wire radius
t	1 mm	Water film thickness
h_{ref}	4 m	Reference height

In Figure 2.2, the conductance G is plotted as a function of h for different values of the water thickness t . For the parameters used here, we see that conductance is roughly a linear function of h , which that the regime where the wire resistance γ_w is negligible and the approximation of equation (2.12) is valid. The conductance between the wires is roughly 1.7 S/m, which can be read directly from the curves with small t . As t becomes comparable and larger than the wire radius $r_w=3$ mm, the validity of equations (2.4)-(2.6) is questionable as the real conductivity of the water layer would be limited by the contact area with the wire. Both in this and later graphs, however, we have not allowed $I_{aw}/\Delta z$ to become larger than $I_{bw}/\Delta z$, hence the horizontal curve for $t=0.1$ m.

In Figure 2.3, Δh is plotted as a function of h and h_{meas} for different values of t . Since $\Delta h(h_{meas})$ is nonzero at $h=0$ for finite values of t , the curves of $\Delta h(h_{meas})$ will not go all the way to $h_{meas}=0$, and will always be above the corresponding $\Delta h(h)$ -curve. The height where the wet deck meets the bow plate (about $h=4$ m), we call the reference height h_{ref} . At $h=h_{ref}$ we probably need our relative wave measurement to be most accurate, probably around 0.1 to 0.2 m. Figure 2.3 indicates that with the chosen parameters, you can allow a water film thickness between 1 and 3 mm to reach this goal.

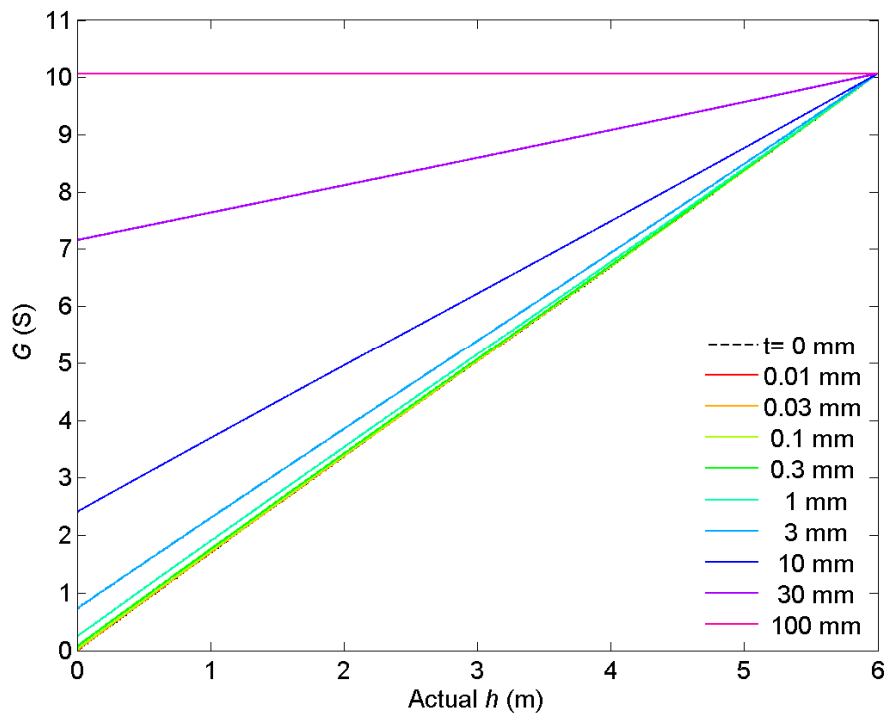


Figure 2.2 Estimated conductance G as a function of water surface height, h , for different values of water film thickness t above the water surface. Other parameters are defined in Table 2.1.

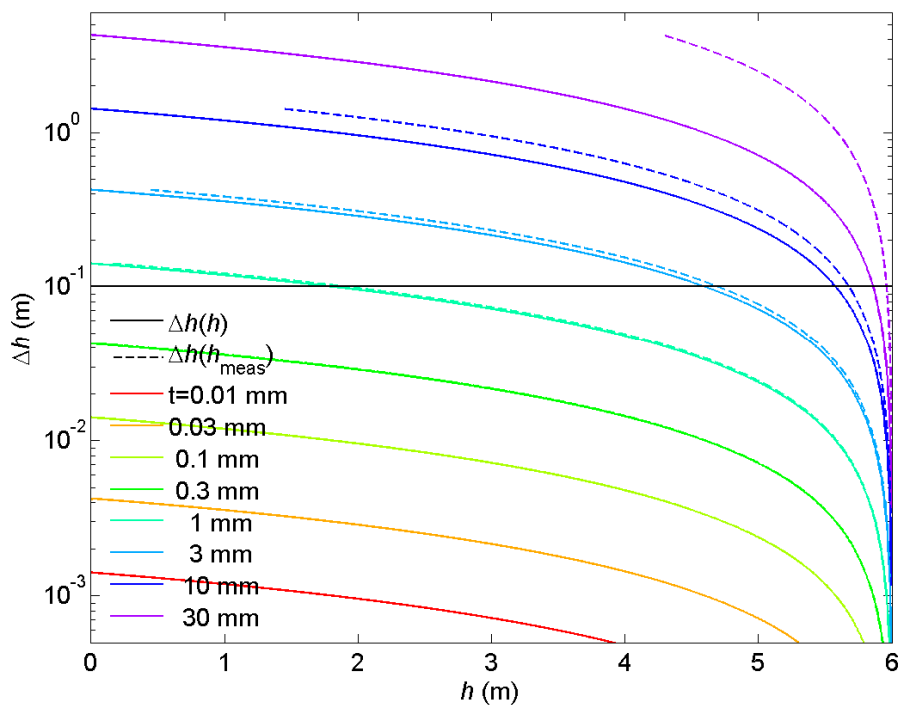


Figure 2.3 Difference Δh between measured, h_{meas} , and actual, h , value of water surface height as a function of both h and h_{meas} for different values of water film thickness t . Other parameters are defined in Table 2.1.

In Figure 2.4, Δh is plotted as a function of t for different values of the wire separation d and for h and h_{meas} equal to h_{ref} . From the graph, it is evident that increasing d is advantageous in order to decrease the sensitivity to sea water between the wires above the water surface level, and hence decrease the error Δh . The reason is that while the resistance of the sheet resistance from equation (2.6) increases proportionally to the wire separation d , the bulk water resistance increases only weakly with d from equation (2.3). The reason is that in the latter case, the field lines are allowed to spread over a larger volume as d increases. From the figure, it seems like an accuracy of $\Delta h=0.1$ m is achievable with 5 cm separation for $t=1$ mm. For larger separations the accuracy becomes even better, but we used $d=0.3$ m in the other calculations since there in practice there will be space limitations in the bow and d must be of the same order as the required

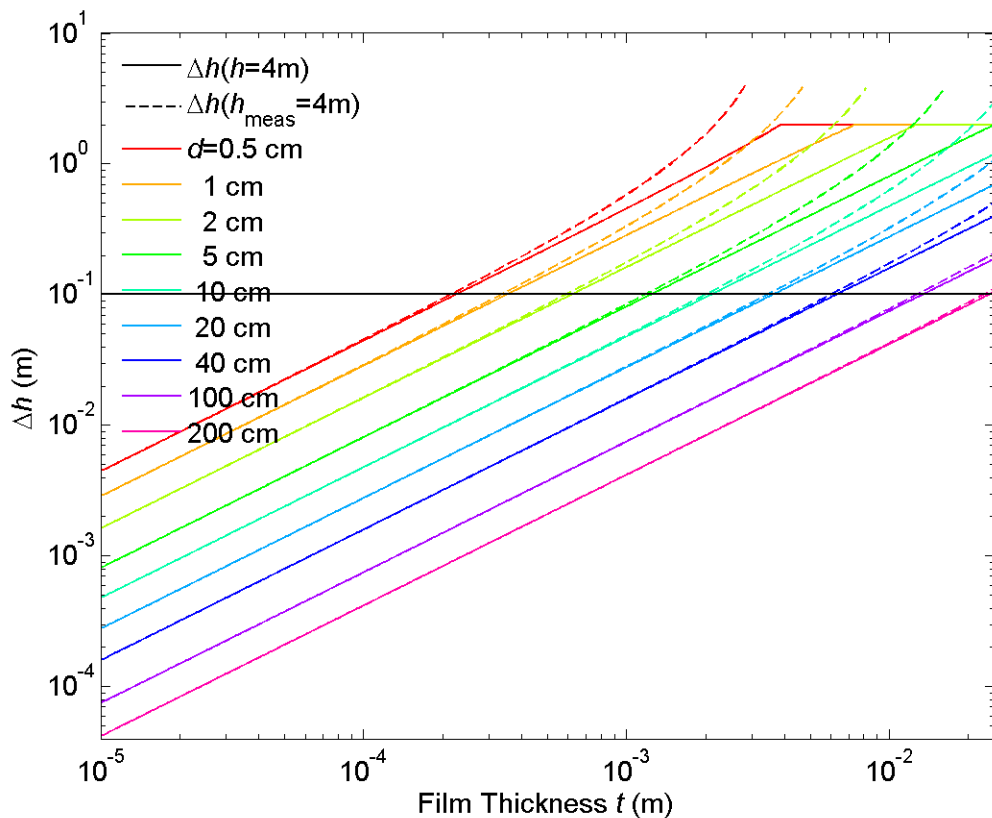


Figure 2.4 Δh as a function of t for different values of the wire separation d and at $h=4$ m and $h_{meas}=4$ m. Other parameters are defined in Table 2.1.

resolution. In order to get meaningful results for the other parameter, we should also keep within the assumption $L \gg d$ of the theoretical model.

Silver is probably a good choice as an electrode material in the sea because it is quiet resistant to corrosion. In addition silver is the metal with the highest electrical conductivity. In Figure 2.5, the estimated wire pair conductance G is plotted as a function of h for different materials with $t=1$ mm and $h=0$. The metals/alloys are chosen among those that are proven to be reasonably resistant to corrosion. Gold, copper and silver, all quite good conductors, all have a fairly linear response, whereas some of the other metals don't. However, as shown in Figure 2.6, where Δh for the different materials is plotted at $h=h_{ref}$ and $h_{meas}=h_{ref}$, the differences in conductance is not

that important for the sensor resolution, and the difference in conductance can be compensated by increasing the wire radius r_w somewhat. The corresponding dependence of Δh on r_w is shown in Figure 2.7.

Finally, the dependence of Δh on sea water conductivity σ_{sw} is shown in Figure 2.8. This appears to be not critical at all. However, one should bear in mind that we have assumed that we know the exact value of σ_{sw} , and that it is uniform. Neither is probably true in practice. Also, in order to cope with varying sea water conductance equipment with large dynamical range is needed.

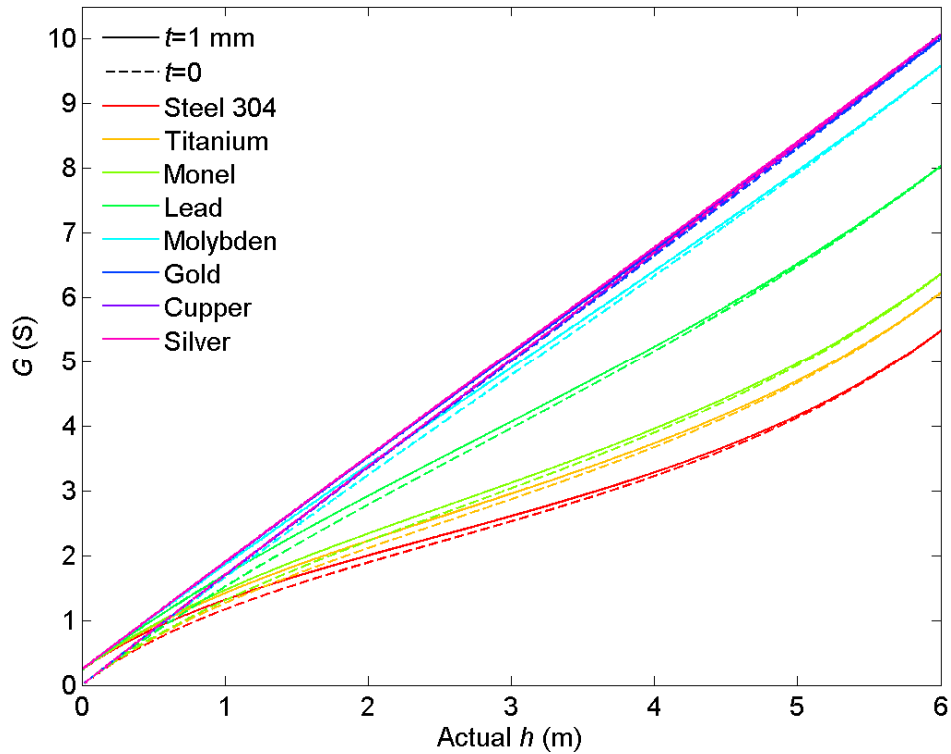


Figure 2.5 Conductivity between wire electrodes as a function of h for different wire electrode materials and for $t=1$ and 0 mm.

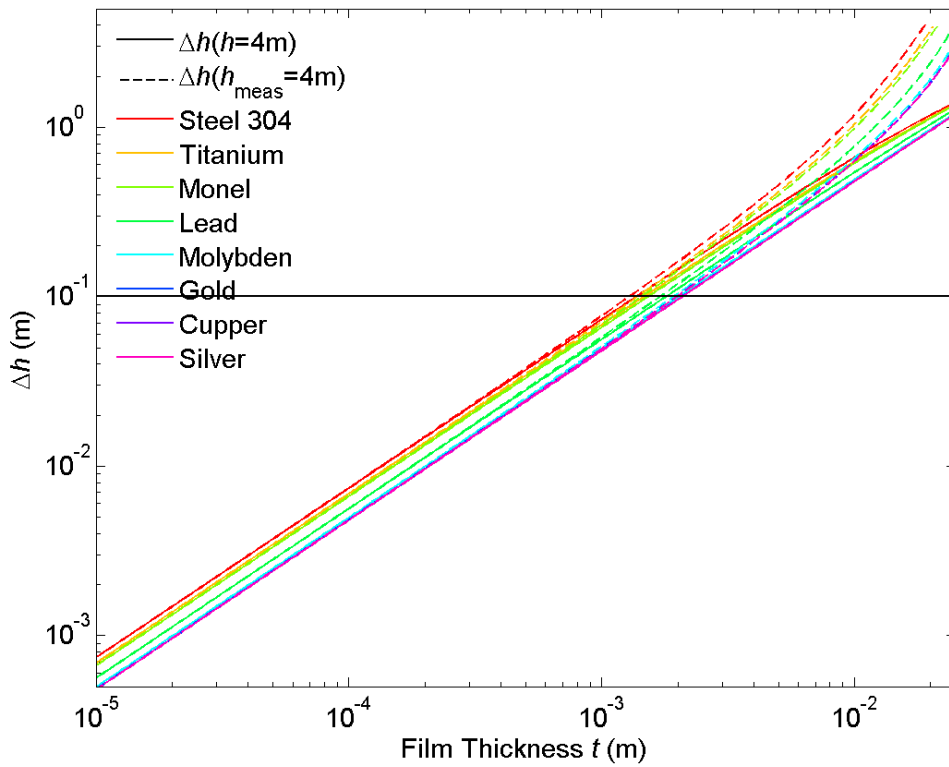


Figure 2.6 As Figure 2.4, but for different wire electrode material.

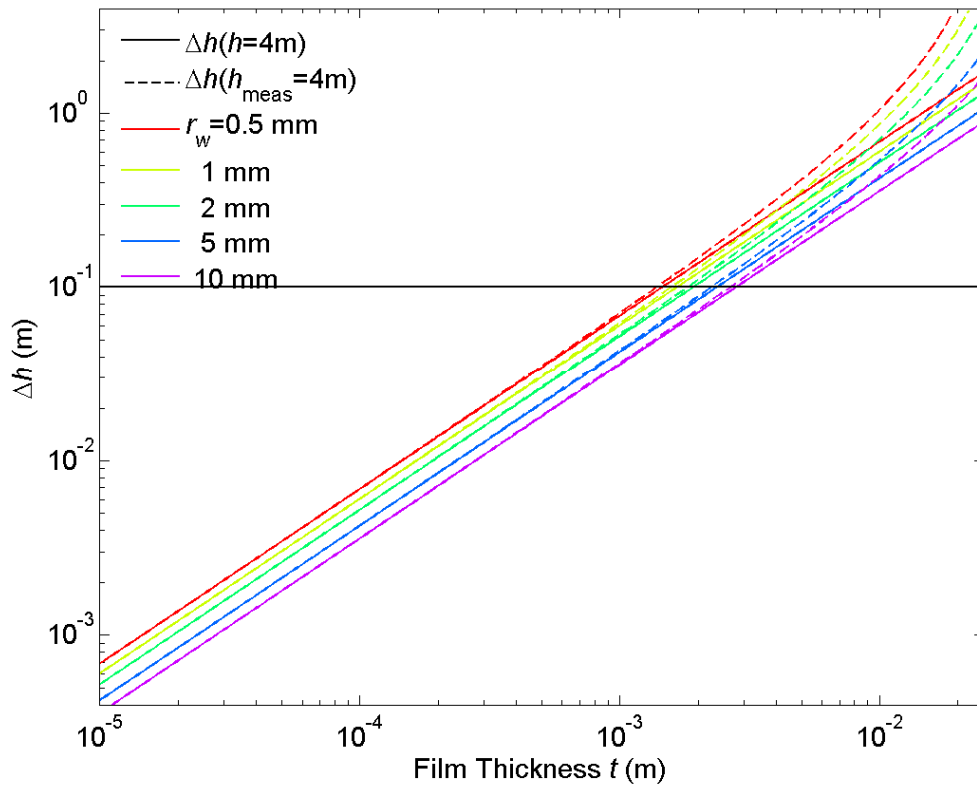


Figure 2.7 As Figure 2.4, but for different wire radius r_w .

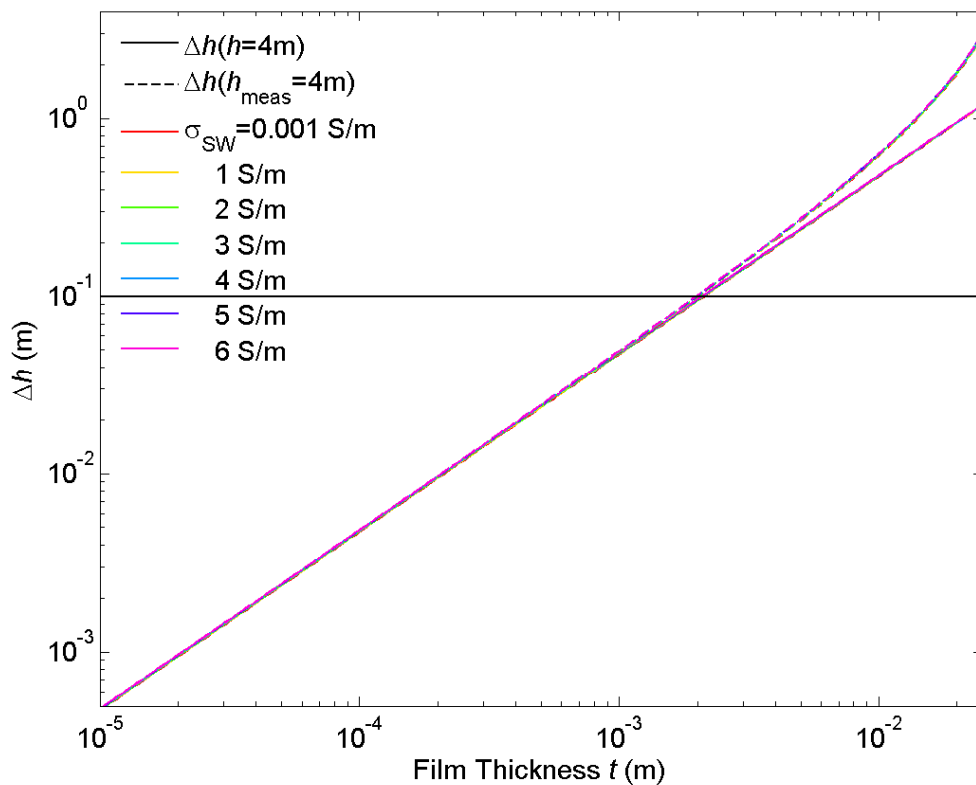


Figure 2.8 As Figure 2.4, but for different sea water conductance σ_{SW} .

2.1.2 Hardware Configurations

2.1.2.1 Choice of Materials and Corrosion Implications

As discussed in Subsection 2.1.1.2, the conductivity of all the considered electrode metals and alloys was sufficient to make good sensors, under the assumption that the materials are in their metallic form. However, most of these metals are in fact base metals, whose main protection against corrosion is based on forming a thin oxide layer. This is the basis of the corrosion resistance of for instance stainless steel, titanium, lead and to some degree copper. A buildup of such oxide layers is undesirable for a conductance measurement, as such oxide layers have large electrical resistance, and thus the conductance measurement can become more unreliable. Further, when used as active electrodes in sea water, this kind of corrosion resistance would be ineffective. Thus, our electrode metal should have high nobility, and we believe that silver is a suitable choice, considering its galvanic and mechanical properties and costs.

Further, we need to ensure that no direct current runs between the electrodes. Otherwise the anode will dissolve in the electrolyte which in this case is sea water. Thus, we need to measure the conductance using alternating current, and to ensure that there is no accidental DC running between the electrodes a capacitor has to be placed between the electrodes in the read-out electronics.

2.1.2.2 Electrode Layout, Design and Mounting

In subsections 2.1.1.1-2.1.1.2, an idealized conductance sensor consisting of two parallel wires running from the weather deck down to the keel, possibly with a reference sensor that measure the conductivity of the sea water. Although simple, such a configuration would probably not result in the desired accuracy and reliability required for the relative wave height measurement. As mentioned above, the temperature and salinity may vary significantly. In addition, oxidation or dirt may in an unpredictable way affect the contact between the electrode and the sea water, and thus cause errors in the measurement of the relative wave height h based on conductance.

In order to become independent of the varying sea water conductivity and contact resistance between the sea water and electrodes, we suggest using several shorter sensors instead of one long wire electrode pair. Even with varying sea water conductivity and electrode state with water depth there will be a clear difference between the conductance of sensors that are above and below the sea water surface. Thus, with minimal processing it will be possible to resolve the water depth h with accuracy equal to the individual separation/length. With more advanced processing, a much higher accuracy can probably be achieved.

In Figure 2.9, a few suggested electrode configurations are shown. In configuration a), the right electrode wire is divided up in several shorter wires, whereas the left electrode is still a continuous, long wire. The water depth is found by comparing the currents of the electrodes on the right side in the processing unit. In configuration b), the left wire is chopped up as well, but by connecting the electrodes of the left side on the dry side of the shell plates, configuration b)

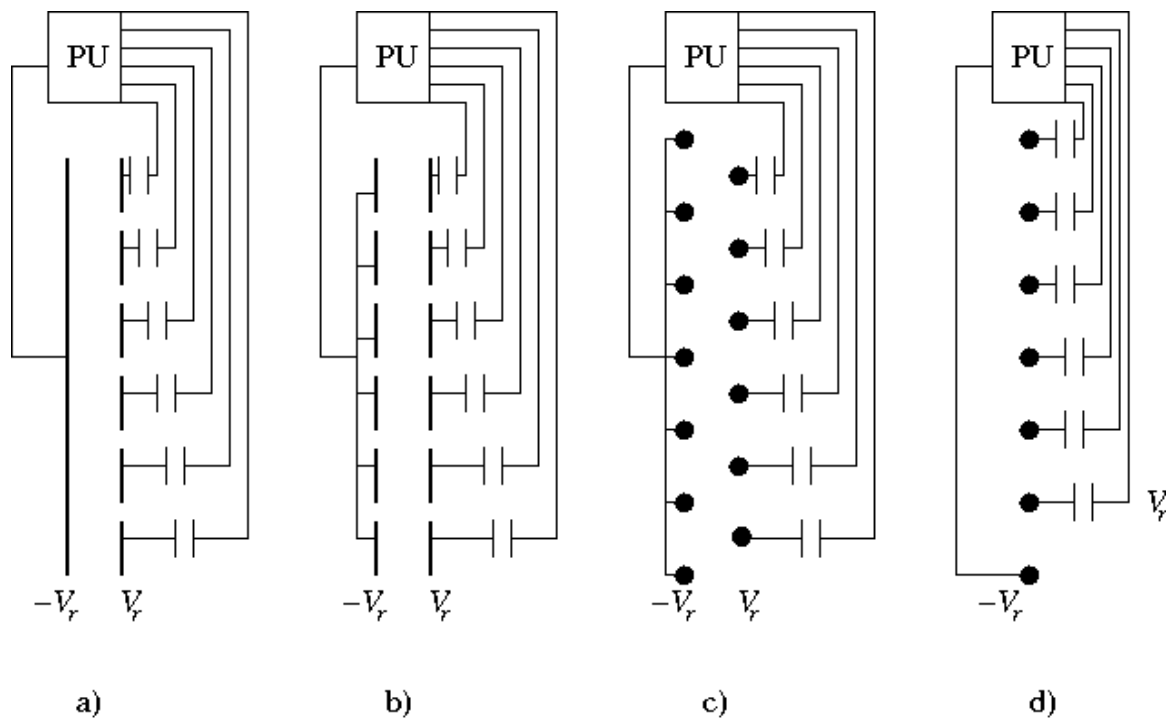


Figure 2.9 Suggested conductance sensor electrode configurations. PU is the sensor processing unit, and thin lines are dry wires which are not part of the conductance sensor head.

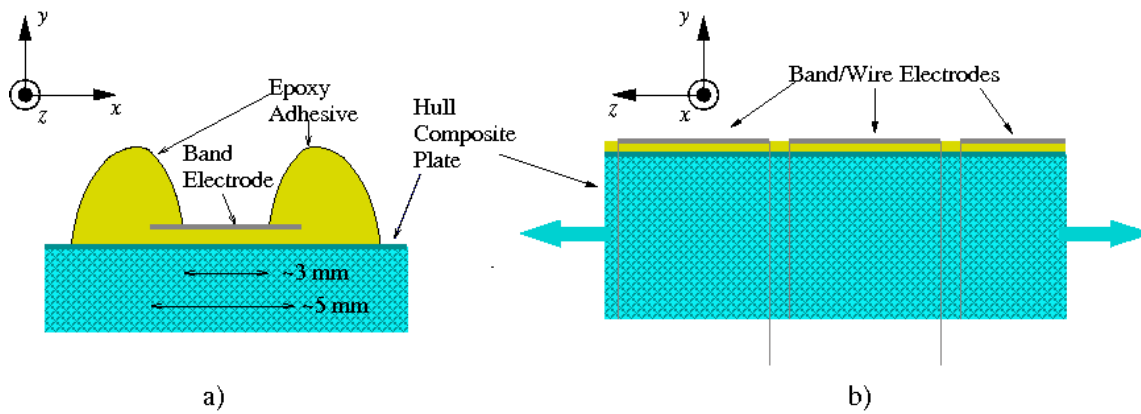


Figure 2.10 Mounting of band/wire electrode on the outside of the shell plates.

is electromagnetically and electronically close to identical to configuration a). However, configuration b) is probably mechanically more robust. In any case, mounting a wire on the outside of the shell plates may be problematic. The contact area between the wire and the plate is relatively small relative to the area that will be exposed to slamming waves. At the same time, silver is a soft material which will break at relative low tensile strains. It is probably better to use bands as this will increase contact area between the shell plate and the metal. In Figure 2.10 a), a suggested method of mounting such bands is shown. By pressing a silver band into a strip of epoxy glue, allowing the edges of the band to be covered by the epoxy, water flow will probably not be able to tear the band off the hull. The epoxy barriers will also provide some mechanical protection of the silver band itself. In order to avoid that the silver band is completely covered by epoxy, the central section can for instance be protected by a strip of paper which is removed before the epoxy has fully hardened. The silver bands should also be anchored in both ends through the shell plate as shown in Figure 2.10 b).

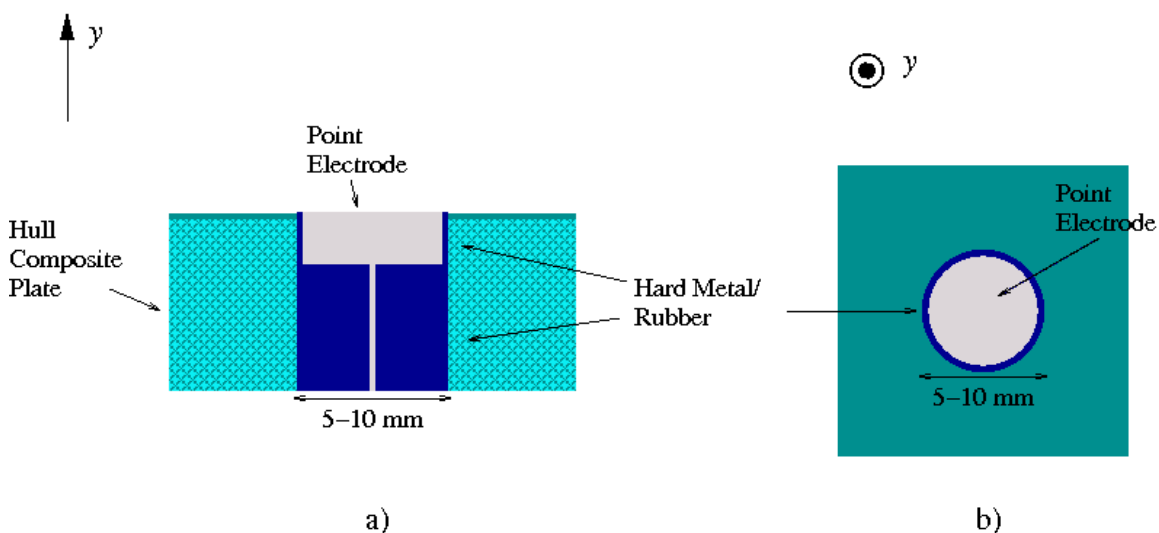


Figure 2.11 Mounting of point electrode embedded in a shell plate.

Point electrodes, as shown in Figure 2.9 c), is an alternative to using silver bands or wires. By having left and right electrodes at alternating heights, as shown in the figure, it will also here be possible to resolve the water depth with higher accuracy than the electrode spacing. The common left electrode need only one wet point, and thus we can measure the relative wave height by

placing this electrode at the keel, as shown in Figure 2.9 d) alternative is to only have one wet point of the common left electrode. This will perhaps require fewer holes to be drilled, but might lead to higher noise at the critical measurements of high water depth. From a processing point of view it is probably simpler if all the sensors have similar sensitivity as well. On the other hand, configuration d) is easier to place in the very front of the bow, similar to the pressure sensor mounting shown in Figure 3.3. One way of mounting such point electrodes is shown In Figure 2.11. As before, the y -axis is normal to the shell plate surface and pointing towards the wet surface. Since silver is quite a soft material, the electrode should probably be quite thick. The thickness of the electrode plug in this case has no importance for the radar signature since it is behind the shell plate wet surface. In order to avoid leakage into the composite material as the electrode plug wears down, the electrode should be placed within a sleeve of a tougher material, for instance a harder metal or rubber. This will also probably make it easier to replace an electrode plug than it would be to substitute a silver band glued to wet surface. However, as will be discussed in Subsection 3.1, a plug with diameter 5-10 mm probably should be anchored to a transverse bulkhead, for instance the inner wall of the sacrificial bow as illustrated in Figure 3.2.

2.1.2.3 Sensor Read-Out

There are many ways to read out the conductance sensor. We suggest grounding the common electrode, setting the voltage V_{in} on the dry side of the capacitor using a microcontroller unit (MCU), and, using the same MCU, measure the voltage V_{out} over the variable conductance G through and between the electrodes. A schematic of the read-out system is given in Figure 2.12. By setting $V_{in}(t)$ equal to a step function, it follows that V_{out} will have an exponential decay with a time constant equal to C/G :

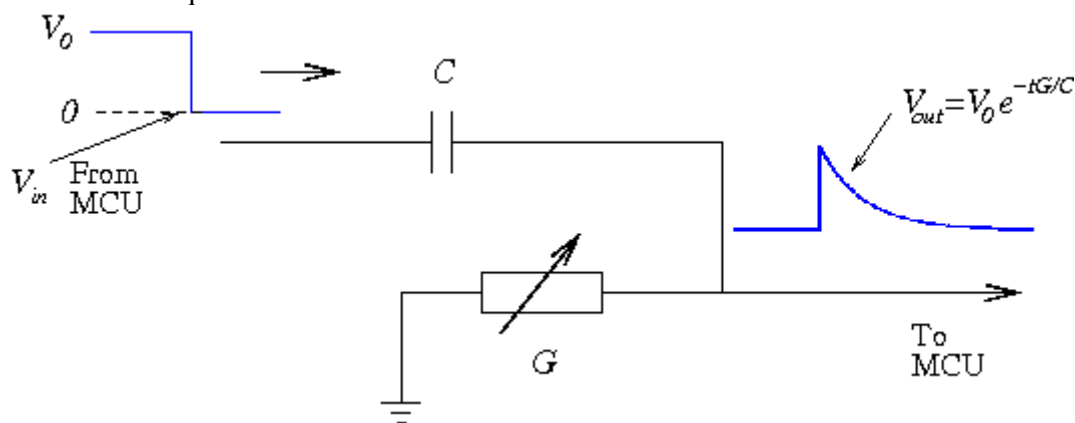


Figure 2.12 Proposed read-out circuitry

$$V_{out} = \begin{cases} 0 & , \text{ when } t < 0 \\ V_0 e^{-tG/C} & , \text{ when } t \geq 0 \end{cases} \quad (2.15)$$

when

$$V_{in} = \begin{cases} 0 & , \text{ when } t < 0 \\ V_0 & , \text{ when } t \geq 0 \end{cases} \quad (2.16)$$

Thus, by sampling V_{out} at a certain time, for instance when it is anticipated that V_{out} has decreased by factor e^{-1} assuming the electrode pair in question is completely below the sea surface, the

actual G can be estimated. Alternatively, the delay until V_{out} decreases to a certain level can be measured.

2.2 Inductance Sensors

Inductive loops have widespread use for the detection of electrical conductors. Examples of applications are handheld metal detectors, passenger security checks and vehicle detection in front of for instance traffic lights or speed cameras. Sea water is also conducting, and inductive loops can thus be used to detect its presence. Inductive loops are for instance used to measure the thickness of sea ice, as shown in Figure 2.13. The basic principle of inductive techniques is that temporal varying magnetic field induces current in conductors that perturbs the original field. The direction of the current is always such that the variation of the field is reduced.

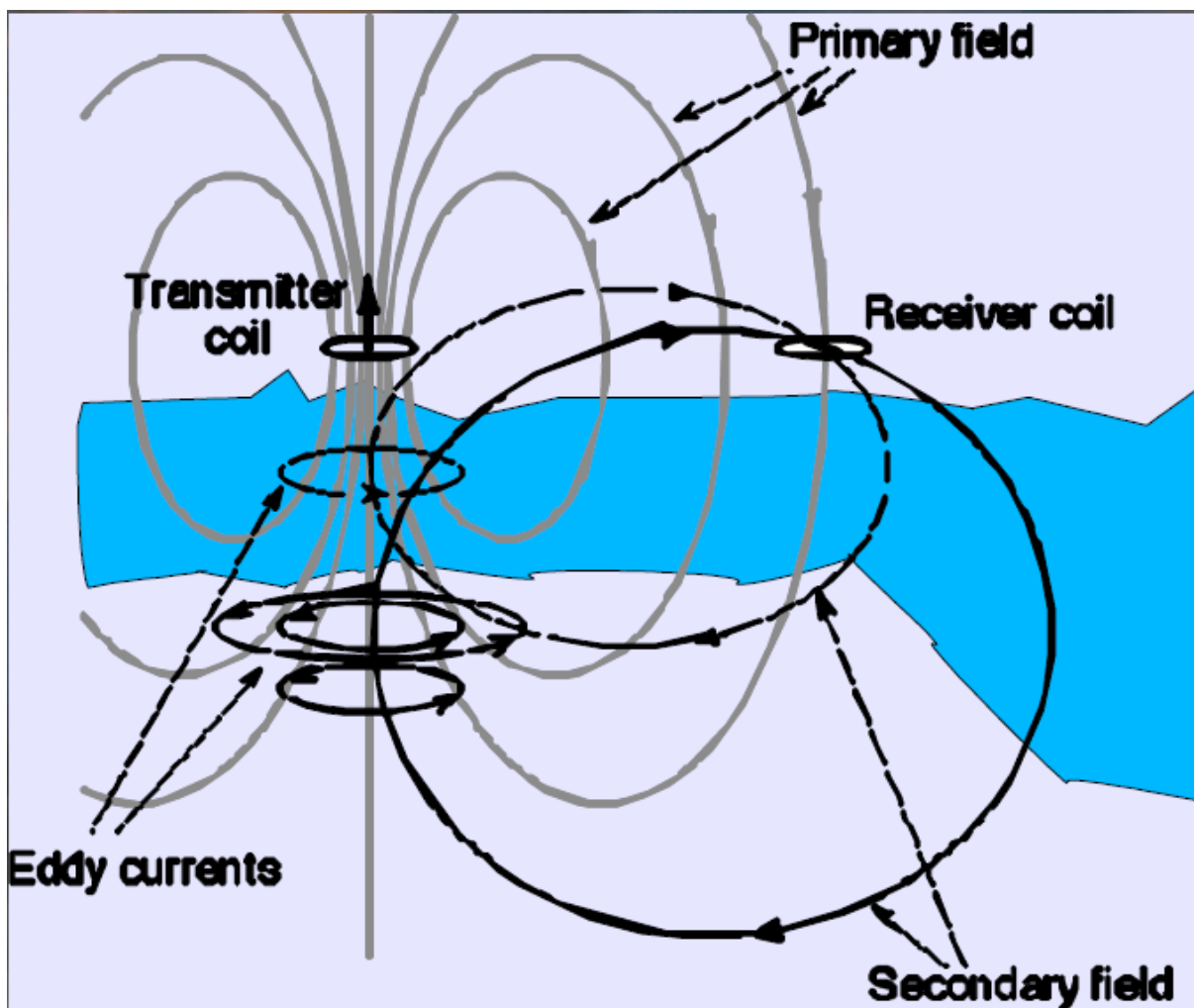


Figure 2.13 Measuring of ice thickness using an inductive measurements (from [3])

There are many methods to detect such a perturbation of the field, of which we have looked into three. The first technology to be developed was the so called beat frequency oscillator (BFO). This technique utilizes the fact that the perturbation of the magnetic field leads to a change of the induction L of the transmitting coil. The induction is evaluated by measuring the difference

(beat) frequency between an oscillating circuit including the transmitting coil and a reference oscillating circuit immune to the external fields. A technique with higher sensitivity is to have a separate receiver coil which is constructed in such a way that the contribution from the “mother field” from the transmitting coil is cancelled. I.e., the receiver coil current has no contribution from the directly transmitted field. However, fields from induced Eddy currents leads to induced currents in receiver coil. This technique is called induction balance (IB), and is currently dominating the metal detector market. We also have made the most thorough investigation into this technique due to its higher sensitivity than BFO and simpler read-out circuitry. In a third method, a circuit including a sensor coil and a reference coil can be brought close to oscillation, and made in such a way that it’s start to selfoscillates when a conductor is close to the sensor coil. We will not go into the great detail describing this sensor type, but we used it for some of our experiments.

2.2.1 Analyzed IB configurations

On the left side of Figure 2.14, a few examples of how IB can be achieved is shown. A long transmitter coil, drawn in red in the figure, is assumed to run along the entire region of interest for relative wave measurements. The length is assumed to be much longer than the width, so for theoretical purposes the transmitter coil can be treated like an infinitely long conductor pair. Multiple IB receiver coils, drawn in blue in the figure, will be placed along the length of the transmitter coil. One of the suggested IB arrangements, labeled IIa in the figure, relies on two concentric transmitter coils. The inner transmitter coil of IB arrangement IIa has opposite current direction compared with the outer coil. Three of the receiver/transmitter solutions, configuration Ib, Ic, and IIa, is induction balanced by utilizing that the magnetic field has opposite sign outside than inside the transmitter coil. However, with a single transmission wire pair and rectangular receiver coil, the receiver coil has to be infinite wide to include all magnetic lines and be completely induction balanced. Configurations Ib, Ic, and IIa are example of different solutions to this problem. Ib reduces the magnetic flux inside the loop between the transmission wire pair by introducing a linear tapering there of the receiving coil. One can imagine many other tapering functions, for instance a “step” tapering at each transmission wire. This would in effect be a strategy equal to the one chosen in Ic, where the receiving coil has more wires outside (M) than inside (N) the coil, i.e. $N_{rc,o} > N_{rc,i}$. In structure IIa, the outer field is strengthened by the introduction of a second wire pair.

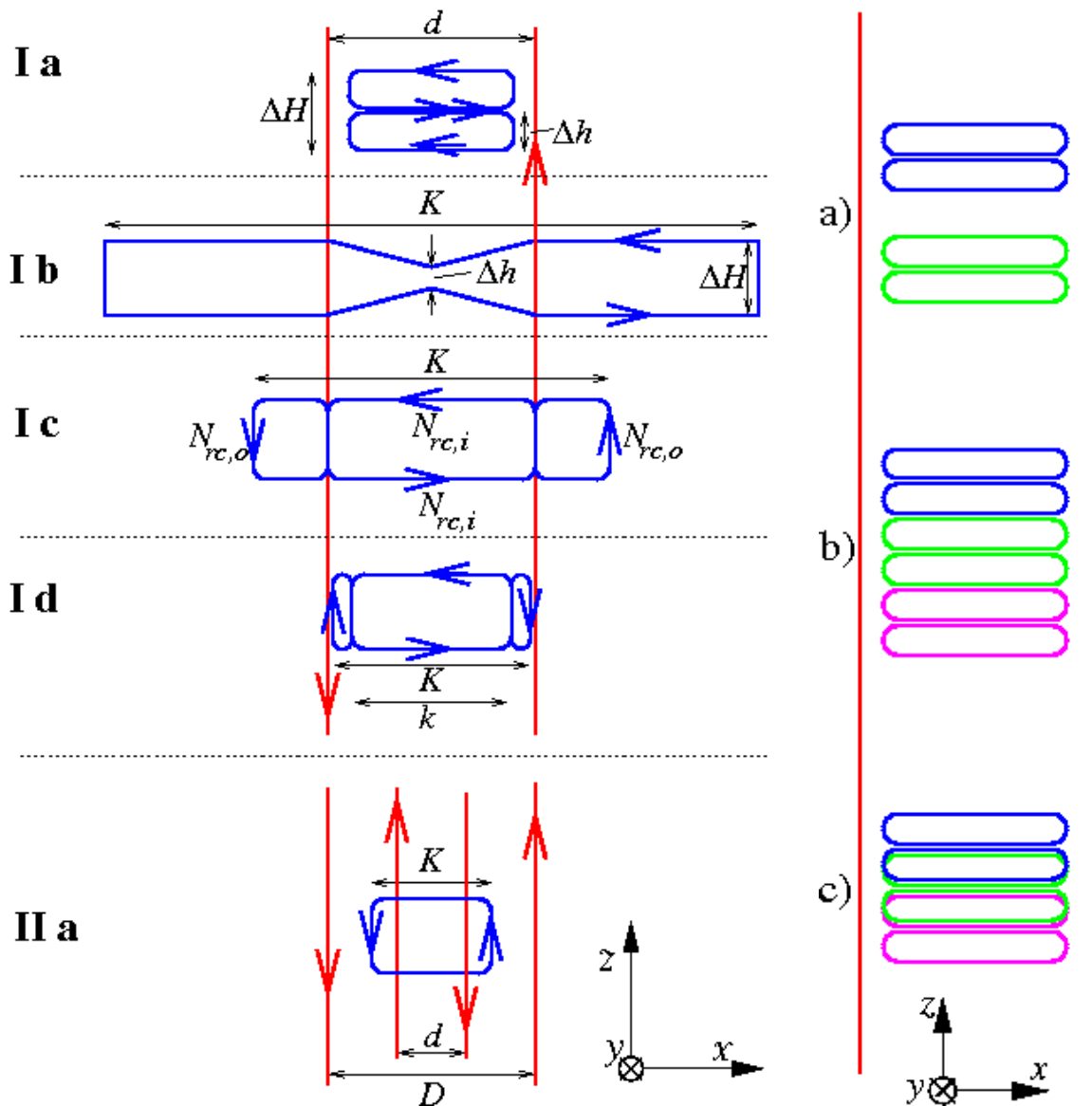


Figure 2.14 Left: Different induction balance (IB) structures considered for relative wave measurements. Right: Ways of arranging multiple suggested IB structures Ia.

For concepts Ia and Id, there is no sign change of the transmitted field within the coils, but induction balanced is achieved by having loops with opposing polarity, i.e. current direction. For most of the concepts, the presence of the sea water outside the hull will break the induction balance because the horizontal (x -) distribution of the magnetic field will change. An exception is configuration Ia, which will be induction balanced also with sea water covering the hull outside the whole receiver coil. However, for this sensor, the induction balance will be broken when the water level is half-way up the receiver coil, as illustrated in Figure 2.15. The different arrangement will be analyzed and discussed in detail in Subsection 2.2.2.

The density of the receiver coils, i.e. number of receiver coils per length, defines the resolution of the measurement. Since the current induced in the receiver coils will only induced a second-order perturbation to the magnetic field from the transmitter coil, the receiver coils can even be placed

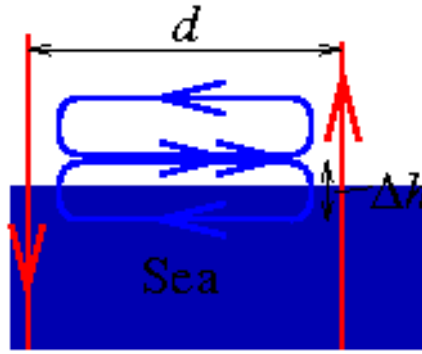


Figure 2.15 Breaking the induction balance of IB sensor configuration Ia.

in top of each other if dense measurements are required. This is illustrated on the right side of Figure 2.14. However, the resolution cannot be much better than the height of the receiver coils (i.e. Δh or ΔH) or the thickness of the shell composite plates (~ 6 cm).

2.2.2 Theoretical Considerations

2.2.2.1 Mutual Inductance

The theoretical basis for induction sensor is given by derivations from Maxwell's laws.

Specifically, as long as:

$$\frac{\omega l_{\text{typ}}}{c} = \frac{2\pi f l_{\text{typ}}}{c} \ll 1, \quad (2.17)$$

where f is the oscillation frequency and l_{typ} is a typical length scale of the problem, the magnetic field \vec{B} can be calculated using Biot-Savart law. For the dimensions in question here (tens of cm), it is sufficient that f is below the GHz range. The field $\vec{B}_{tc}(\vec{r})$ at position \vec{r} from a transmitter coil can thus be calculated from:

$$\vec{B}_{tc}(\vec{r}) = \frac{\mu_0 N_{tc} I_{tc}}{4\pi} \int_{tc} \frac{d\vec{l}(\vec{r}') \times (\vec{r} - \vec{r}')}{|\vec{r} - \vec{r}'|^3}. \quad (2.18)$$

The line integral is to be performed along the entire coil in question. μ_0 is the magnetic permeability, N_{tc} is the number of turns of the transmitter coil, I is its current, $d\vec{l}(\vec{r}')$ is the infinitesimal length of the coil element at position \vec{r}' . The magnetic field caused by the induced volume currents in the sea water is similarly given by:

$$\vec{B}_{sw}(\vec{r}) = \frac{\mu_0}{4\pi} \int_V \frac{\vec{J}_{sw}(\vec{r}') \times (\vec{r} - \vec{r}')}{|\vec{r} - \vec{r}'|^3} dV, \quad (2.19)$$

where $\vec{J}_{sw}(\vec{r}')$ is the induced current density at position \vec{r}' , and the integral is to be performed over the volume of interest. The induced current density is proportional to the induced electric field.

$$\vec{J}_{sw} = \sigma_{sw} \vec{E}_{sw} \quad (2.20)$$

The induced electric field in the sea water is given by Faraday's law:

$$\oint_C \vec{E}_{sw} \cdot d\vec{l} = -\frac{\partial \phi_s}{\partial t} = -M_{tc,C} \frac{\partial I}{\partial t} = -j\omega M_{tc,C} I_{tc}, \quad (2.21)$$

where

$$\phi_S = M_{ic,C} I_{ic} = \iint_S \vec{B}_{ic} d\vec{A}. \quad (2.22)$$

ϕ_S is the magnetic flux of the surface S , whereas $M_{ic,C}$ is the mutual inductance between the coil and an imaginary coil along the closed path C . C is the contour of the surface S . It can be shown that:

$$M_{ic,C} = M_{C,ic}. \quad (2.23)$$

Finally, the emf (electromotive force voltage) induced in the receiver circuit from the sea water currents is given from Faraday's law:

$$U_{emf,rc,SW} = -N_{rc} \frac{\partial \phi_{rc,SW}}{\partial t} = -j\omega N_{rc} \int_{S_{rc}} \vec{B}_{SW} d\vec{A} \quad (2.24)$$

Here N_{rc} is the number of turns of the receiving coil, and S_{rc} is a closed surface spanned out by the coil. As we will see below, the results given above will be somewhat simplified for the cylinder-symmetric or two-dimensional structures.

An important result, which perhaps is not immediately recognized from the above equation, is that $U_{emf,rc,SW}$ is of second order in ω and μ_0 , and further is proportional to the $N_{rc}N_{ic}$ product.

Note however, that the shielding provided by the eddy current density \vec{J}_{SW} , which in practice will limit the penetration depth, and hence $U_{emf,rc,SW}$, is ignored. Such shielding would be a third order effect in $U_{emf,rc,SW}$ but an analytical inclusion of this effect is difficult. The penetration depth δ_{SW} of electromagnetic fields in sea water is however given by:

$$\delta_{SW} = \frac{1}{\sqrt{\pi\mu_0\sigma_{SW}f}} \quad (2.25)$$

For a typical sea water conductivity of 3.8 S/m, which we get for 3.5 % salinity and 10 °C temperature, we get 1 m penetration depth at a magnetic field frequency of $f \approx 67$ kHz. For higher frequencies, the results of equations (2.18) - (2.24) will not be very realistic

2.2.2.2 Self-Inductance

The self-inductance of various coil types can be found in many text books so here only the main results applicable for our use will be given. The self-inductance of the transmitter coil is important to know in order to properly design transmitter driver circuitry. For BFO, the value of the self-inductance versus the mutual inductance squared also gives a measure of the sensitivity of this sensor.

The self-inductance L_{sol} for a long solenoid coil is simply given by:

$$L_{sol} = \frac{\mu_0 N^2 A}{l}. \quad (2.26)$$

A is the cross section area of the coil, N is the number of turns, and l is the length of the coil, i.e. the density of turns is N/l .

The self-inductance of a circular loop is given by $L_{\text{circular loop}}$:

$$L_{\text{circular loop},0} = \mu_0 N^2 R_{\text{loop}} \left(\ln \frac{8R_{\text{loop}}}{r_w} - 2 + Y \right). \quad (2.27)$$

Here R_{loop} is the radius of the loop and r_w is the radius of the wire. Y is a constant that is equal to $\frac{1}{4}$ when the current is conducted uniformly in the wire, and $Y=0$ when all the current is at the surface of the wire. The skin depth copper is 0.6 mm at 10 kHz and 0.2 mm at 100 kHz, so in the former case Y would be close to $\frac{1}{4}$ for most wires, so the value of Y could be anywhere between 0 and $\frac{1}{4}$ for realistic wire thicknesses.

For two long parallel wires, the inductance is given by:

$$L_{\text{wire pair}} = N^2 \frac{\mu_0 l}{\pi} \left(\ln \frac{d}{r_w} + Y \right), \quad \text{where } d \ll l \quad (2.28)$$

d is the distance between the wires and l is the length of the wires.

The standard result of equation (2.28) is found by integrating the field from a single wire from its surface to the center of the other wire. This method can also be used as a basis to find the self-inductance of two transmitting wire pairs, where one of the pairs are placed symmetrically around the other pair in the same plane but with opposite polarity, as configuration IIa in Figure 2.14. In this case we have 6 different wire combinations, but the wire combinations where the two wires have equal current direction will contribute to a reduction in the overall induction. We get:

$$\begin{aligned} L_{2\text{wire pairs}} &= N^2 \frac{\mu_0 l}{\pi} \left[\ln \left(\frac{D-d}{2r_w} \frac{2r_w}{D+d} \frac{D}{r_w} \frac{d}{r_w} \frac{2r_w}{D+d} \frac{D-d}{2r_w} \right) + 2Y \right] \\ &= N^2 \frac{\mu_0 l}{\pi} \left\{ \ln \left[\left(\frac{D-d}{D+d} \right)^2 \frac{dD}{r_w^2} \right] + 2Y \right\}, \quad \text{where } d \ll l. \end{aligned} \quad (2.29)$$

In addition to inductance, the various coil structures also have some resistance which will be frequency dependent due to the skin effect. However, in all cases treated here, with reasonably low frequencies, high conducting wires (and possibly using Litz wires which mitigates the skin effect) the resistance will be small compared with the self inductance.

2.2.2.3 Beat Frequency Oscillator (BFO)

Even assuming that we have a circular loop with one turn, the expressions quickly become nasty, but it can be shown from equation (2.18) that the y-component of the magnetic flux density is given by:

$$B_{y,ic} = B_0 \frac{1}{\pi Q} \left[C(k) \frac{1-\alpha^2-\beta^2}{Q-4\alpha} + K(k) \right], \quad (2.30)$$

where

$$B_0 = \frac{\mu_0 I_{ic}}{2R_{\text{coil}}}, \quad (2.31)$$

$$\alpha = \frac{\rho}{R_{\text{coil}}}, \quad (2.32)$$

$$\beta = \frac{y}{R_{\text{coil}}}, \quad (2.33)$$

$$Q = \left[(1 + \alpha)^2 + \beta^2 \right], \quad (2.34)$$

$$k = \sqrt{\frac{4\alpha}{Q}}. \quad (2.35)$$

$$\rho = \sqrt{x^2 + z^2} \quad (2.36)$$

Here $C(k)$ and $K(k)$ are the so-called complete elliptic integral function of the first and second kind. The Cartesian axis system is defined as before and illustrated in Figure 2.1, and it is assumed that the coil is located oriented parallel with the shell plate and with its center co-located with the origin of the coordinate system.

Deep down in the water we can assume that we have cylindrical symmetry, and equation (2.21) reduces to:

$$2\pi\rho E_g(\rho, y) = -j\omega M_{tc,C} I_{tc} = -j2\pi\omega \int_0^\rho B_{y,tc}(\rho', y) d\rho'. \quad (2.37)$$

and using the reciprocity relation (2.23) and the fact that the receiver and transmitter coil in this case is identical, we get from equation equations (2.19), (2.20) and (2.24):

$$\begin{aligned} U_{emf,tc,SW} &= -N_{tc} \frac{\partial \phi_{tc,SW}}{\partial t} = -j\omega \int_0^\infty \int_t^\infty M_{C,tc}(\rho', y') J_\theta(\rho', y') dy d\rho \\ &= -\frac{\omega^2 \sigma_{SW} I_{tc}}{2\pi} \int_0^\infty \int_t^\infty \frac{M_{tc,C}^2(\rho', y')}{\rho'} dy d\rho \end{aligned} \quad (2.38)$$

where the mutual induction $M_{tc,C}(\rho, y)$ between the sensor loop and a virtual loop in the sea water of radius ρ around the y-axis a distance y from the sensor loop is given by:

$$M_{tc,C}(\rho, y) = \frac{2\pi}{I_{tc}} \int_0^\rho B_{y,tc}(\rho', y) \rho' d\rho'. \quad (2.39)$$

t is the distance from the loop to the sea water. Hence, the addition in inductance caused by the sea water is given by:

$$\begin{aligned} \Delta L_{\text{circular loop,SW}} &= \frac{U_{emf,tc,SW}}{j\omega I_{tc}} \\ &= \frac{j\omega \sigma_{SW} I_{tc}}{2\pi} \int_0^\infty \int_t^\infty \frac{M_{tc,C}^2(\rho', y')}{\rho'} dy d\rho. \end{aligned} \quad (2.40)$$

Thus, the presence of sea water increases the impedance amplitude of the coil, but also introduces a phase shift. Of course, the integrals (2.39)-(2.40) does not have an analytic solution, but can be calculated numerically.

When the coil is part of an oscillation circuit, the oscillation frequency can be calculated from the capacitance and inductance of the circuit. Assuming the ideal case where the coil is the only

inductive element of the circuit, we get that the oscillation frequency is given by the well known expression:

$$f = \frac{2\pi}{\sqrt{L_{\text{circular loop},0} C}}. \quad (2.41)$$

Assuming $\Delta L_{\text{circular loop},\text{SW}} \ll L_{\text{circular loop},0}$, the beat Δf frequency between the sensor with sea water on the outside and the reference sensor is given by:

$$\begin{aligned} \Delta f &= \frac{2\pi}{\sqrt{L_{\text{circular loop},0} C}} - \frac{2\pi}{\sqrt{(L_{\text{circular loop},0} + \Delta L_{\text{circular loop},\text{SW}}) C}} \\ &\approx \frac{1}{2} \frac{\Delta L_{\text{circular loop},\text{SW}}}{L_{\text{circular loop},0}} f. \end{aligned} \quad (2.42)$$

Note that since $\Delta L_{\text{circular loop},\text{SW}} \propto f$, we have that $\Delta f \propto f^2$. If there are other inductive elements in the oscillation circuit, $L_{\text{circular loop},0}$ has to be substituted with the real inductance of the circuit.

In Figure 2.16, the beat frequency Δf is plotted as a function of R_{coil} for $Y=1/4$ and for different values of the wire thickness r_w and distance between the loop and salt water t . Skin effects in the coil and salt water is ignored. The left y-scale is given for $\Delta f / f^2$, which in this case will be independent of f . On the right scale Δf is given for $f=20$ kHz. With the thickness of the shell plate being approximately 6 cm, a realistic value of t is 7 cm. In order to get a resolution of the measurement of the order of 20 cm, the R_{coil} should probably not be much larger than 20-40 cm. From Figure 2.16 we see that increasing t from 2 to 7 cm in itself only decreases the sensitivity of the sensor with 35 % at $R_{\text{coil}}=20$ cm, and less at higher values of R_{coil} . Also the r_w seems to have relatively little importance for typical thicknesses.

2.2.2.4 Induction Balance (IB) Sensors

Transmitted Magnetic Field and Conditions for Induction Balance

As discussed in Subsection 2.2.1, all suggested IB configurations will involve one or two transmitter loops consisting of two parallel wires running from top to down inside the hull. Since the distances between the wires (d and, in configuration IIa, D) and the distance from the transmitting loop to the outside of the hull both will be much smaller than the height of the loop, we can assume that the transmitted magnetic field will be independent of the height z . It can be shown

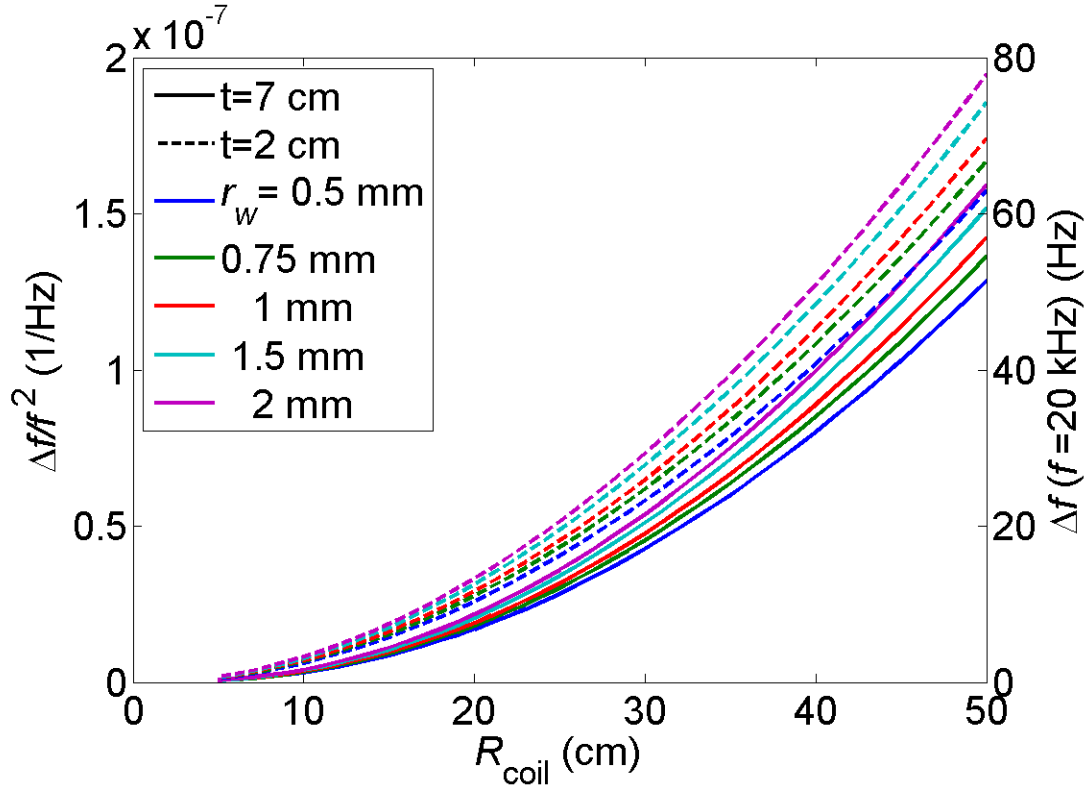


Figure 2.16 Beat frequency of BFO induction sea water sensor based on a circular loop as a function of loop radius R_{coil} for different distances to the outer hull surface t and conducting wire radius r_w . The skin effect in salt water is ignored, and it is assumed that $Y=1/4$ in equation(2.27). On the left y-axis the scale for the normalized beat frequency $\Delta f / f^2$ is given, whereas the right y-axis scale is Δf calculated for an interrogating oscillating frequency $f=20$ kHz

from Biot-Savart law given in equation (2.18) that the magnetic flux density around an infinitely long wire with current I in cylindrical coordinates is given by:

$$\vec{B}(\rho) = \frac{\mu_0 I}{2\pi\rho} \hat{\theta}. \quad (2.43)$$

Here ρ is the distance (radius) from the wire and $\hat{\theta}$ is the azimuthal unit vector. Transferred to Cartesian coordinates and using the superposition principle, we get that the magnetic flux density around a single pair of bundled parallel long wires with current of opposite sign is given by:

$$\vec{B}_{ic,l}(x, y) = \frac{\mu_0 N_{ic} I_{ic}}{2\pi} \left[\frac{-y\hat{x} + \left(x + \frac{d}{2}\right)\hat{y}}{\left(x + \frac{d}{2}\right)^2 + y^2} + \frac{-y\hat{x} + \left(x - \frac{d}{2}\right)\hat{y}}{\left(x - \frac{d}{2}\right)^2 + y^2} \right]. \quad (2.44)$$

N_{ic} is the number of wires in each bundle, I_{ic} is the the current running through each wire and d is still the distance between the two wires. Figure 2.1 and Figure 2.14 (right) still give an accurate illustration of the orientation and location of the wires with respect to the coordinate system. I_{ic} is assumed to be positive in the wire bundle located in $x = d/2$.

For simplicity, we chose to add the additional coil of configuration IIa symmetrical around the other coil, but with the polarity opposite in the outer and inner coil, and the transmitted magnetic field in this case becomes:

$$\vec{B}_{tc,II}(x, y) = \frac{\mu_0 N_{tc} I_{tc}}{2\pi} \left[\begin{aligned} & -\frac{y\hat{x} + \left(x + \frac{D}{2}\right)\hat{y}}{\left(x + \frac{d}{2}\right)^2 + y^2} + \frac{-y\hat{x} + \left(x + \frac{d}{2}\right)\hat{y}}{\left(x + \frac{d}{2}\right)^2 + y^2} \\ & -\frac{-y\hat{x} + \left(x - \frac{d}{2}\right)\hat{y}}{\left(x - \frac{d}{2}\right)^2 + y^2} + \frac{-y\hat{x} + \left(x - \frac{D}{2}\right)\hat{y}}{\left(x - \frac{D}{2}\right)^2 + y^2} \end{aligned} \right] \quad (2.45)$$

As illustrated in Figure 2.14, D is the distance between the outer transmitter bundles.

Based on the magnetic flux density given by equation (2.44) or (2.45), we now must find the conditions under which the coil configurations illustrated in Figure 2.14 is induction balanced, i.e. when the net magnetic flux through the receiver coil in the $y=0$ plane is zero in the absence of sea water. Structure Ia is the simplest case in this regard, as it will be induction balanced as long as the upper and lower loops of the receiver coil have identical height. For structure Ib, the idea of the receiving loop is that the stronger positive field between the two wires compared with the negative field on the outside, should be offset by narrowing the receiver coil linearly towards the center between the two wires, as illustrated in Figure 2.14. We have that the transmitted flux going through the receiver coil, $\phi_{tc,rc,lb}$ is dependent on:

$$\begin{aligned} \phi_{tc,rc,lb} &\propto \int_0^{\frac{d}{2} - r_w} \left(\frac{1}{x' - \frac{d}{2}} - \frac{1}{x' + \frac{d}{2}} \right) \left[\frac{\Delta h}{\Delta H} + \frac{2x' \left(1 - \frac{\Delta h}{\Delta H}\right)}{h} \right] dx' + \int_{\frac{d}{2} + r_w}^{\frac{K}{2}} \left(\frac{1}{x' - \frac{d}{2}} - \frac{1}{x' + \frac{d}{2}} \right) dx' \\ &= \frac{\Delta h}{\Delta H} \ln \frac{d^2}{4(d - r_w)^2} + \ln \frac{4|K - d|(d + r_w)(d - r_w)}{d^2(K + d)}. \end{aligned} \quad (2.46)$$

As indicated by Figure 2.14, K is the width of the receiving coil, Δh is its height in the middle and ΔH is its height at the edges. In order to get induction balance $K > d$, and if we in addition assume $r_w \ll d$, we get that $\phi_{tc,rc,lb} \approx 0$ when:

$$\frac{\Delta h}{\Delta H} \approx \frac{\ln \left(2 \frac{K - d}{K + d} \right)}{\ln 2} = 1 - \frac{\ln \left(\frac{1 + \frac{d}{K}}{1 - \frac{d}{K}} \right)}{\ln 2}. \quad (2.47)$$

This means, that in order to obtain a non-negative Δh , K needs to be at least three times d . As we will see later, this in practice means that structure Ib is not very efficient compared for instance with Ia.

In structure Ic, we rather offset the stronger field inside the transmitter coil by having more receiving turns on the outside (M_{tr}) of the transmitter coil than inside (N_{rc}). The transmitted magnetic flux seen by the receiver coil, $\phi_{tc,rc,lc}$ is thus proportional to:

$$\begin{aligned}\phi_{\text{tc,rc,lc}} &\propto N_{rc,i} \int_0^{\frac{d-r_w}{2}} \left(\frac{1}{x' - \frac{d}{2}} - \frac{1}{x' + \frac{d}{2}} \right) dx' + N_{rc,o} \int_{\frac{d+r_w}{2}}^{\frac{K}{2}} \left(\frac{1}{x' - \frac{d}{2}} - \frac{1}{x' + \frac{d}{2}} \right) dx' \\ &= N_{rc,i} \ln \frac{r_w}{d-r_w} + N_{rc,o} \ln \frac{(K-d)(d-r_w)}{(K+d)}.\end{aligned}\quad (2.48)$$

We have induction balance $\phi_{\text{tc,rc,lc}} = 0$ if:

$$\frac{N_{rc,i}}{N_{rc,o}} = \frac{\ln \frac{(K-d)(d+r_w)}{(K+d)r_w}}{\ln \frac{d-r_w}{r_w}} \approx \frac{\ln \left(\frac{K-d}{K+d} \frac{d}{r_w} \right)}{\ln \frac{d}{r_w}} = 1 - \frac{\ln \left(\frac{1-d/K}{1+d/K} \right)}{\ln \frac{d}{r_w}}.\quad (2.49)$$

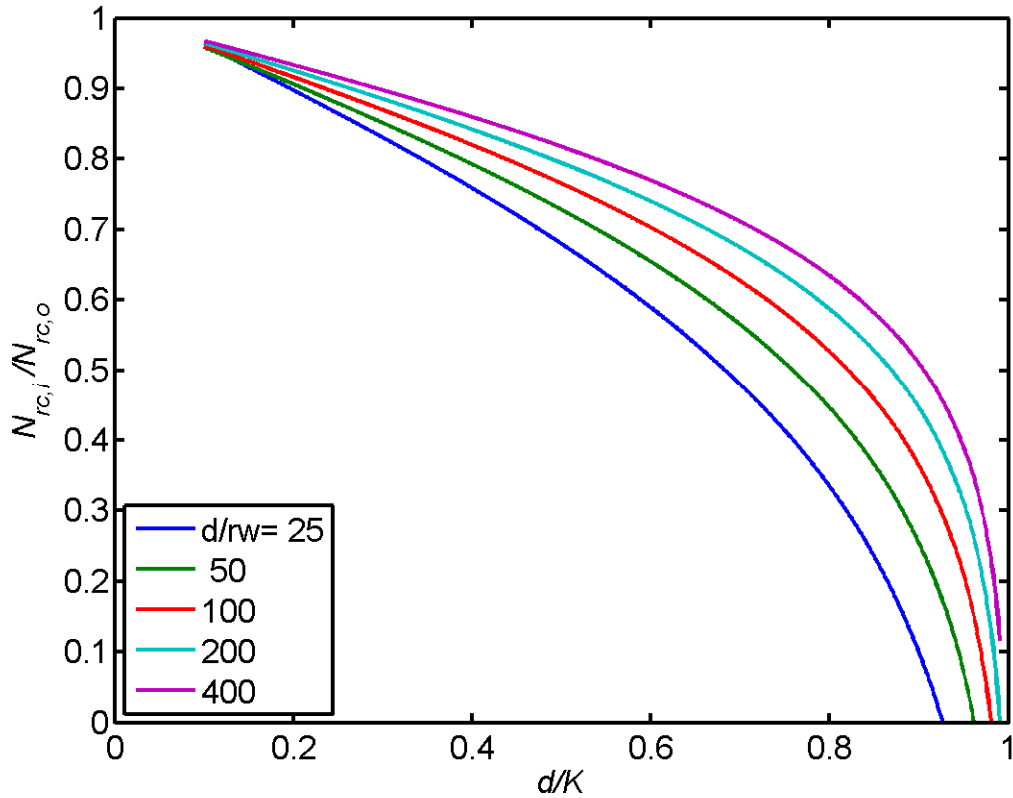


Figure 2.17 The required ratio between the number of inner and outer turns, $N_{rc,i}/N_{rc,o}$, required in order for structure Ic to be induction balanced as a function of the receiver coil width (d) divided by the transmission wire separation (K). The plot is performed for various transmission wire radius, r_w .

The approximation above is valid when $r_w \ll d$. In Figure 2.17, the required $N_{rc,i}/N_{rc,o}$ is plotted as a function of d/K for different values of d/r_w .

In a similar manner, induction balance is achieved for structure Id given that:

$$\begin{aligned}\phi_{tc,rc,Id} &\propto \int_0^{\frac{k}{2}} \left(\frac{1}{x' - \frac{d}{2}} - \frac{1}{x' + \frac{d}{2}} \right) dx' - \int_{\frac{k}{2}}^{\frac{K}{2}} \left(\frac{1}{x' - \frac{d}{2}} - \frac{1}{x' + \frac{d}{2}} \right) dx' \\ &= \ln \left[\left(\frac{d-k}{d+k} \right)^2 \frac{d+K}{d-K} \right] = 0.\end{aligned}\quad (2.50)$$

⇓

$$\frac{k}{d} = \frac{2d - \sqrt{2(d-K)(d+K)}}{2K} \approx 1 - \sqrt{\frac{d-K}{d}} + \frac{d-K}{d}.\quad (2.51)$$

k is the width of the center loop of the receiving coil. The last approximation of equation (2.51) is valid for $d - K \ll d$.

Finally, we find induction balance for structure IIa with two transmission coils when:

$$\phi_{tc,rc,IIa} \propto \int_0^{\frac{K}{2}} B_{tc,II,y}(x', y=0) dx' = \ln \frac{(K+d)(D-K)}{(K-d)(D+K)} = 0\quad (2.52)$$

⇓

$$K = \sqrt{dD}.\quad (2.53)$$

I.e., in order to achieve induction balance in configuration IIa, the width of the receiving coil has to be equal to the geometrical mean of the transmitting coils.

Induced EMF for Different Induction Balance Principles

If we still assume that we have perfect induction balance, we can find the induced emf in the receiving coils in the sea water, $U_{emf,rc}$ from:

$$U_{emf,rc} = -\frac{\omega^2 \sigma_{sw} I_{tc}}{2\Delta H} \int_0^{\infty} \int_t^{\infty} M_{tc,C}(x', y', \Delta H) M_{rc,C}(x', y', \Delta H) dy' dx'\quad (2.54)$$

Here ΔH is the height of the receiving coil. In order to derive equation (2.54), a similar argument as used to derive equations (2.37)-(2.38) have been used. When calculating the mutual inductances $M_{tc,C}$ and $M_{rc,C}$ we assume that transmitting wires are long and that we are far down into the sea water. Both the transmitted magnetic field and the magnetic field induced by the sea water can then be assumed to be independent of height. Hence both $M_{tc,C}$, $M_{rc,C}$ and hence $U_{emf,rc}$ are proportional to ΔH .

Due to the symmetry of the problem, the induced electric field in the sea water will be parallel to the transmission wire pair(s) and anti-symmetric in the x -direction. We should integrate over a rectangle in the xz -plane symmetrically around the transmission wire pair(s) in order to find the mutual inductance between the pair(s) and a point (x,y) in the sea water, and we find in equivalence to equation (2.39):

$$M_{tc,C}(x, y, \Delta H) = \frac{2\Delta H}{I_{tc}} \int_0^x B_{y,tc}(x', y) dx'.\quad (2.55)$$

Hence, for the single transmission wire pair structures, we get from equation (2.44):

$$\begin{aligned}
 M_{tc,C,I}(x, y, \Delta H) &= \frac{\Delta H \mu_0 N_{tc}}{\pi} \int_0^x \left[-\frac{x' + d/2}{(x' + d/2)^2 + y^2} + \frac{x' - d/2}{(x' - d/2)^2 + y^2} \right] dx' \\
 &= \frac{\Delta H \mu_0 N_{tc}}{2\pi} \ln \left[\frac{(x - d/2)^2 + y^2}{(x + d/2)^2 + y^2} \right].
 \end{aligned} \tag{2.56}$$

Similarly, we get using the result (2.45) that the mutual induction between the double transmission wire pair structure and a point (x,y) in the sea water is given by:

$$M_{tc,C,II}(x, y, \Delta H) = \frac{\Delta H \mu_0 N_{tc}}{2\pi} \ln \left\{ \frac{\left[\left[(x + d/2)^2 + y^2 \right] \left[(x - D/2)^2 + y^2 \right] \right]}{\left[\left[(x - d/2)^2 + y^2 \right] \left[(x + D/2)^2 + y^2 \right] \right]} \right\}. \tag{2.57}$$

Since the mutual induction is reciprocal, and the fields are independent of z , we can use equation (2.55) also to calculate the mutual induction between the receiver coils and a point in the sea water, $M_{rc,C}(x, y, \Delta H)$. In order to find $M_{rc,C}$, we thus have to find the magnetic field that would have been caused by a current of a long ($\Delta H \gg K, k$) receiver coil.

Structure Ia is in this respect particular, as the mutual inductance between the sea and the whole receiver coil is zero at large depths. Instead, we define $M_{rc,C,Ia}$ to be the mutual inductance between the upper (or lower) half of the coil with height $\Delta h = \Delta H$:

$$\begin{aligned}
 M_{rc,C,Ia}(x, y, \Delta H) &= \frac{2\Delta h}{I_{tc}} \int_0^x B_{y,rc,Ia/2}(x', y) dx' \\
 &= \frac{\Delta H \mu_0 N_{rc}}{4\pi} \ln \left[\frac{(x - K/2)^2 + y^2}{(x + K/2)^2 + y^2} \right].
 \end{aligned} \tag{2.58}$$

K is the width (in the x -direction) of the coil. Defining $M_{rc,C,Ia}$ this way is strictly correct only when ΔH is large compared with y , i.e. (2.58) can strictly speaking only be used to find the induced voltage when ΔH is much larger than the shell plate thickness (t). Compared with the other structures, however, Ia can be interrogated both on a rising slope (when the lower half is lowered into the water) and a declining slope (when the upper half goes into the water), which in effect doubles the resolution of the sensor. Everything considered, it is therefore believed that using equation (2.58) results in a reasonable figure of merit compared with the other structures.

For structure Ib, there is no doubt of the interpretation as for configuration Ia, but the expressions are a bit more complex due to the more complicated coil structure. The magnetic flux density from a current in the receiver coil becomes:

$$B_{y,rc,lb}(x, y) = \frac{\mu_0 I_{rc} N_{rc}}{2\pi} \left\{ -\frac{x + K/2}{\left(x + K/2\right)^2 + y^2} + \frac{x - K/2}{\left(x - K/2\right)^2 + y^2} + \frac{(1 - \Delta h / \Delta h)}{d} \ln \left[\frac{\left(x - d/2\right)^2 + y^2}{\left(x + d/2\right)^2 + y^2} \right] \right\}. \quad (2.59)$$

The mutual inductance is again found from integrating the flux density as in equation (2.55)

$$M_{rc,C,lb}(x, y, \Delta H) = \frac{\Delta H \mu_0 N_{rc}}{2\pi} \times \left[\ln \left(\frac{\left[\frac{x - K/2}{\left(x + K/2\right)^2 + y^2} \right]}{\left[\frac{x + K/2}{\left(x + K/2\right)^2 + y^2} \right]} \right) + \frac{2(1 - \Delta h / \Delta H)}{d} \left(\ln \left\{ \frac{\left[\left(x + d/2\right)^2 + y^2 \right]^{x+d/2} \left[\left(x - d/2\right)^2 + y^2 \right]^{x-d/2}}{\left[x^2 + y^2 \right]^{2x}} \right\} - 2y \arctan \left\{ \frac{2d^2 xy}{4 \left[x^2 + y^2 \right] + d^2 \left[y^2 - x^2 \right]} \right\} \right) \right] \quad (2.60)$$

We get the most efficient structure for $\Delta h = 0$ since then the overlap with $M_{rc,C,l}$ is largest given the width available for our sensor and transmitter coils.

For structure Ic, we get that the mutual induction is given by:

$$M_{rc,C,Ic}(x, y, \Delta H) = \frac{\Delta H \mu_0 N_{rc,i}}{2\pi} \times \ln \left(\left\{ \frac{\left[\left(x - d/2 + r_w\right)^2 + y^2 \right]}{\left[\left(x + d/2 - r_w\right)^2 + y^2 \right]} \right\} \left\{ \frac{\left[\left(x + d/2 + r_w\right)^2 + y^2 \right]}{\left[\left(x - d/2 - r_w\right)^2 + y^2 \right]} \right\} \left\{ \frac{\left[\left(x - K/2\right)^2 + y^2 \right]}{\left[\left(x + K/2\right)^2 + y^2 \right]} \right\} \right)^{N_{rc,o}/N_{rc,i}}. \quad (2.61)$$

Note that $N_{rc,i}/N_{rc,o}$ is given from d/K and d/r_w from the relation (2.49).

For structure Id, the mutual induction is given by:

$$M_{rc,C,Id}(x, y, \Delta H) = \frac{\Delta H \mu_0 N_{rc}}{2\pi} \ln \left\{ \frac{\left[\left(x - k/2\right)^2 + y^2 \right]}{\left[\left(x + k/2\right)^2 + y^2 \right]} \frac{\left[\left(x + K/2\right)^2 + y^2 \right]}{\left[\left(x - K/2\right)^2 + y^2 \right]} \right\} \quad (2.62)$$

where k/d is given by equation (2.51).

Finally, for structure IIa, we find the following mutual inductance between the receiver coil and the sea water:

$$M_{rc,C,IIa}(x, y, \Delta H) = \frac{\Delta H \mu_0 N_{rc}}{2\pi} \ln \left[\frac{\left(x - \frac{K}{2}\right)^2 + y^2}{\left(x + \frac{K}{2}\right)^2 + y^2} \right] \quad (2.63)$$

Here it should be remembered that $K = \sqrt{dD}$ from equation (2.53).

Comparison between Different Induction Balanced Coil Structures

With the given logarithmic expressions of the mutual inductance, there is no analytical solution of the integral (2.54), but it is of course easily evaluated numerically. In order to evaluate the different structures, we have focused on the ratio between the induced voltage of the receiving loop and the driving voltage of the transmitting loop:

$$\left| \frac{U_{emf,rc}}{U_{tc}} \right| = \frac{\omega \sigma_{sw}}{2\Delta H L_{tc} N_{tc}} \left| \int_0^\infty \int_t^\infty M_{tc,C}(x', y', \Delta H) M_{rc,C}(x', y', \Delta H) dy' dx' \right| \quad (2.64)$$

Here L_{tc} is given by equation (2.28) for single wire pair transmission (structures Ia, Ib, Ic, and Id) and equation (2.29) for dual wire pair transmission (structure IIa). This is of course assuming that the transmission loop is the dominating contribution to the impedance of the driving circuit. Note that the driving voltage, U_{tc} , is $\pi/2$ out of phase with the measured voltage of the receiving loop, $U_{emf,rc}$, when all higher order terms to the inductances caused by the presence of the sea water is ignored. In order to compare the different structures, we have assumed that the width of the widest coil is 0.3 m.

It is at this point not clear what the major noise source of the system would be, and it could vary dependent on the chosen configuration as well as the ambient environment. If the signal picked up by the receiver coil is weak, internal thermal and electronic noise of the receiver is probably dominating, and signal to noise ratio of the system will depend on the signal strength. We define the figure of merit in this case to be equal to the $U_{emf,rc}/U_{tc}$ -ratio assuming a single (effective) receiver coil turn.

If the signal picked up by the receiver is reasonably strong, however, electric noise from other sources picked up by the receiver coil could dominate. In such a case, the signal strength relative to the noise pick-up capability is the relevant parameter for the noise performance. Assuming that inductive sensor has an operating frequency around or below 100 kHz, the noise field can probably be assumed to be approximately uniform across the receiver coil surface, and the pick-up capability of external noise fields will therefore for most of the discussed inductive sensor topologies scale proportionally to the number of turns and the surface area of the sensor. An exception to this is the two structures (Ia and Id) where different loops of the receiver coil has opposite current direction. These cases will be discussed further below. We define the figure of merit in this noise limit to be the $U_{emf,rc}/U_{tc}$ -ratio assuming a single effective receiver coil turn, but with $U_{emf,rc}$ normalized according to a ambient noise pick up capability of a uniform receiver coil of width 0.3 m. This means that the normalized $U_{emf,rc}/U_{tc}$ -ratio increases inversely

proportional to the noise pick up capability, and that structure with a receiver coil width equal to 0.3 m already is naturally normalized.

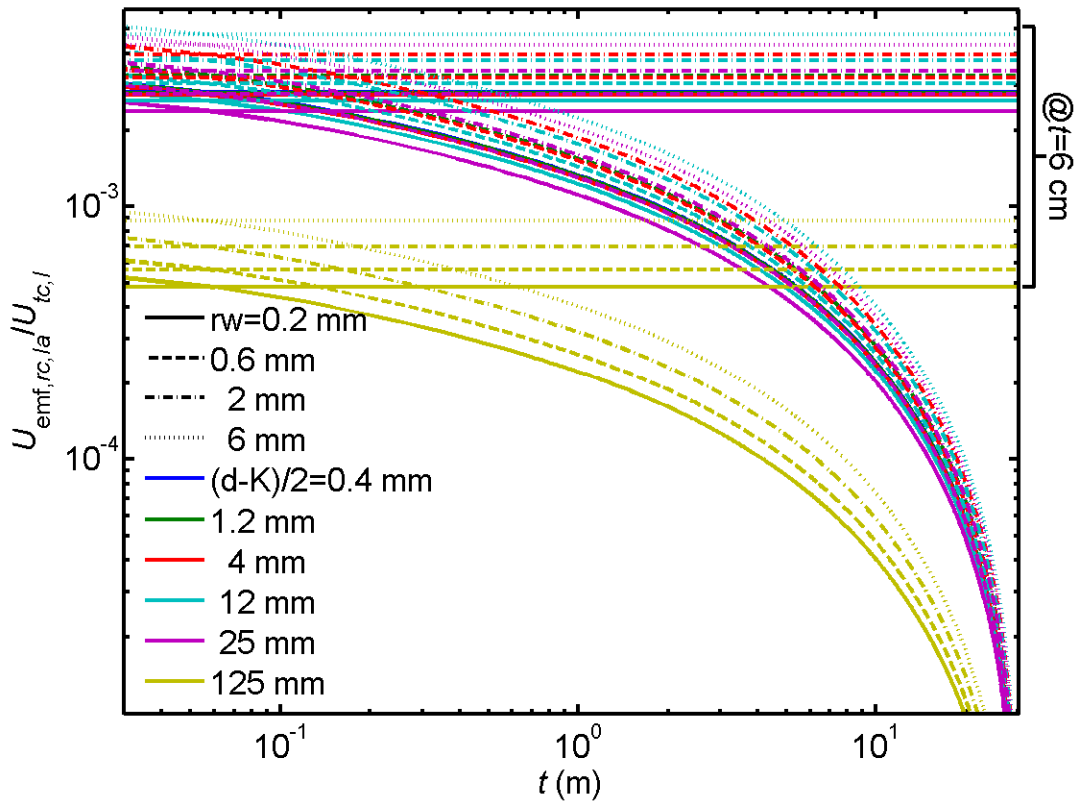


Figure 2.18 Ratio between induced voltage per turn of the receiver coil over required driving voltage amplitude of the transmission coil per length for coil structure Ia as function of distance between the coils and the sea/hull surface t . The horizontal line is the ratio when the distance is 6 cm. Plots are given for different wire diameters and width difference between the receiver and transmission coil widths. For all plots, the total width of the coil structure is 0.3m and the chosen RF frequency is 20 kHz.

In Figure 2.18, the $U_{emf,rc} / U_{tc}$ -ratio is plotted for structure Ia. As expected, this figure of merit increases with increasing receiver coil width (i.e. with decreasing $(d-K)$ -value) and increasing transmission coil wire thickness (r_w), and hence decreasing inductance L . Except for the extremely small coil width ($(d-K)/2=0.125\text{m} \Rightarrow K=5\text{ cm}$), the value of r_w seems most important.

This means that we could have some distance $(d-K)$ between the inner receiver coil and the transmission coil without significantly affecting the receiver signal sensitivity. If we required a very small $(d-K)$ -value, the production of the receiver and transmission coils would have to be very accurate as the transmitted field has much larger gradients close to the transmission coil wire. As long as the receiver coil width doesn't get to small, we have that

$U_{emf,rc, Ia} / U_{tc, I} \approx 4 \cdot 10^{-3}$ at a distance between the water and the coil of $t=6\text{ cm}$ when $r_w = 2\text{ mm}$.

It should be noted that the $U_{emf,rc, Ia} / U_{tc, I}$ -ratio decreases only slowly with increasing shell plate thickness t (or really, separation between the sea and the sensors) when t is below a couple of meters. It should be remembered, however, that shielding effects are ignored.

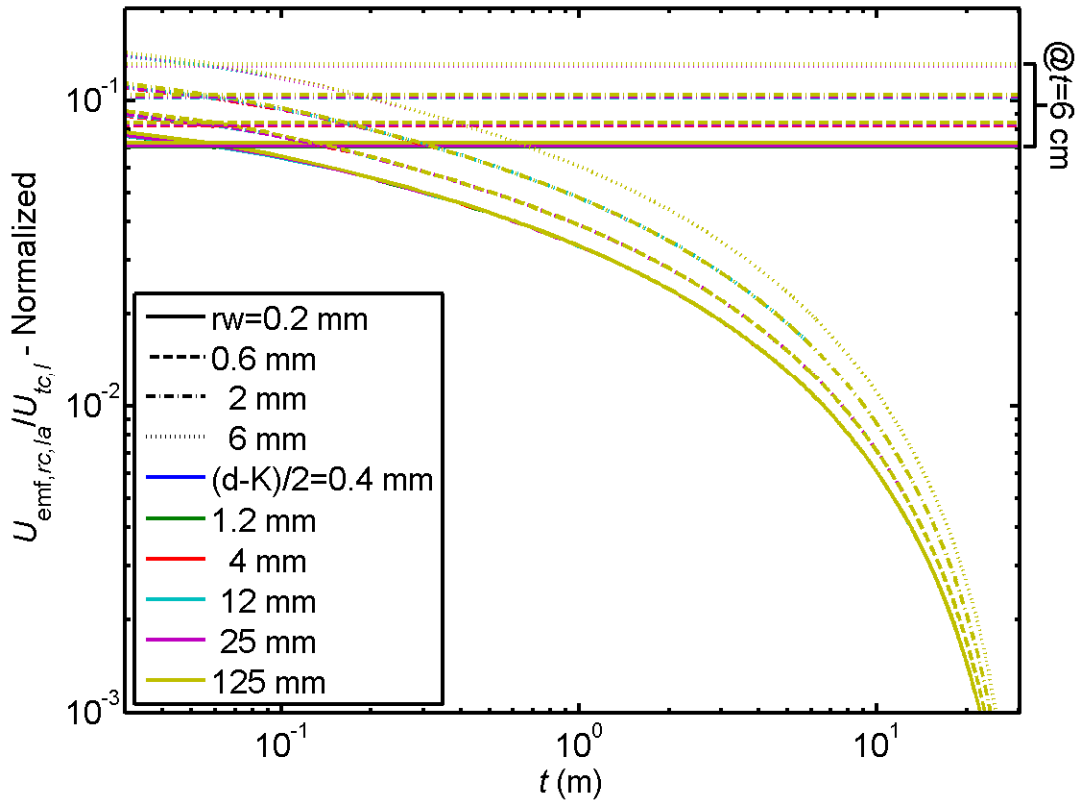


Figure 2.19 As Figure 2.18, but with the ratio normalized such that it corresponds to a single receiver coil turn of width 0.3 m.

In Figure 2.19, $U_{emf,rc,la} / U_{tc,I}$ normalized with respect of the ambient electric noise pick-up of a uniform receiver loop of width 0.3 m is plotted. It is not apparent what the normalization factor should be in this case. In fact, in an electric field uniform across the detector, the pick-up would be zero, since the two loops of the receiver coil then would cancel each other's pick up. The corresponding "normalized" $U_{emf,rc,la} / U_{tc,I}$ ratio would infinite. As will be discussed further in Subsection 2.4, an RF field has limited penetration depth in sea water. Thus, the cancellation of ambient electromagnetic noise fields will not be complete when the sensor is in the sea water, especially close to the surface. Assuming an operating frequency of 100 kHz (a bit higher than anticipated), the water conductivity equal to the maximum found naturally in the oceans of the world (7.7 S/m in the Persian Gulf), that the upper loop of the receiver coil is above the water surface, and that the lower coil is immersed in sea water, we get that the noise pick-up capability is 1/25th of a uniform receiver coil of the same width. This normalization factor in addition to the "ordinary" width normalization is what we have used when calculating the normalized $U_{emf,rc,la} / U_{tc,I}$ -ratio. This, of course, makes the normalized $U_{emf,rc,la} / U_{tc,I}$ -ratio plotted in Figure 2.19 much larger than the corresponding actual ratio plotted in Figure 2.18. The normalized $U_{emf,rc,la} / U_{tc,I}$ -ratio is around 0.1 with $t=6$ cm.

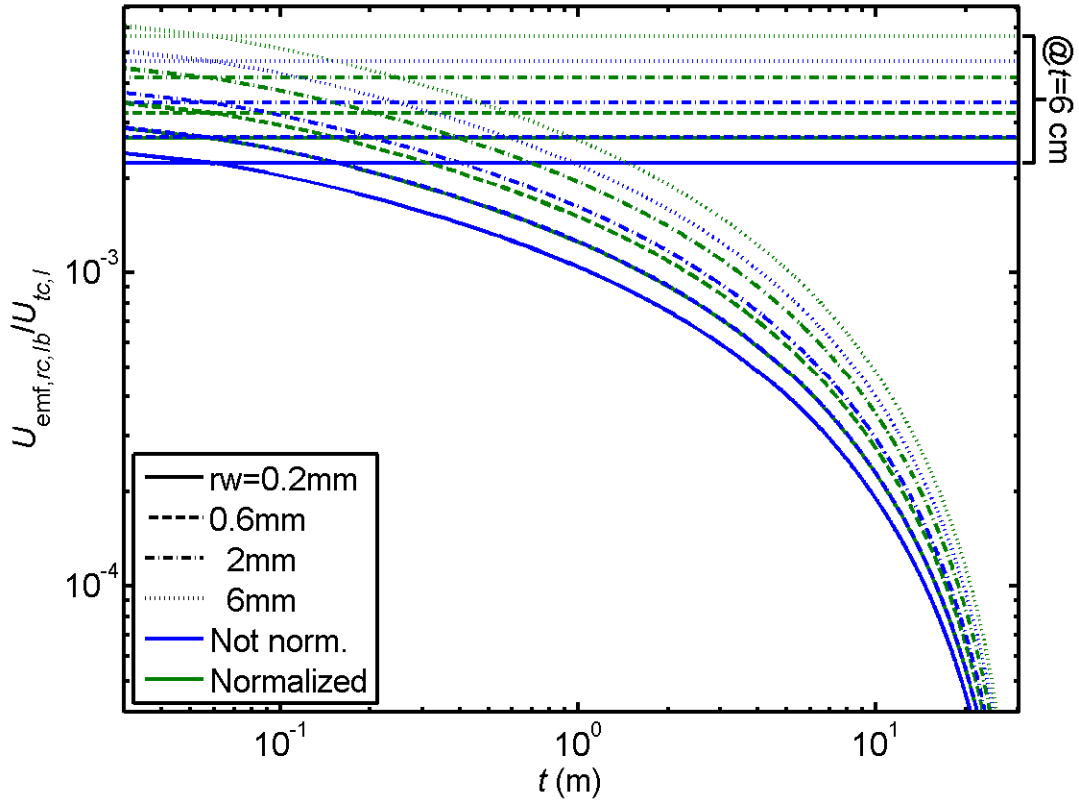


Figure 2.20 A plot of the same ratios as in Figure 2.18 and Figure 2.19, but for coil structure Ib.

In Figure 2.20 both the real and normalized $U_{emf,rc}/U_{tc}$ -ratio is plotted for structure Ib in the most efficient case $\Delta h = 0$. As expected the efficiency is still rather low, however, with the $U_{emf,rc,I_b}/U_{tc,I}$ -ratio being equal to $3.5 \cdot 10^{-3}$ and $4.2 \cdot 10^{-3}$ in the actual and normalized cases, respectively.

For structure Ic, the width of the structure is given by K which we thus set equal to 0.3. The width of the transmitter coil can however be set freely within the limits $6r_w \leq d \leq K - 8r_w$ as long as the $N_{rc,i}/N_{rc,o}$ is set according to (2.49). In Figure 2.21, $U_{emf,rc,I_c}/U_{tc,I}$ is plotted as a function of d for $t=6$ cm. As discussed above, structure Ic is naturally “normalized”. Since we here assume that the inner receiver coil and the inner side of the outer receiver coils lie in contact with the transmitter coil, the wire width r_w is more important for this structure than for coil structures Ia and Ib. Unless r_w is very large, the optimal value of d is quite close to K , and the required $N_{rc,i}/N_{rc,o}$ -ratio correspondingly small, and $U_{emf,rc,I_c}/U_{tc,I}$ is increasing with increasing r_w . With a 6 mm wire thickness, we have that $U_{emf,rc,I_c}/U_{tc,I} \approx 8 \cdot 10^{-3}$. In Figure 2.22, $U_{emf,rc,I_c}/U_{tc,I}$ is plotted as a function of t for the optimum selection of d at $t=6$ cm.

In Figure 2.23, actual $U_{emf,rc}/U_{tc}$ is plotted for coil structure Id for different values of r_w and receiver and transmission coil separation $(d-K)/2$. Because of the coil layout, $(d-K)/2$ is more

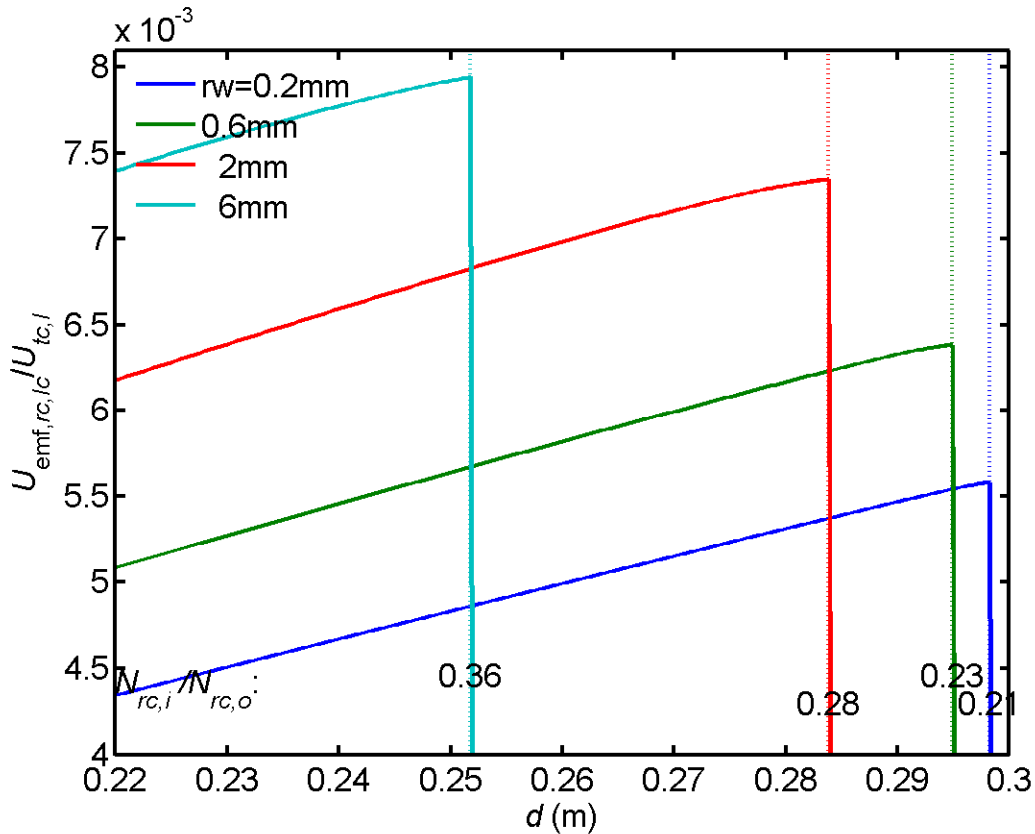


Figure 2.21 Ratio between induced receiver coil emf and required driving voltage of the transmitter coil with $t=6$ cm for coil configuration Ic as a function of transmitter coil width d . The corresponding ratio between the number of turns of the inner and outer receiver coils are indicated at the maximum value. At average, the coil has a single turn (coil surface area averaged).

important for structure Id than Ia, because this parameter directly affects the k/K -ratio. With a coil wire thickness of 2 mm and separation between the transmission and receiving coil of 4 mm (i.e. back to back), the actual $U_{emf,rc,Id} / U_{tc,I}$ -ratio is around $5 \cdot 10^{-3}$.

When normalizing coil structure Id, we assume that the electromagnetic field is uniform in the horizontal direction. Since the current direction of the outer coil is opposite of the inner coil, the effective width of the receiver coil in this case becomes $2k - K$. For smaller values of K , the transmitted field will be more uniform, k and K become almost identical, and the normalization factor becomes very large. This is clearly evident in Figure 2.24, where the normalized $U_{emf,rc,Id} / U_{tc,I}$ -factor is plotted, and the curve with $(d-K)/2=125$ mm stands out as an exception with a normalized $U_{emf,rc,Id} / U_{tc,I} \approx 0.05$ for $r_w=2$ mm and $t=6$ cm. Note, however, that the actual $U_{emf,rc,Id} / U_{tc,I} \approx 6 \cdot 10^{-5}$, and that higher normalized factors were achieved with coil structure Ia without having such a weak actual ratio. When $r_w=2$ mm and the receiver and

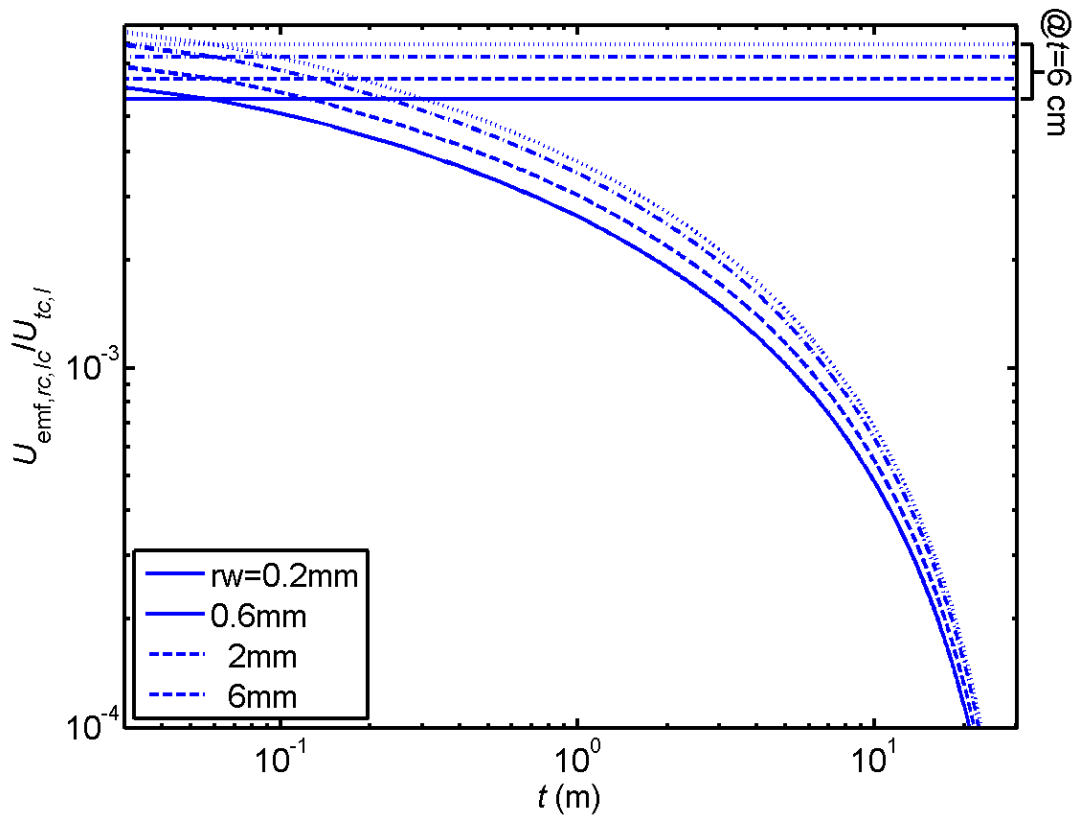


Figure 2.22 As Figure 2.18, but for structure Ic with optimized value of d from Figure 2.21.

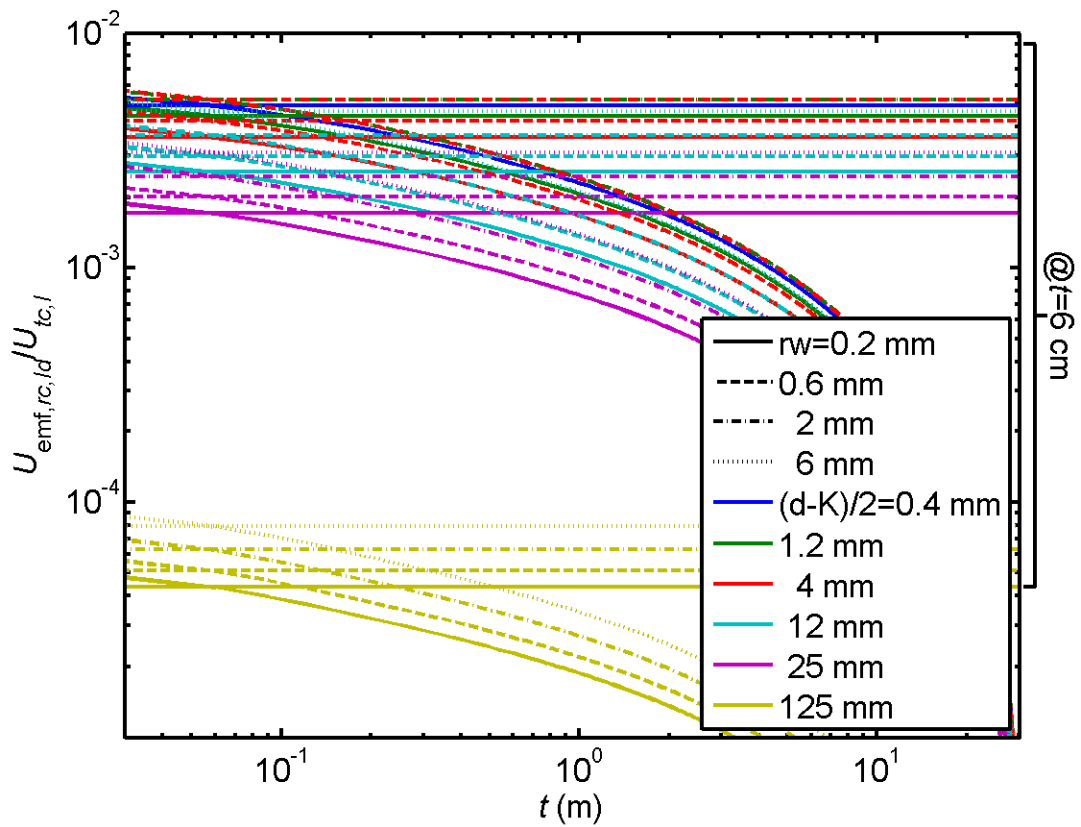


Figure 2.23 As Figure 2.18, but for coil structure Id.

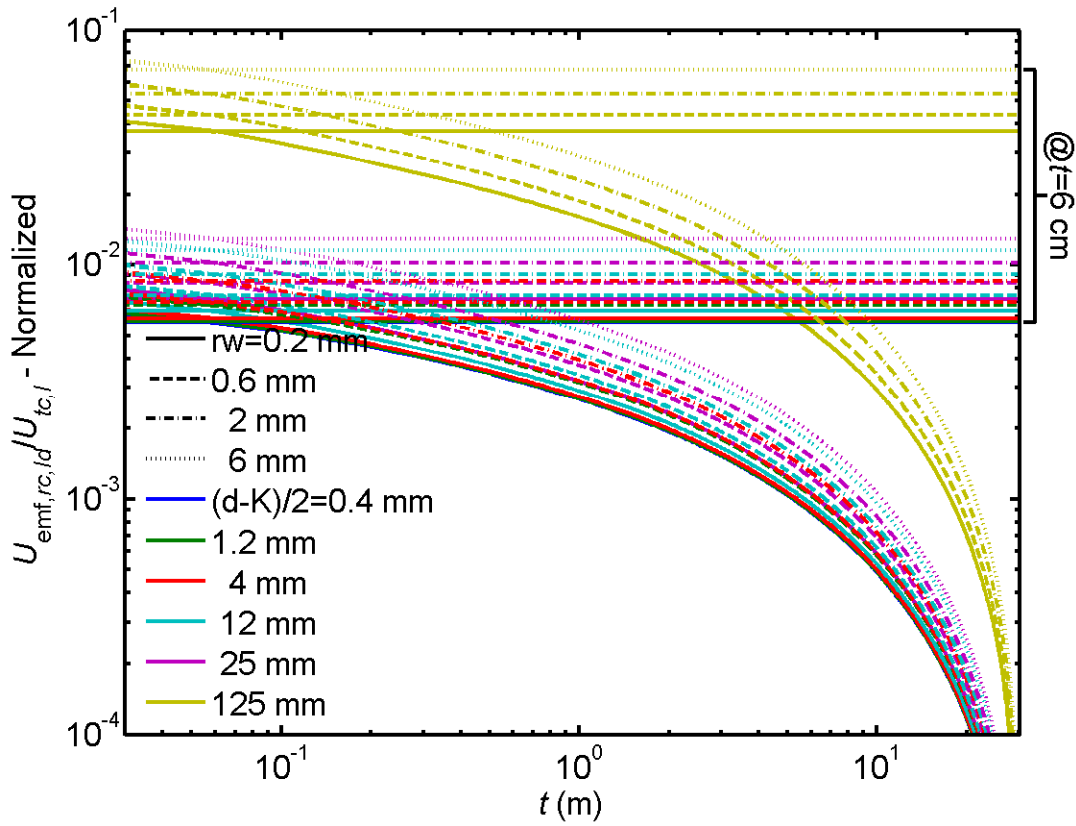


Figure 2.24 As Figure 2.19, but for coil structure Id

transmitter coils are back-to-back ($(d-K)/2=4$ mm), we get that the normalized $U_{emf,rc,Id}/U_{tc,I}$ factor is around $8.4 \cdot 10^{-3}$, only a slight increase from the actual value.

For coil structure IIa, the width of the inner transmitter coil can be chosen within the interval $2r_w \leq d \leq d_{max}$, where

$$d_{max} = \frac{-8r_w + D + \sqrt{D^2 - 16r_w D}}{2} \approx D - 8r_w. \quad (2.65)$$

The last approximation in equation (2.65) is valid for $r_w \ll D$, remembering from equation (2.53) that $K = \sqrt{dD}$. When $d=d_{max}$, the inner transmitter coil is back to back with the receiver coil, i.e. $K = d + 4r_w$. The actual and normalized $U_{emf,rc,IIa}/U_{tc,II}$ -factors are plotted as function of d in Figure 2.25 and Figure 2.26, respectively. Just like for coil structure Ic the largest $U_{emf,rc,IIa}/U_{tc,II}$ -fractions are found for the largest coil wire thicknesses. The maximum actual $U_{emf,rc,IIa}/U_{tc,II}$ -value is found for d/K between $1/2$ and $1/3$, whereas the maximum normalized value is found at the smallest possible d -value, i.e. $d = 2r_w$. In either case, the $U_{emf,rc,IIa}/U_{tc,II}$ -ratio is not very large compared with the other suggested coil structures, with the actual value being less than $3 \cdot 10^{-3}$ and normalized value being around $8.5 \cdot 10^{-3}$. In Figure 2.27, the actual and normalized $U_{emf,rc,IIa}/U_{tc,II}$ -ratios are plotted as a function of t using the optimum d -values at $t=6$ cm found from Figure 2.25 and Figure 2.26.

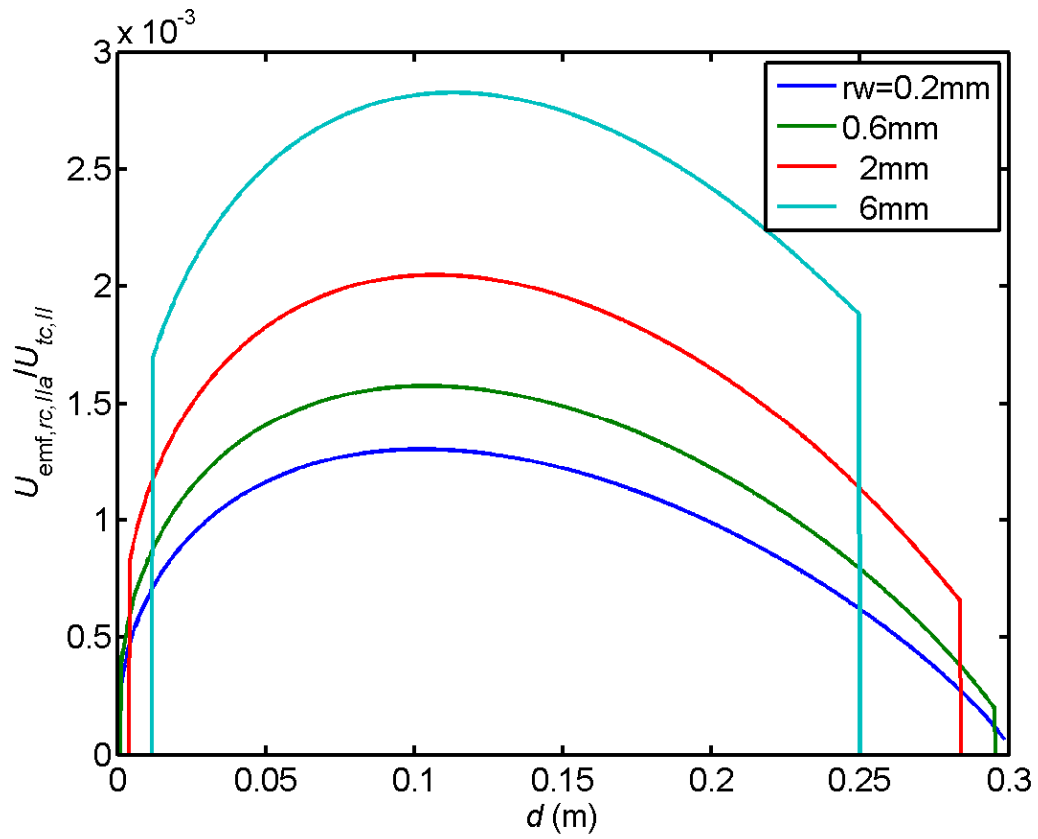


Figure 2.25 As Figure 2.21, but for coil structure IIa.

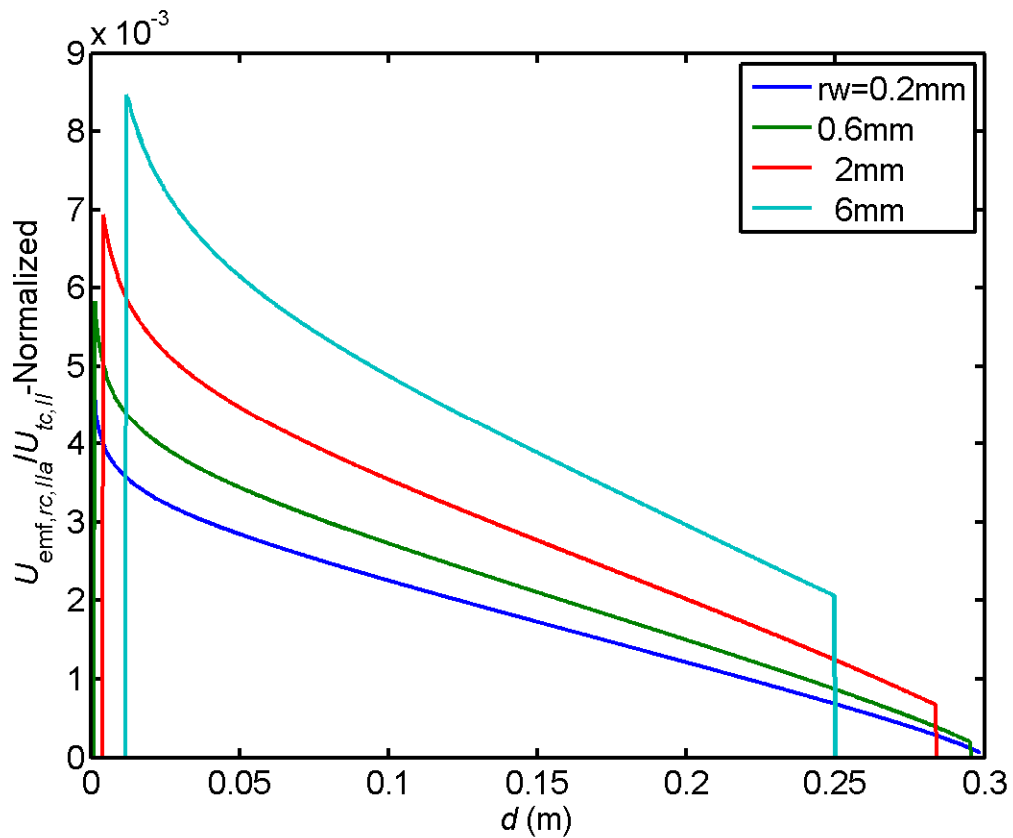


Figure 2.26 As Figure 2.25, but normalized.

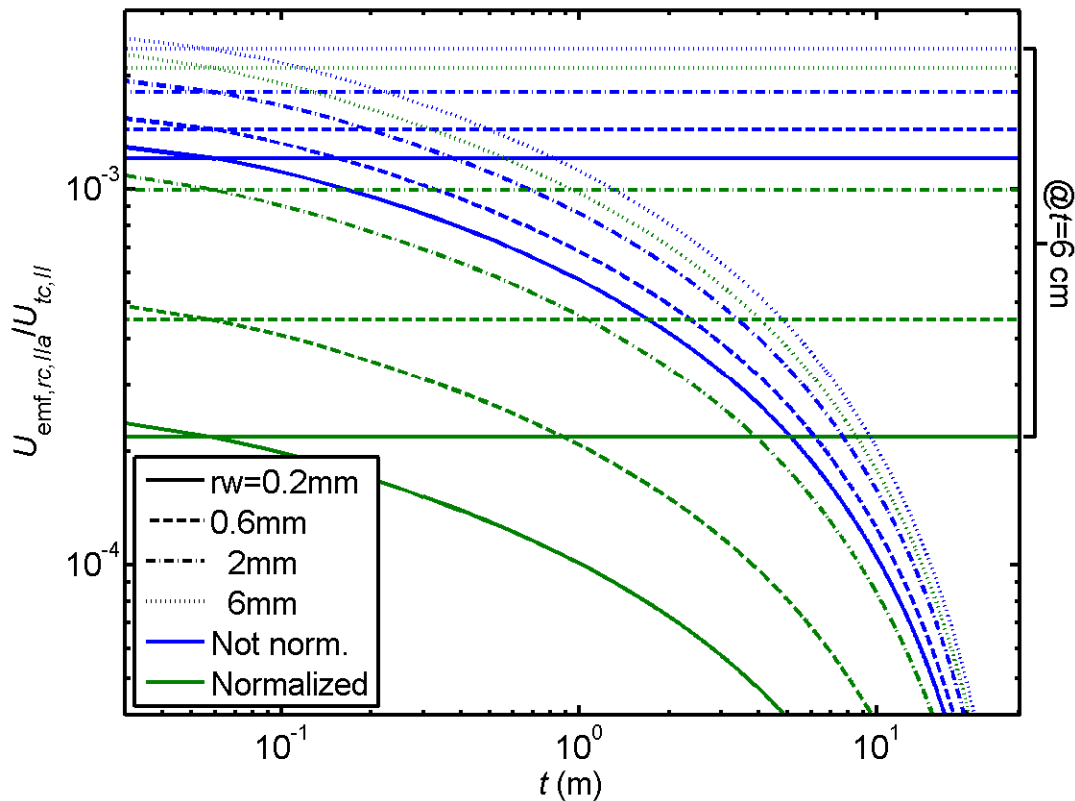


Figure 2.27 As Figure 2.22, but for structure IIa.

2.2.2.5 Summary Theoretical Considerations

For low frequencies, the response of both BFO and IB sensors are proportional to the frequency squared, and the response does not decrease much with increasing coil/water separation t , as long as t is less than a few meters. However, due to the RF-shielding of the sea water, i.e. higher order induction terms, the optimum driving frequency of the system is probably less than 100 kHz in most sea waters, and t should not be much larger than the desired resolution. For induction sensors the signal strength in theory scales with the product of the number of turns of the receiver and transmitter coils. Also the driving power scales proportionally to the number of turns of the transmitter coil, however.

BFO sensors are attractive in the respect that the coils can be made very simple, but they are generally not as sensitive as IB sensors, and there will be cross talk between sensors. If it is possible to decrease the sea-coil distance, however, by for instance incorporating the sensor coil in the shell plate, the sensor coil can be made much smaller, however, and resolution will not be a problem.

The IB sensors can be made more sensitive than BFO sensors, and using a common transmitter coil, the receiver coils can be multiplexed to the desired resolution. There are very many ways of making such coils, and of the coil structures we have investigated, illustrated in Figure 2.14, coil

structure Ia seems to be promising alternative. The design is fairly simple, and it has a reasonably high absolute signal level, only structure Ic is significantly higher. Coil structure Ia has very low susceptibility to external electromagnetic noise. One disadvantage of IB sensors is that the coils have to be made or tuned quite accurately, so that no emf is induced in the receiver coil directly from the transmitted signal.

2.2.3 Experiments

Different induction based sensors were investigated using a rather large plastic pan ($l \times w \times h = 0.6 \times 0.4 \times 0.25 \text{ m}^3 \approx 60 \text{ liter}$). The pan was filled to the rim with water with 3 % salinity (NaCl), and the various sensors were placed above the surface of the water. To make the tests a bit more realistic, we did also measure through a sample shell plate used in the bow of the Skjold class vessels. The shell plate was not painted, but according to the manufacturer, the Sealion ship-bottom paint/fouling release coating that will be used on Skjold is not conductive. The metal detectors were also investigated outside a small jetty by Oslofjorden.

2.2.3.1 Commercial Metal Detectors



Figure 2.28 Velleman CS100 metal detector

A few commercially available metal detectors, Velleman CS100 and Velleman CS150 being the most advanced, were investigated. The Velleman detectors were based on the IB principle. They were able to detect the salt water when placed in close proximity to the water surface. They seemed to work at 6-10 cm distance from the water surface or through the shell plate after a lot of tuning, but it was less stable. This was not very surprising considering that many metal detectors actually are designed to filter out salt water signal, and that the diameter of the transmitter coil was less than 19 cm (for some considerably less), and the area enclosed by the receiver coil probably was a quarter of that.

2.2.3.2 ELFA Metal Detector Kit ("Byggsats 1022/Smart D1022")

This was a simple metal detector kit provided by ELFA, an assembled version is shown in Figure 2.29. Two coils are wound around a 6 cm ferrite rod. The two coils are part of a electronic circuit that is close to oscillation. By introducing a conductive medium close to the ferrite rod, the inductance of the two coils is changed and the circuit starts to oscillate, causing a small diode

lamp to light up. I.e., this detector is just like the BF detectors based on a change of inductance of the sensing coils. The oscillation threshold can be tuned by adjusting a potentiometer.

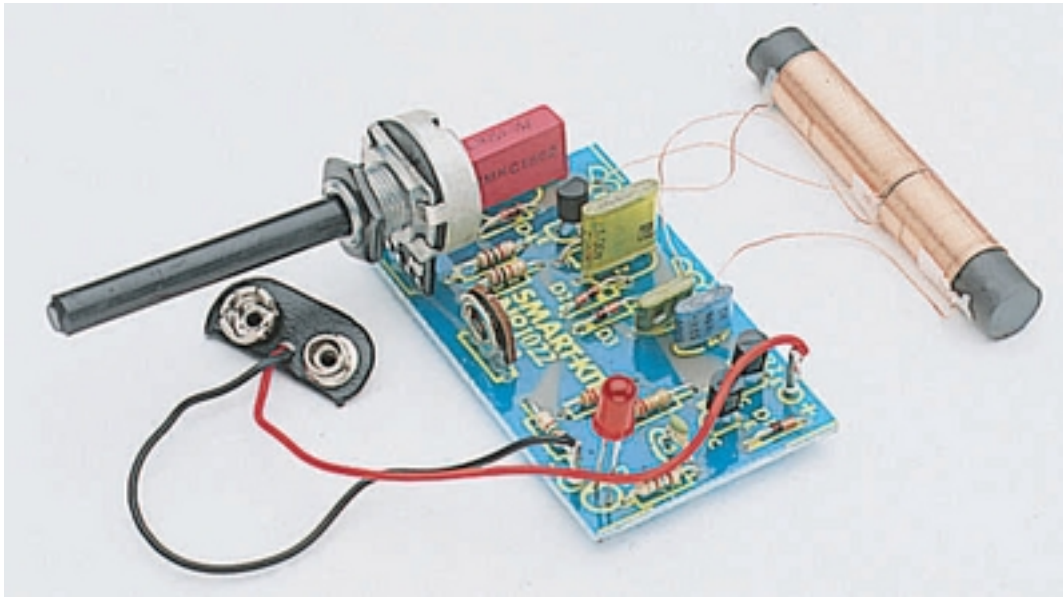


Figure 2.29 Elfa detector kit (Smart D1022)

It was possible to induce oscillation by placing the rod close to the salt water. However, it was not possible to introduce oscillation at 6 cm distance or through the shell plate of the Skjold class.

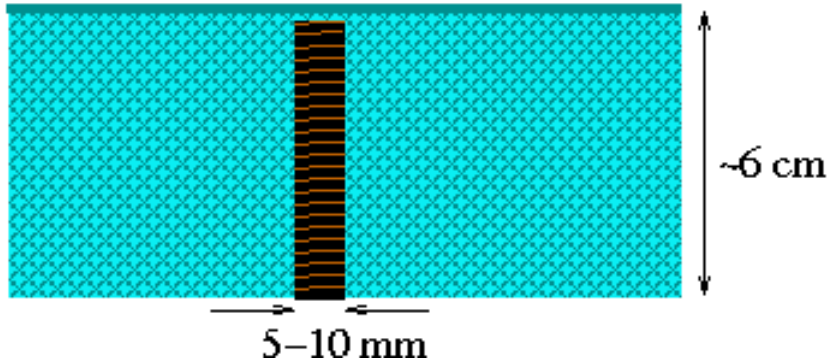


Figure 2.30 Introduction of ferrite rod coil into the shell plate of the Skjold class

In a further experiment, a small hole was drilled almost to the outer surface of the shell plate, and the ferrite rod was placed into the hole, as shown in Figure 2.30. Interestingly, the circuit started to oscillate when the plate was placed in contact with the salt water of the plastic pan. However, no signal was detected when the surface of the plate was only wetted with salt water.

2.2.3.3 Implementation of IB Sensor with Coil Structure Ia



Figure 2.31 Preliminary experimental coils for IB concept Ia.

Structure Ia was implemented with a single receiver coil with $\Delta h = 10$ cm, $d = 30$ cm, $K = 26$ cm, $N_{tc} = 4$, and $N_{rc} = 46$. The total height of the transmitter coil was 56 cm, and the transmit coil wire thickness was $r_w \approx 1$ mm. The coil structure was manually wound on a 6 mm thick sheet of plastic, as shown in Figure 2.31. Using a signal generator and audio-amplifier, a 0.5 A AC current was sent through the transmitter coil at frequencies varying between 5 and 100 kHz. As a safety measure, an 18Ω resistor was placed in series between the amplifier and the transmitter coil. Since both the transmit coil and receiver coil were made quite coarsely, it turned out to be quite difficult to achieve complete induction balance, and even small movements of some of wire in the receiver coil lead to quite large changes in the background signal. Thus, it was rather difficult to detect the rather weak return signal from the salt water.

The peak signal condition with the receiver coil around the water surface was simulated by sandwiching the shell plate from Skjold between the salt water pan and the receiver coil, with one of the loops of the coil above the salt water and the other one just outside. A change in voltage corresponding to about 5 % of the background signal was detected. The ideal frequency turned out to be around 50 kHz. The coil was also tested simply by placing a large copper coil 6 cm above one of the loops of the receiver coil, which of course resulted in a large signal. When placing the shell plate between the large copper coil and the receiver/transmitter coil, a 20 % reduction in signal was detected.

2.2.4 Concluding Remarks Regarding Inductive Techniques

Inductive loops have been investigated both theoretically and experimentally. Coils should preferably be wider than the shell plate thickness if they are placed inside the hull. Further, quite high current levels are probably required; of the order of 1 A. The actual current level will be dependent on the final physical and electrical design. One meter away, 1 A in a single long transmitter coil will correspond to a magnetic field strength of 0.6 nT/A, which would be well within both health and EMC standards.

The preliminary experiments have clearly illustrated the need for accuracy when winding the receiver coils, and that the coils subsequently will have to be fixed in their entire length, perhaps using epoxy. Still, the robustness of a system of coils attached from top to bottom in the bow of the boat can be put into question.

By inserting inductive coils into the shell plate, and thus getting much closer to the sea, the coils can be made much smaller, and current consumption would also be considerably smaller. From a sensor lifetime point of view, this will be a better option. The experiments we have done have indeed shown that such much smaller sensors is a viable alternative, although they might be more vulnerable to sea spray.

2.3 Capacitive Techniques

2.3.1 Operating Principle and Theoretical Considerations

The idea here is to utilize that there is a finite capacitance between two conducting surfaces separated by a dielectric. As is well known, the capacitance C between two large conducting plates of area A separated by a dielectric with a small thickness d and permittivity ε is given by:

$$C = \frac{\varepsilon A}{d} \quad (2.66)$$

This expression is ignoring edge effects, i.e. it is only valid as long as d is much shorter than the length and width of the plate. The conducting surfaces does not need to be metal, also for instance salt sea water is conducting. Thus, it is possible to conduct a RF signal between a metal plate to a parallel salt water surface, and back again to another surface. Alternatively, if the interrogating circuit is grounded to the sea, the second metal plate is not necessary. Capacitive techniques are frequently used as level sensors in tanks as well as a range of other different applications, for instance touch sensors [4].

From equation (2.66), the admittance¹ between the sea and such a metal plate will be proportional to the plate areas A , RF frequency, permittivity ε and inversely proportional to the distance between the plate and the water d . Of course, if there is no continuous layer of salt water outside and between the two metallic plates, the impedance become quite high, and the parasitic capacitance directly between the plates will dominate.

¹ Inverse impedance

A number of different plate conductor configurations were considered. Considerations similar to the ones discussed in connection with conductance sensors in Section 2.1.1 can be made regarding sensitivity to water films on the outside of the hull. However, if the conducting plates are placed inside the hull, the plates probably will have to be so large that cross talk due to water films will not be an issue. As discussed above, the impedance between the plates and the sea water will decrease with increasing RF frequency. However, if the frequency becomes too high, the resistance in the salt water becomes significant.

The capacitive sensors can be made insensitive to objects inside the hull by covering the sensing plate with a grounded shield, as illustrated in Figure 2.32.

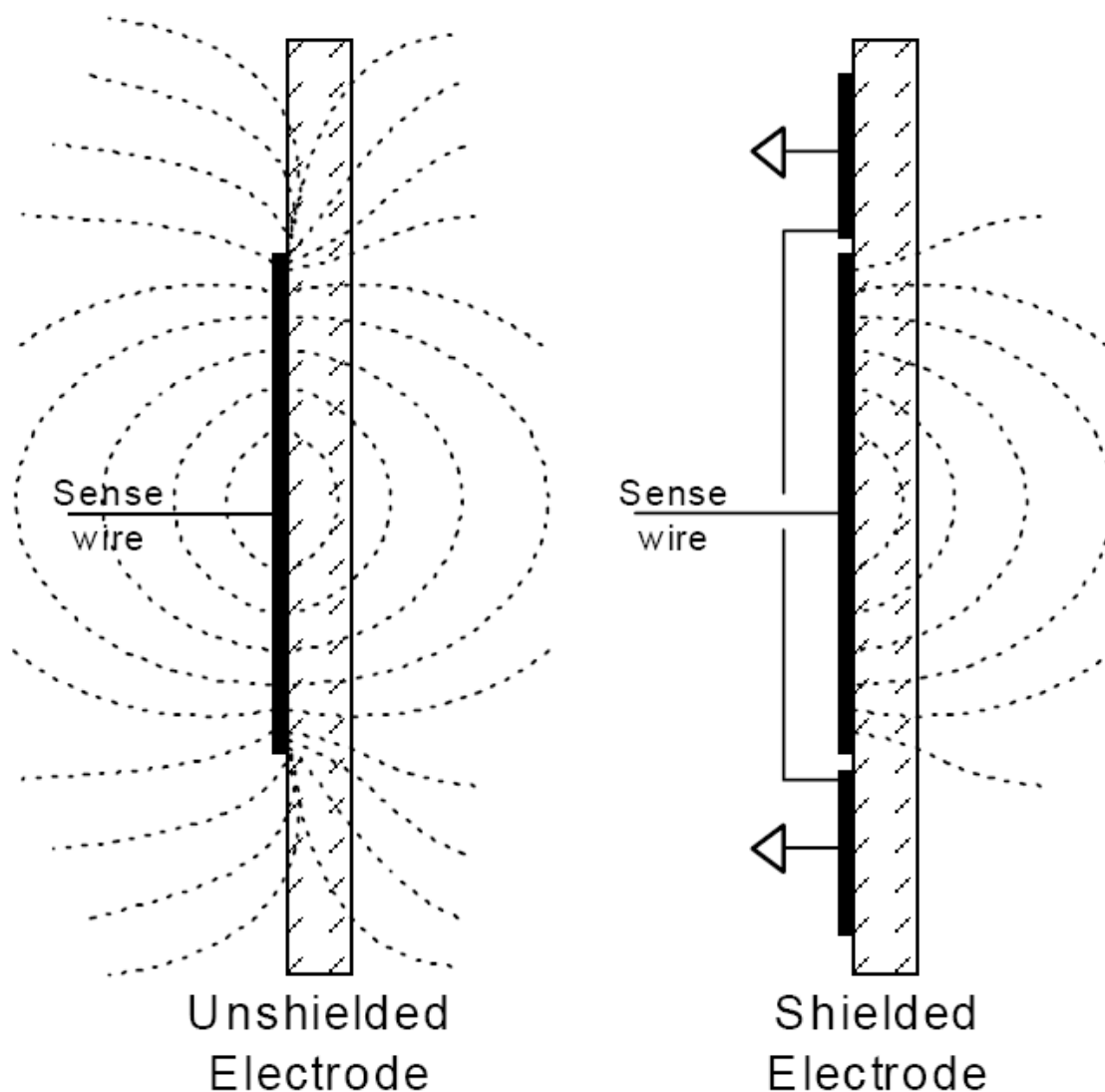


Figure 2.32 Shielded and unshielded capacitive sensor (from [4])

2.3.2 Experiments

2.3.2.1 Large Metal Plates Tested with Air-Gap between Salt Water and Capacitive Sensors

Table 2.2 Tested large place capacitive sensor electrode configurations

Sensor label	Electrode Length (cm)	Electrode Width (cm)	Electrode Separation (cm)	Distance water electrodes when measuring Y_0 (cm)
A	17	17	20.5	19.6
B	10	20	37.0	19.6
C	10	20	20.0	19.6
D	20	10	19.0	19.6
E	20	10	10.5	19.6
F	20	20	18.7	34.1
G	20	40	19.0	19.6

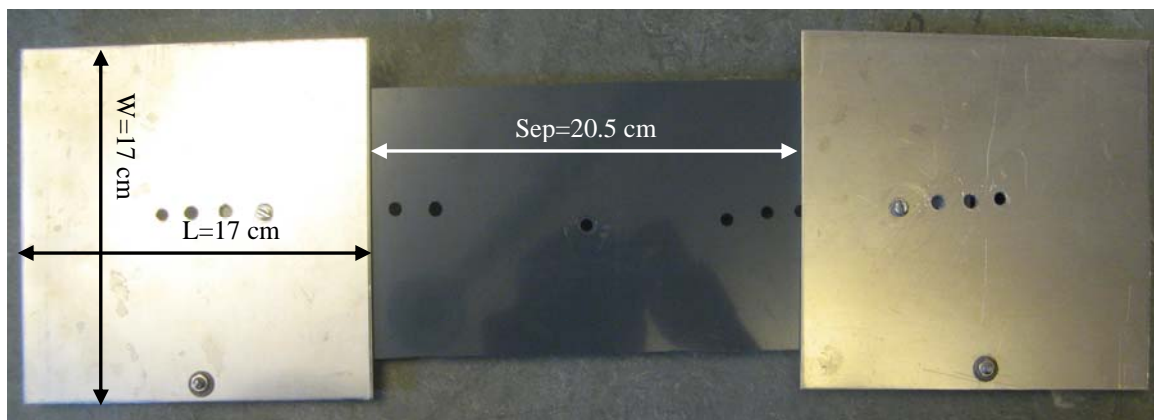


Figure 2.33 Large plate capacitive sensor A

A few different capacitive sensors with two metal plate electrodes were tested as capacitive sensors. The different configurations are listed in Table 2.2, and a picture of sensor A is given in Figure 2.33. A signal generator was connected to one of the plates, whereas the other plate was grounded. The current load of the signal generator was then measured when the plates were separated by a 6 cm air gap from and parallel to the salt water surface provided by the same plastic pan discussed in Section 2.2.3. The metal plate structure was then raised to the height given in the last column of Table 2.2. This current is probably dominated by the parasitic capacitance directly between the plates. Finally, the current was measured after disconnecting the wires from the electrode plates. This current is caused by parasitic capacitance between the lead wires. By dividing the measured currents with the transmitted voltage (7.2 V RMS), the admittance Y are found for the three cases. The admittance equals the inverse impedance. The results are shown in Figure 2.34. In Figure 2.35 the ratio between the signal admittance when the plates are 56 cm from the salt water surface, $Y_{6\text{cm}}$, and the measured admittance when the plates are removed from the water, Y_0 . The capacitive sensors with the

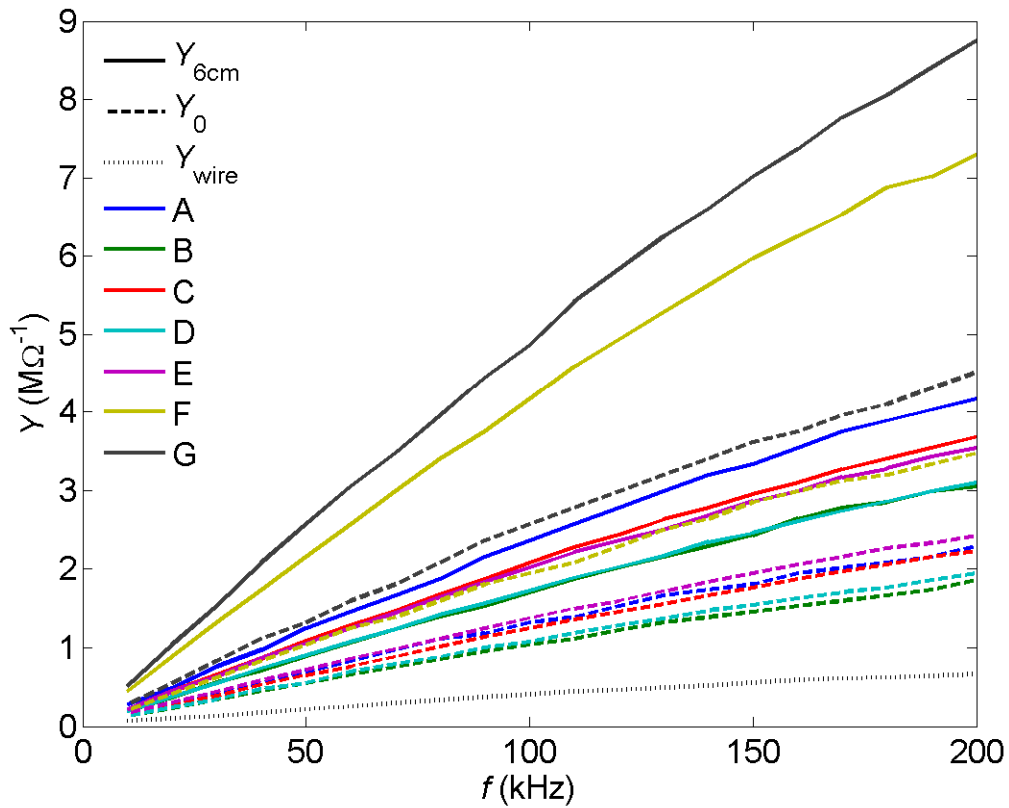


Figure 2.34 Measured admittance of the different large plate capacitive sensors 6 cm ($Y_{6\text{ cm}}$ - solid line) and "high" (Y_0 - dashed line) above the water surface. The admittance measured between the lead wires are also indicated (Y_{wire} - dotted line)

largest plates, capacitive sensors F and G, have both the largest absolute ($Y_{6\text{ cm}}$) and relative ($Y_{6\text{ cm}}/Y_0$) signal admittance, which is as expected from equation (2.66).

In Figure 2.36, the difference between the signal admittance $Y_{6\text{ cm}}$ and the "leakage" admittance Y_0 is normalized with the frequency f and the total effective plate area defined from:

$$A_{\text{plate } 1||2} = \frac{A_{\text{plate } 1} A_{\text{plate } 2}}{A_{\text{plate } 1} + A_{\text{plate } 2}} \quad (2.67)$$

Here $A_{\text{plate } 1}$ and $A_{\text{plate } 2}$ are the areas of the two metal plates, and hence $A_{\text{plate } 1} = A_{\text{plate } 2} = A_{\text{plate}}$, and consequently $A_{\text{plate } 1||2} = A_{\text{plate}}/2$ for all capacitive sensor types listed in Table 2.2 except capacitive sensor F. Also indicated in the figure is the theoretical value for two pairs of infinitely large plates separated by vacuum at a distance 6 cm. Deviation from this theoretical value is certainly expected. Firstly, one of the "plates" in the capacitor is not made of highly conductive metal, but of salt water, which makes the effective distance between the capacitor plates a bit larger than 6 cm. Secondly, there will be a frequency dependence resistivity in the sea water. Both effects will reduce the admittance with respect to the vacuum value, and this is confirmed by the experimental results plotted in Figure 2.36. The negative slope of all the curves are probably due to the increase in salt water resistivity as a function of frequency.

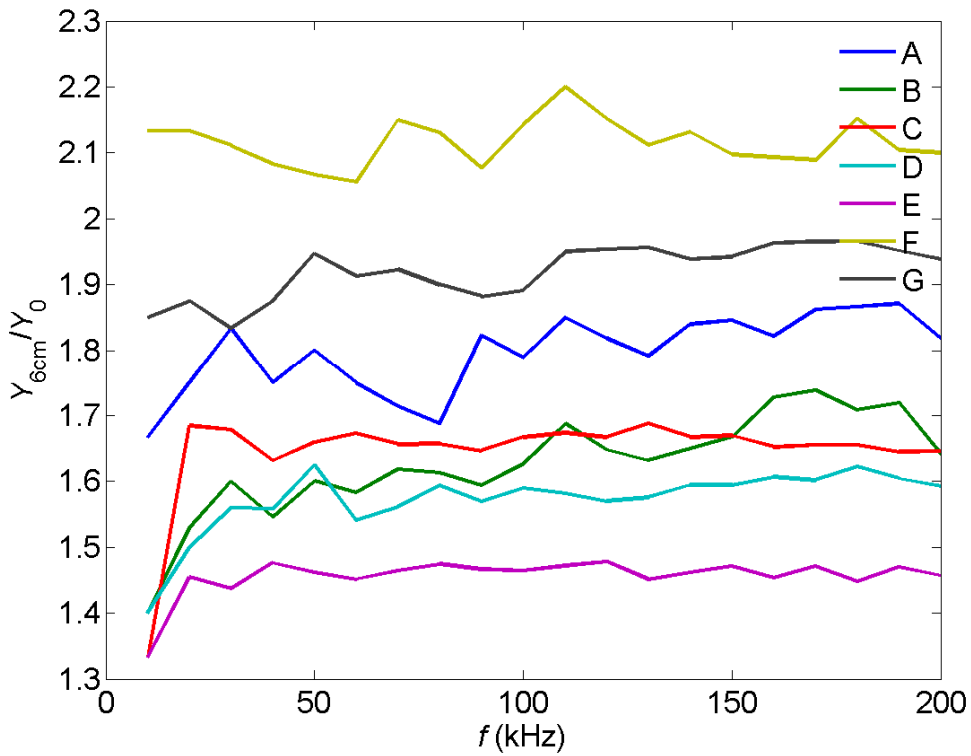


Figure 2.35 Ratio between Y_{6cm} and Y_0 plotted in Figure 2.34.

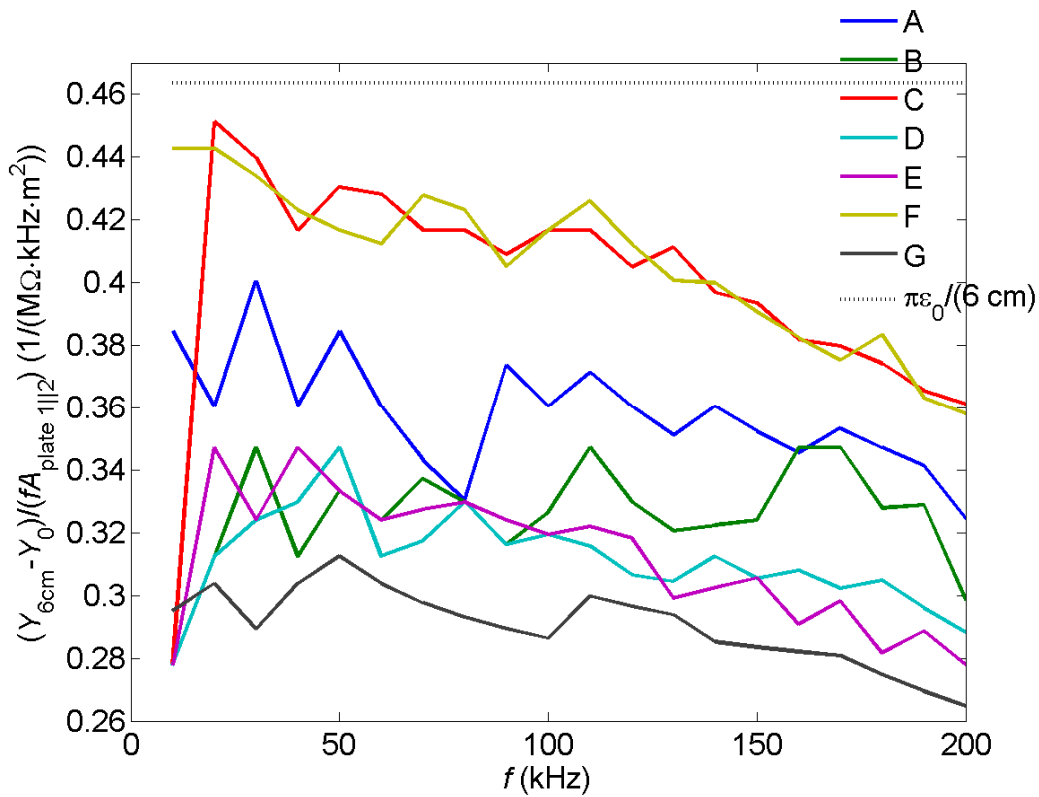


Figure 2.36 Difference between Y_{6cm} and Y_0 plotted in Figure 2.34 normalized with respect to the plate electrode surface areas and frequency. The theoretical potential value in vacuum for a large capacitor is plotted with a dotted line.

The experimental results shown in Figure 2.34 - Figure 2.36 are preliminary, and caution should be used when making quantitative comparisons between the different designs. What should be clear, however, is that the principle of the technique is proven.

2.3.2.2 Large Metal Plates Tested behind Skjold Class Shell Plates

Some of the sensors listed in Table 2.2 and discussed in the previous subsection were placed on top of a 1 m x 0.5 m Skjold shell plate, which then was placed on top of the sea water pan discussed above. I.e., instead of air, the gap between the capacitive sensors and the water was now more realistically filled by the shell plate. Unfortunately, even though the permittivity of the shell plate is higher than of air, it was no longer possible to detect an increase in the admittance. This is believed to be caused by a slightly conducting layer in the shell plate. Thus, these preliminary tests indicate that capacitive sensors on the inside of the Skjold class hull are probably not a viable sensor alternative. However, such simple capacitive sensors could very well be a good solution for the Oksøy/Alta class.

2.3.2.3 Smaller Capacitive Sensors Embedded in the Skjold Class Shell Plate

Similar to the inductive sensors discussed in Subsection 2.2.3.2, it is possible to shorten the distance between the sensor head and the measurand (in this case sea water) by embedding a capacitive sensor just inside the outer layer of the shell plate. In addition to allow for smaller detector footprint, an added advantage for a capacitive sensor is that it is possible to cut through the conductive layer. A limited test was performed by boring a hole with a diameter of roughly 6 cm through the shell plate except the outer epoxy layer which was left intact. In the hole a metallic, but isolated disk was placed. A QProx™ QT113 circuit from Quantum research group specifically made to detect changes in capacitance [4] was connected between the disk and the conductive (and drilled-through) layer of the shell plate. Using this setup, nearby salt water was indeed detected. However, also a water film on the surface of the shell plate was detected. The reason is that this sensor in practice acts as a conductance sensor. For a reasonably good resistance against surface water, the discussion in Subsection 2.1.1.2 concluded that the separation between the wires should be at least 10 cm. Translated to this case, that means that the diameter of the hole should be at least 0.2 m plus the diameter of the disk. Thus, although embedding a capacitive disk into the shell plate probably will provide high sea water sensitivity, making it immune to sea spray and water film may involve a deterioration of hull strength and/or radar signature.

2.4 Radio Attenuation Detection Array

2.4.1 Concept and Theoretical Considerations

The reason that the reach of electromagnetic waves in a conducting medium is limited is that inductive processes set up an electromagnetic field that opposes the initial one. In Section 2.2, various ways of detecting this induced field was discussed, which will be a second order process. The idea here is instead to measure the initial field, which will be a process of first order and also have many other potential advantages.

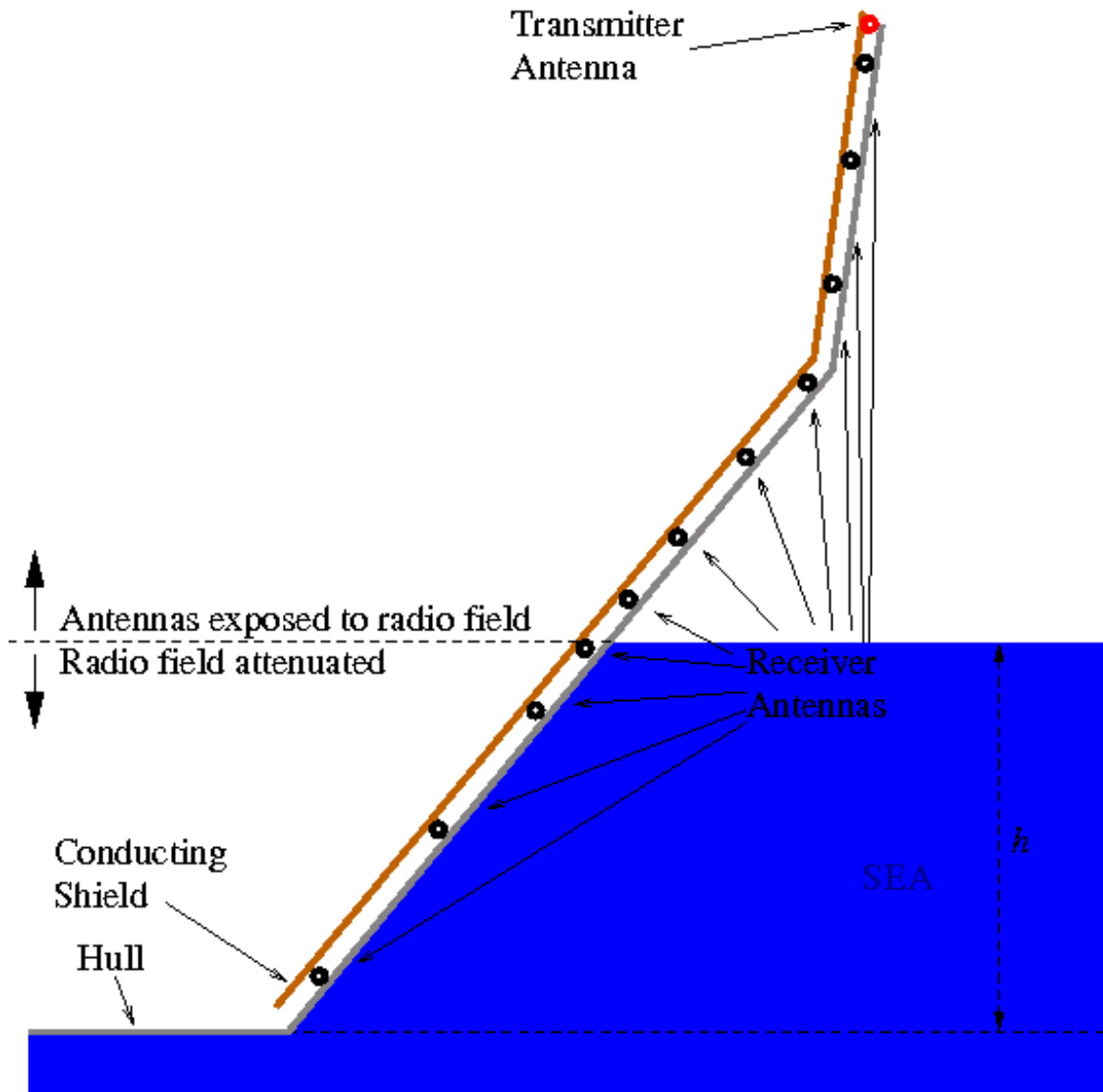


Figure 2.37 Suggested sensor system for the measurement of radio wave attenuation

In Figure 2.37, a suggested system to measure the relative wave height by utilizing the limited penetration depth of RF waves in sea water is illustrated. A radio transmitter is placed at the top of the bow. An array of antennas is placed from the top of the bow down to the keel, at an interval determined by the desired local measurement accuracy. Immediately behind the antennas, a conducting shield should be mounted, so that no radio waves can reach the antennas from inside the ship.

Above the water surface, the transmitted RF signal will travel freely and almost lossless to the antennas. As discussed in Subsection 2.2.2.1, however, the RF waves will be attenuated below the water surface, and the attenuation is characterized by a length called the penetration depth given by:

$$\delta_{sw} = \frac{1}{\sqrt{\pi\mu_0\sigma_{sw}f}} \quad (2.68)$$

The penetration depth is the depth where the amplitude of a normal incident field has fallen to $1/e$ of the value at the water surface. σ_{sw} is the electrical conductivity. The sensor/antenna array can find the relative wave height by utilizing the contrast between the clear RF signal above the water and the exponentially falling signal strength below the water surface.

2.4.1.1 Selection of Operating Frequency

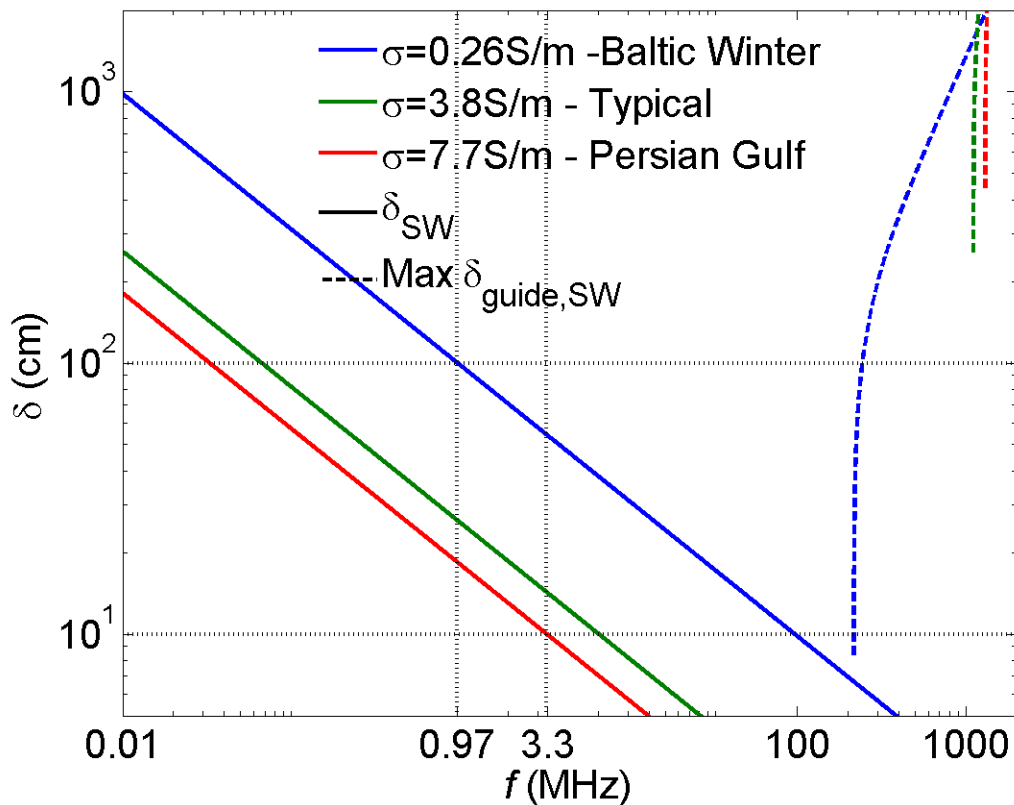


Figure 2.38 Penetration depth of electromagnetic waves in sea water as function of frequency for different sea water electric conductivities plotted with solid line. With dashed line is the corresponding penetration depth of the planar waveguide created below the water surface, between the sea and the conductive screen behind the antennas. The physical width of this waveguide is assumed to be 7 cm

As discussed in Subsection 2.1.1, typical conductivity in Norwegian waters is around 4 S/m, but the ship may be exposed to conductivities between 0.25 and almost 8 S/m in other oceans of the world. As illustrated in Figure 2.38, the lower limit in conductivity leads to a penetration depth that is almost four times higher than the typical value found in Norwegian waters. The penetration depth probably has to be less than 1 m, preferably less, in order to have a measured wave height resolution of less than 0.1 m. In the “Baltic winter” scenario that is only possible with a radio frequency above 1 MHz.

Below the water surface, the water/hull interface and the conducting shield will in effect constitute a planar waveguide, which can have different attenuation characteristics than the surrounding water. Such waveguides have two types of modes, TE modes with the electric field

normal to the propagation direction and parallel to the waveguide walls (i.e. conducting shield or sea water surface), or TM modes with the magnetic field normal to the propagation direction and parallel to the waveguide walls. For metallic waveguides, it can be shown that for both TE and TM modes, the lowest so called cut-off wavelength λ_{cutoff} and cut-off frequency f_{cutoff} are given by (see for instance [5]):

$$\lambda_{\text{cutoff}} = \frac{c}{f_{\text{cutoff}}} = 2a_{\text{guide}} \quad (2.69)$$

Here a_{guide} is the thickness of the waveguide and c is the speed of light, and as is customary in optics, λ_{cutoff} is related to the wavelength in vacuum. Below the cutoff-frequency, an ideal lossless planar waveguide has a rather high attenuation α given by [5]:

$$\alpha_{\text{guide,ideal}} = \frac{2\pi}{\lambda_{\text{cutoff}}} \sqrt{1 - \left(\frac{f}{f_{\text{cutoff}}}\right)^2} \quad (2.70)$$

In practice however, all waveguides have walls with finite conductance, and in practice no modes can propagate below the cut-off. Above the cutoff-wavelength of the lowest order mode, the loss of ordinary metallic waveguides is given by [5]:

$$\alpha_{\text{guide,metal}} = \frac{c^2}{2a_{\text{guide}}^3} \sqrt{\frac{\pi\epsilon_0}{\sigma f^3 \left[1 - \left(\frac{f}{f_{\text{cutoff}}}\right)^2\right]}} \quad (2.71)$$

At the cut-off frequency, the mode loss approaches infinity.

The planar waveguide created by the metal shield differ significantly from a pure metallic waveguide since it has a rather “soft” wall at the sea-side due to the low conductivity of sea water compared with metal, and the theory has to be modified. This is in practice a quite complicated problem, and just rough estimates/hand waving arguments will be made here. The effective waveguide thickness to be inserted in equation (2.69) and (2.71) we define by:

$$a_{\text{guide,SW}} \approx \sqrt{\epsilon_{\text{r,comp}}} t_{\text{shield}} + \sqrt{\epsilon_{\text{r,SW}}} \delta_{\text{SW}} \quad (2.72)$$

Here t_{shield} is distance from the metallic shield to the sea water/hull interface, and $\epsilon_{\text{r,comp}}$ and $\epsilon_{\text{r,SW}}$ are the relative (real) dielectric constants of the composite material of the shell plates and sea water, respectively. Note that $a_{\text{guide,SW}}$ defined as in equation (2.72) is an “optical” rather than physical width. $\epsilon_{\text{r,comp}}$ is mostly dominated by the core material, which has a rather low permittivity. We will use $\epsilon_{\text{r,comp}} = 1.16$ based on data related to the core materials actually used on Skjold and Oksøy/Alta. $\epsilon_{\text{r,SW}}$ is generally dependent on salinity, temperature and frequency, and can be calculated using a rather complex Debye model [6]. The permittivity for different types of sea water is plotted in Figure 2.39. The frequency dependence is relatively small below a few hundred MHz. The permittivity is decreasing slightly as a function of temperature and salinity. For typical Norwegian conditions, with a temperature of 10 °C and a salinity of 3.5 %, $\epsilon_{\text{r,SW}} \approx 76$. At 34 °C and a salinity of 4.4 % (possible in Persian Gulf), $\epsilon_{\text{r,SW}} \approx 67$, and at 0 °C and 0.3 % salinity (possible in Gulf of Bothnia), $\epsilon_{\text{r,SW}} \approx 87$. Assuming a constant permittivity as a function of cutoff frequency f_{cutoff} of the planar waveguide can be found by solving:

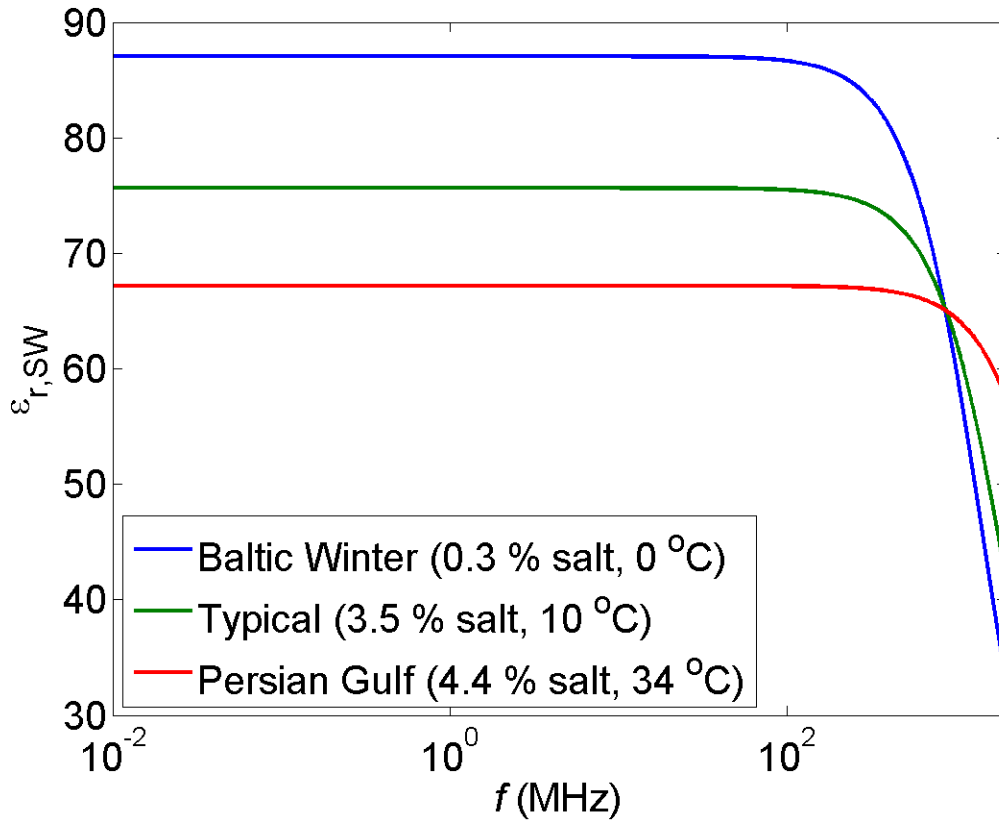


Figure 2.39 Real permittivity $\varepsilon_{r,SW}$ as a function of frequency for different types of sea water according to [6].

$$\frac{c}{f_{\text{cutoff}}} \approx 2 \left[\sqrt{\varepsilon_{r,\text{comp}}} t_{\text{shield}} + \sqrt{\varepsilon_{r,SW}} \delta_{\text{SW}} (f_{\text{cutoff}}) \right] \quad (2.73)$$

c is the speed of light. This equation can be solved by inserting equation (2.68), and the rather complicated result is:

$$f_{\text{cutoff}} \approx \frac{\chi + \sqrt{\varepsilon_{r,\text{comp}}} t_{\text{shield}} c - \sqrt{\chi^2 + 2\sqrt{\varepsilon_{r,\text{comp}}} t_{\text{shield}} c \chi}}{2\varepsilon_{r,\text{comp}} t_{\text{shield}}^2}, \quad (2.74)$$

where

$$\chi = \frac{\varepsilon_{r,SW}}{\pi\mu_0\sigma_{\text{SW}}}. \quad (2.75)$$

Equation (2.74) is strictly valid only when the permittivity can be assumed constant. Numerical solution of equation (2.73) with frequency dependent permittivity however reveals that the deviation is less than 10 % for cut-off frequencies up to 1.3 GHz. With 0 °C temperature and 0.3 % salinity, $f_{\text{cutoff}} \approx 0.22$ GHz, for 10 °C temperature and 3.5 % salinity, $f_{\text{cutoff}} \approx 1.1$ GHz, and for 34 °C temperature and 4.4 % salinity, $f_{\text{cutoff}} \approx 1.3$ GHz.

Above the cut-off wavelength, equation (2.71) is not really applicable for the loss anymore, since it is arrived assuming that the penetration of the fields into the conductor is very shallow. In the “Bothnian” case, the penetration depth at cut-off is in fact comparable to the width of the dielectric in the guide, and this assumption breaks down. In addition, the conductor (i.e. sea

water) has much higher permittivity than the rest of the guide, increasing the overlap with the conductor even further. Finding the actual loss requires more detailed analysis than is attempted in this project, but we can adapt expression (2.71) to find the lower limit for the loss, and hence the upper usable frequency limit:

$$\frac{1}{\delta_{\text{guide,SW}}} = \alpha_{\text{guide,SW}} \geq \frac{c^2}{4a_{\text{guide,SW}}^3} \sqrt{\frac{\pi\epsilon_0}{\sigma f^3 \left[1 - \left(\frac{c}{a_{\text{guide,SW}} f} \right)^2 \right]}} \quad (2.76)$$

The factor of 4 in the denominator compared with the factor 2 in (2.71) arose since the loss in the sea-water guide is completely dominated by the resistivity of the sea water. Maximum $\delta_{\text{guide,SW}}$ according to equation (2.76) is indicated in Figure 2.38 with dashed line. Apparently, the loss above the cut-off decreases very rapidly, so the sensors will not be usable above the cut-off frequency. In order to operate in the Baltic, the RF frequency should thus be selected between roughly 1 and 200 MHz. If the system is not required to work in the Baltic Sea and similar areas with very low salinity, the allowable frequency range according to Figure 2.38 is much wider, perhaps between 100 kHz and 1 GHz. If t , the distance between the sea and the conductive screen, is wider, the upper limit may be reduced somewhat.

2.4.1.2 Antenna and Radio Transmitter Selection

Above water, the conducting shield will act as a radio reflector. Assuming that the shield is a good conductor, there cannot be any tangential electrical field. I.e., reflectivity coefficient of the tangential electrical field is negative, and the tangential electric field close to the shield will be quite small. On the other hand, the reflection coefficient of the tangential is positive, and tangential magnetic field will have a local maximum at the conductor shield surface. Thus, an ordinary whip or dipole antenna oriented parallel to the shell plates will not be very effective since they are insensitive to magnetic fields. Since the wavelength of the frequencies in the “Baltic” range is 1.5 m or more, a dipole or whip antenna normal to the shell plates will either not be very sensitive (short antenna) or very practical (antenna length comparable to half the wavelength). An alternative is to use a magnetic loop antenna, with the loop axis being parallel to the hull surface and orthogonal to the propagation direction of the radio waves. Such an antenna would of course work best if the transmitted radio signal also has the magnetic field parallel to the shell plates.

Antenna Figure of Merits

Apart from the physical footprint, the performance of an antenna is usually characterized by its radiation resistance and its radiation efficiency factor. The radiation resistance R_r is a measure of how much power is emitted from an antenna for a given current:

$$P_r = R_r i_{\text{rms,S}}^2 \quad (2.77)$$

Here P_r is the radiated power, R_r is the radiation resistance and $i_{\text{rms,S}}$ is the root mean square (RMS) current of the antenna. Note that R_r is a fictitious resistance. Due to the reciprocity of antennas, the radiation resistance also gives the RMS voltage of the (open-circuit) antenna from incoming radiation:

$$v_{\text{rms},S}^2 = R_r P_r \quad (2.78)$$

All directivity of the antenna is here hidden in P_r . Later amplification stages will always add some noise, and a high signal strength for a given radio signal is therefore almost always desirable. I.e., we want R_r to be as large as possible. The final signal to noise ratio can however never be better than that coming from the antenna itself. The primary noise source from an open-circuited antenna, is thermal noise from internal resistance, given by [7;8]:

$$v_{\text{rms},N,f} = \sqrt{4k_b T R_l B} \quad (2.79)$$

k_b is Boltzmann's constant, T is the absolute temperature and R_l is the loss resistance of the antenna, i.e. resistance that is not related to radiation, and B is the bandwidth of the detection system. In addition there will be noise contributions from atmospheric and man-made electromagnetic noise sources.

$$v_{\text{rms},N,a} = \sqrt{R_r P_{r,N}} = \sqrt{4k_b T_r R_r} \quad (2.80)$$

Here T_r is called the equivalent ambient noise temperature. Note that this noise does not originate from the antenna itself, but from black body radiation or radiation from other man made or natural sources. R_r is only a virtual resistance, and is in itself noiseless, a fact that unfortunately is lost by many authors. Typical noise temperatures are plotted in Figure 2.40. Possible sources from the ship itself are not included. At 1 MHz, we have that T_r is larger than the real temperature T by a factor of 10^7 at night, whereas T_r comparable to the real temperature at 200 MHz.

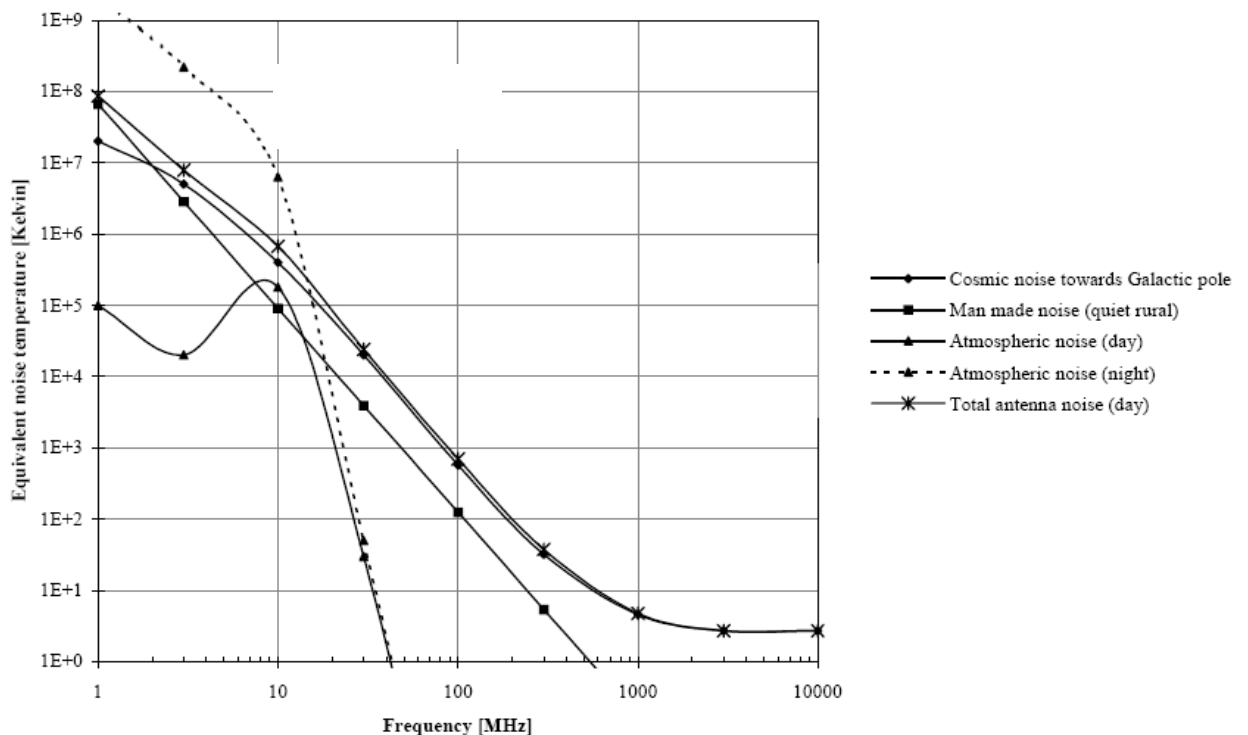


Figure 2.40 Typical noise temperatures T_r , adapted from [9]

The noise factor F of the antenna is the ratio between the signal to noise ratio of the incoming radiation compared with the signal to noise ratio at the output ports of the antenna:

$$F = \frac{\left(\frac{S}{N}\right)_{\text{in}}}{\left(\frac{S}{N}\right)_{\text{out}}} = \frac{\frac{P_r}{4k_b T_r B}}{\frac{P_r R_r}{4k_b T_r B + 4k_b T_r R_r B}} = 1 + \frac{TR_l}{T_r R_r} \quad (2.81)$$

Note that depending on the ambient noise and radiation resistance, an antenna can have a noise factor lower than 2!

Magnetic Air Core Antennas

Due to space constraints, a magnetic antenna should probably be of the solenoid type. The radiation resistance of a long solenoid antenna is given by:

$$R_{r,\text{sol}} = \frac{8}{3} \eta \pi^3 \left(\frac{NA}{\lambda^2}\right)^2 \approx 31200 \times \left(\frac{NA}{\lambda^2}\right)^2 \Omega, \quad (2.82)$$

where η is the vacuum impedance given by:

$$\eta = \sqrt{\frac{\mu_0}{\epsilon_0}} \approx 377 \Omega. \quad (2.83)$$

N is the number of turns, A is the cross sectional area of the coil, and λ is the wavelength. There can be different types of losses in a solenoid antenna. For an air-core solenoid, the major loss will come from resistive losses of the wire. The loss will increase with higher frequencies due to skin effect, which forces the current to run at the conductor surface. Due to this current concentration at the conductor surface, current will also be induced at the surface of neighboring wires, increasing the resistance further. The latter phenomenon is called the proximity effect. The resistive loss can only be calculated accurately using numerical methods, but approximate analytical expressions exist. The most popular among these is probably the Dowell method [10], but it turns out to be quite inaccurate both at high frequencies and for widely spaced windings. A quite accurate, but rather complex model has been developed by Nan and Sullivan [11;12]. We will use the high-frequency limit of the simpler model developed by Fraga et. al, which seems quite accurate for single layer and tightly wound coils [13]. For loosely wound coils, i.e. coils where there is some distance between each turn, the resistivity is decreased inversely proportional to the square root of the filling factor, similar to what is done in [10], but only until the resistance equals that due to the skin effect of a solitary conductor. The resulting, approximate expressions for the wire resistivity become:

$$R_{l,w,s} \approx \begin{cases} \frac{NG_{\text{coil}}}{\pi r_w \delta_M \sigma_M} \max \left[\frac{\sqrt{l^2 + (NG_{\text{coil}})^2}}{NG_{\text{coil}}}; 2 \sqrt{\frac{2\pi r_w}{p_w}} \right], & r_w \gg \delta_M, \text{ arbitrary cross section} \\ \frac{ND_{\text{coil}}}{r_w \delta_M \sigma_M} \max \left[\frac{\sqrt{l^2 + (\pi ND_{\text{coil}})^2}}{\pi ND_{\text{coil}}}; 2 \sqrt{\frac{2\pi r_w}{p_w}} \right], & r_w \gg \delta_M, \text{ circular cross section} \end{cases} \quad (2.84)$$

As before, r_w is the wire radius, σ_M is the metal conductivity, and l is the antenna length (outer dimension of coil). G_{coil} is the coil circumference and D_{coil} is the coil diameter in case of a circularly shaped coil. p_w is the distance between the centers of the wires of each turn. δ_M is the skin depth of the wire, analogous to the penetration depth of sea water from equation (2.68):

$$\delta_M = \frac{1}{\sqrt{\pi\mu_0\sigma_M f}} \quad (2.85)$$

At 1 MHz using copper wire, δ_M is 66 microns, so the assumption $r_w \gg \delta_M$ is reasonable in our preferred frequency range between 1 and 200 MHz. Note that for a solitary wire, the resistance is equal to the length of the conductor divided by the conductance of the fiber and the area of a ring along the circumference of the wire of width δ_M . For tightly wound wires, this resistance is increased further by a factor $2\sqrt{\pi}$ due to the proximity effect. With multiple wound layers, the proximity effect will increase the resistance greatly [13].

It is possible to reduce both the proximity and skin effect somewhat by using so-called Litz wire. This is a stranded wire where each strand is insulated from the other ones, so that the current is forced to run in the interior of the wire. Using such a wire, it seems possible to reduce the resistance at least 50 % [14]. However, at higher frequencies, the skin effect in each strand and the proximity effect between the strands in fact increases the resistance compared with a solid wire. A thorough analysis of Litz wire optimization is given in [15]. A rule of thumb, however, is that Litz wire cease to be more effective than solid wire when the strand diameter becomes equal to the penetration size. The thinnest strand that seems to be easily available commercially is AWG48, corresponding to a strand radius of around 16 micron. In comparison, the skin depth becomes 16 micron around 18 MHz. According to [14], the lowest possible loss is achieved at about half the cross over-frequency, i.e. at 9 MHz. Other sources indicate that Litz does not improve the loss above 3 or even 1 MHz, however, but this may be due to lack of availability of the thinnest wires.

From equations (2.81)-(2.82) and (2.84) the noise factor of a magnetic antenna will decrease at least inversely proportionally with N . N cannot be increased without limit, however. One reason is of course there are constraints regarding how long the antenna can be. A more fundamental limit is caused by the increasing inductance of the antenna L_{sol} , given by (2.26). Since we always have some parasitic capacitance, this will in practice limit the bandwidth for a given value of N . The parasitic capacitance of the input ports of the amplifier circuit is of course very dependent on the design, but will typically be around 20-30 pF [16]. In addition, there will be distributed capacitance in the coil itself, approximately given by [17]:

$$C_{p,\text{sol}} = \frac{\pi G_{\text{coil}} \epsilon_0}{(N-1) \ln \left[\frac{p}{2r_w} + \sqrt{\left(\frac{p}{2r_w}\right)^2 - 1} \right]}, \quad N > 1 \quad (2.86)$$

Here p is the distance between the centers of neighboring wires, and it is assumed that the thickness of the insulating coating is thin compared with r_w . Hence, even without mounting a capacitor, the antenna circuit will be equivalent to an RLC-circuit as sketched in Figure 2.41.

The resonant frequency of this circuit is given by:

$$f_0 = \frac{1}{2\pi\sqrt{L_{\text{sol}}C}} = \frac{1}{2\pi\sqrt{L_{\text{sol}}(C_{p,\text{circ}} + C_{p,\text{sol}})}} \quad (2.87)$$

Here $C_{p,circ}$ is the parasitic capacitance at the input port of the amplifier that is not caused by the antenna. f_0 is roughly independent of N when $C_{p,isol}$ is dominating, but proportional to $1/\sqrt{N}$ when $C_{p,circ}$ is dominating. Signals as well as noise at the resonant frequency are amplified by the so-called quality-factor Q of the oscillation circuit, given by:

$$Q = \frac{2\pi f_0 L_{isol}}{R_l + R_r} \quad (2.88)$$

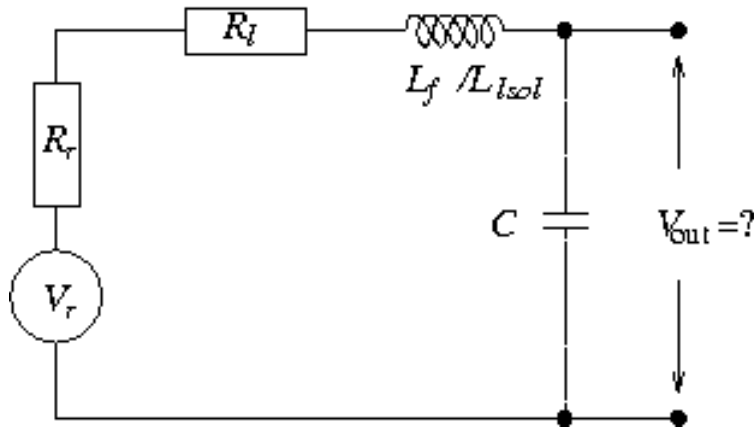


Figure 2.41 Equivalent circuit of a magnetic loop antenna tuned resonant circuit.

Above the resonant frequency, however, the signal will decrease inversely proportional to the frequency. Thus, the operation frequency should be at the resonant frequency in order to get optimum noise performance. It can be shown that:

$$Q = \frac{\Delta f}{f_0} \quad (2.89)$$

, where Δf is the bandwidth of the resonance. Hence, if the signal is within a bandwidth of Δf around f_0 , the resonant circuit can filter out broadband noise. In some cases, such filtering can also be performed later in the amplification chain, however.

The impact of equations (2.81)-(2.88) on an air-core magnetic antenna is best illustrated through specific examples. Let us assume that $C_{p,circ} = 25$ pF and that we have a coil with circular cross section with $D_{coil} = 1$ cm and another coil with rectangular cross section with thickness and height equal to 6 cm and 20 cm, respectively, which results in $G_{coil} = 52$ cm. The rectangular coil builds 6 cm into the interior of the ship (or alternatively into the shell plate), and such a coil should probably not have any larger height than 20 cm in order to achieve the desirable sensor resolution in relative wave height. Assuming a packing factor $p/2r_w = 1.2$, we get from (2.86) that $C_{p,isol}(N-1) \approx 1.4$ pF for the small circular coil and 23 pF for the largest coil. Compared with $C_{p,circ}$ we can thus neglect the distributed capacitance of the coils since we need to have $N \gg 1$ in order for our other assumptions here to be correct. Further assuming a solenoid length of $l=30$ cm, we find by inserting (2.26) into (2.87) that in order to be at the resonance frequency, the number of turns in the winding should be:

$$N_{\text{req}}(f_0) = \begin{cases} \frac{1}{2\pi f_0} \sqrt{\frac{l}{\mu_0 A_{\text{coil}} C_{p,\text{circ}}}}, & \text{arbitrary cross section} \\ \frac{1}{f_0 D_{\text{coil}}} \sqrt{\frac{l}{\pi^3 \mu_0 C_{p,\text{circ}}}}, & \text{circular cross section} \end{cases} \quad (2.90)$$

N_{req} is plotted as a function of the resonance frequency in Figure 2.42 for coils with circular cross sections and with D_{coil} equal to 1 cm, 2.5 cm and 6 cm as well as for two rectangular cross sections with dimensions $1 \times 10 \text{ cm}^2$ and $6 \times 20 \text{ cm}^2$. A coil thickness of 1 cm can be made without changing the effective distance to the sea significantly. Also an antenna of thickness 6 cm can be incorporated into the shell plates and as such will not alter the distance between the conductive screen and the sea water t_{shield} used in the calculations of 2.4.1.1. If the antenna is placed on the inside of the hull, t_{shield} has to be increased roughly by a factor of two, but because of the deep penetration depth into sea water in the “Baltic Winter” case, this will not significantly change the upper limit of the frequency range of the sensor system. Of course, the curves of Figure 2.42 are only approximate at the highest frequencies, as the expression (2.26) for the inductance is not valid for a coil with only a few turns.

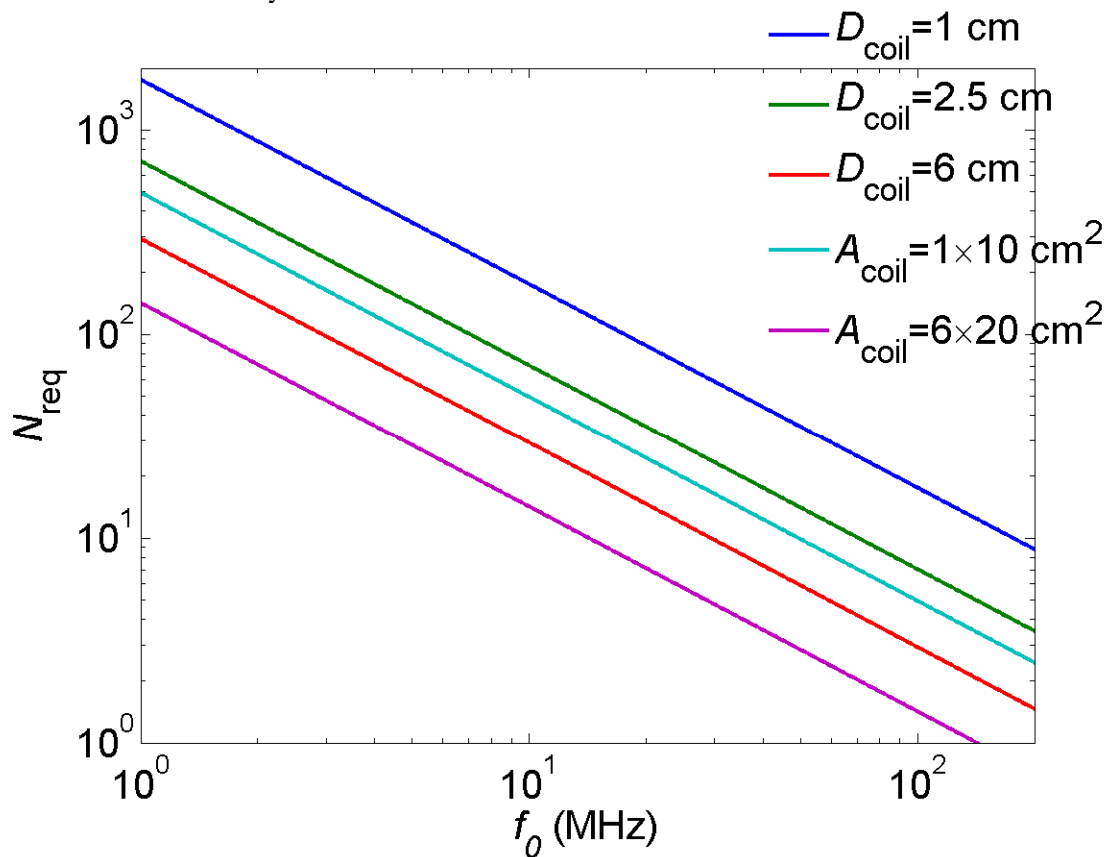


Figure 2.42 Required number of turns of an air-core antenna of length 30 cm with a parallel capacitance of 25 pF as a function of resonant frequency for different coil cross sections

In order to reduce the resistance loss, we should use a wire that is maximally wide and where the single layer coil still fit the bobbin. In practice, there will however also be an upper limit on the wire radius, and here we require that r_w is less or equal to 15 % of the coil thickness (i.e.

diameter for a circular coil). The resulting radiation and loss resistance is given in Figure 2.43. Since the required number of turns from equation (2.90) is inversely proportional to the square root of the area $\sqrt{A_{\text{coil}}}$ and the resonance frequency f_0 , the radiation resistance will from (2.82) increase proportionally to both f_0^2 and A_{coil} , but in our frequency band of interest and considered structures it is mostly lower than the loss resistance except at high frequencies. The loss resistance, as defined in (2.84), has a more complicated dependence on the coil parameters.

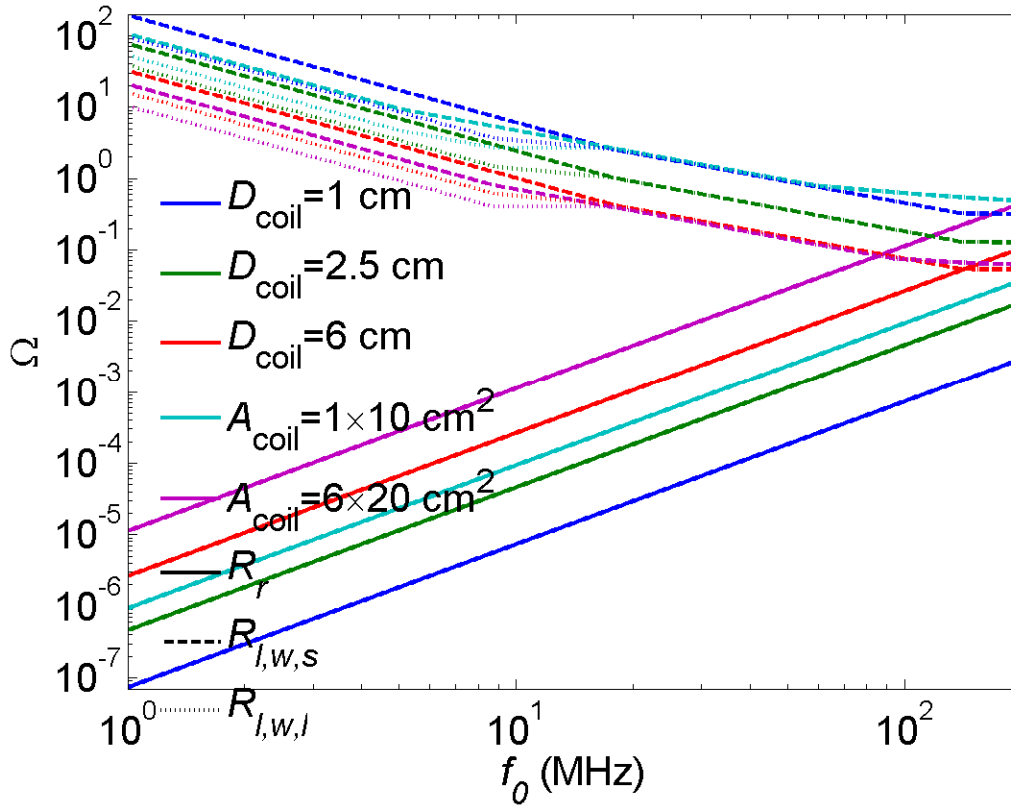


Figure 2.43 Radiation R_r and loss R_l resistance under the same conditions as in Figure 2.42 and with the conditions for wire radius and possible use of Litz wire given in the main text.

For coils with circular frequencies it can be shown that $R_{l,w,s} \propto D_{\text{coil}}^{-1}$ for all frequencies. Below 17 MHz, $p_w = 2r_w \propto N^{-1}$ and it can be shown that $R_{l,w,s} \propto f_0^{-3/2}$. Above 17 MHz but below ~140 MHz, r_w is constant while we still have $p_w \propto N^{-1}$, and hence $R_{l,w,s} \propto f_0^{-1}$. Above ~140 MHz proximity losses are ignored, and $R_{l,w,s}$ is given by the length of the wire times the square root of the frequency. For coils with rectangular cross sections, the tendencies are the same, both with regard to the dependence on the frequency and coil dimensions, but with some adjustments dependent on the ratio between the thickness and the width.

In Figure 2.43 we have plotted an estimate for an optimum loss resistance using Litz wire as well. As discussed above, it is not expected that Litz wire will make a positive effect above 18 MHz, and with full noise reduction of around 50 % only at 9 MHz and below. Hence, we have assumed

that we use solid wire above 18 MHz, and optimized Litz wire below 18 MHz, with a reduction in the Litz optimized wire loss resistance $R_{l,w,l}$ increasing linearly from 50 % to 100 % of the solid wire resistance $R_{l,w,s}$ from 9 to 18 MHz. For the higher frequencies, this probably represents a rather optimistically low loss.

Although the loss resistance in most of the region is much higher than the radiation resistance at the lower frequencies, that does not necessarily mean that the highest frequencies give optimum performance. From Figure 2.40 we see that also the external noise temperature is T_r is much higher at lower frequencies, contributing to decrease of the noise factor F defined in (2.81). In addition, the Q-factor defined in (2.88) has a complex dependence on the inductance and resistance values.

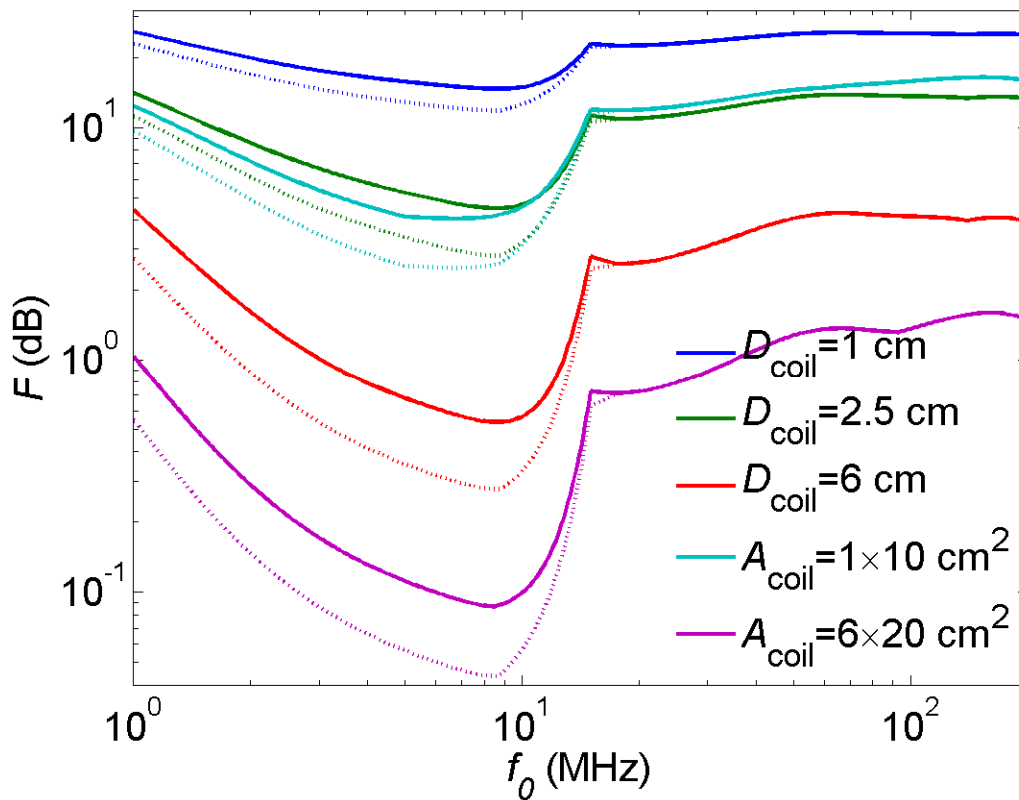


Figure 2.44 Noise figure F of magnetic air-core antennas plotted under the same conditions as Figure 2.42 and Figure 2.43. Results using solid and Litz wire are plotted with solid and dotted curves, respectively.

In Figure 2.44, the noise figure F is plotted for the air-core magnetic antenna with and without the use of Litz wire. In order to calculate F , approximate values for T_r taken from Figure 2.40 and reference [9] have been used. If external noise is the dominating noise source, it seems like the optimum frequency for antennas with circular cross section with the lowest noise figure for this type of antenna is around 8.6 MHz. Further, the area of the antenna is very important since $R_{l,w}/R_r \propto D_{\text{coil}}^{-3}$ for an antenna with circular cross section. At $f_0 \approx 8.6$ MHz and $D_{\text{coil}} = 1$ cm, we have a noise factor of around 29 for a solid wire and 15 using the rather optimistic Litz loss

function, both being unnecessarily high. By increasing the coil diameter D_{coil} to 2.5 cm, the noise factor is already reduced to the more acceptable $F \approx 2.8$ for solid wire and $F \approx 1.9$ for the Litz case. With $D_{\text{coil}} = 6$ cm, the antenna is practically noiseless, with $F \approx 1.13$ for the solid wire. A 3 dB (≈ 2) noise factor is achieved with $D_{\text{coil}} \approx 3.1$ cm for the solid wire and $D_{\text{coil}} \approx 2.4$ cm using Litz wire. It is also worth noting that with $D_{\text{coil}} = 6$ cm, F is below 3 for all frequencies between 1 and 200 MHz. The rectangular shape the optimum frequency is somewhat lower, and lower the bigger difference between the width and thickness of the coil is. Note that the 1×10 cm² coil has only marginally lower optimum F than the circular coil with $D_{\text{coil}} \approx 2.5$ cm, even if the latter has only half the area. This is of course because the longer circumference as a function of cross section area of the rectangular coils. The lowest value of the noise factor, $F=1.02$ is predictably achieved for the 6×20 cm² coil. With this coil, F is smaller than roughly 1.4 over the entire frequency range 1-200 MHz. Remember, however, that the model is probably not very accurate above ~ 20 MHz due to the low number of turns.

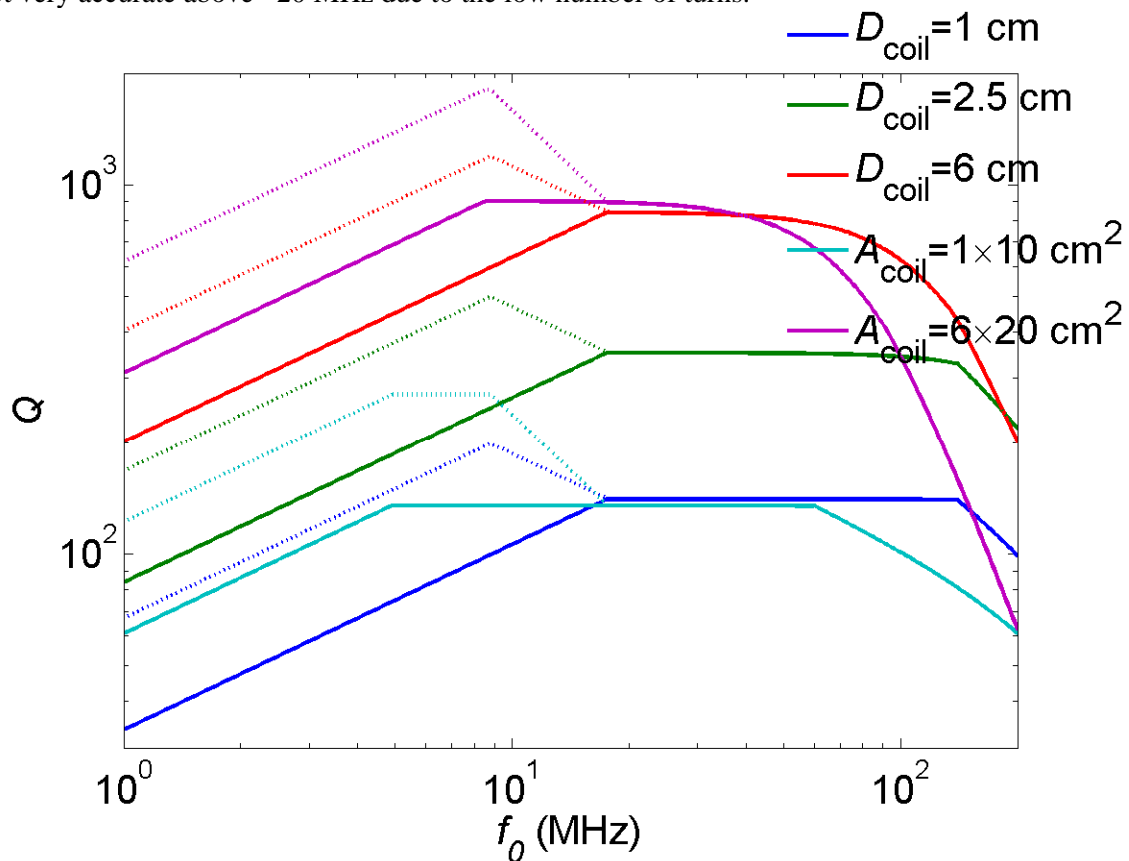


Figure 2.45 Resonance quality factor Q of magnetic air-core antennas plotted under the same conditions as Figure 2.42 and Figure 2.43. Curve definitions as in Figure 2.44.

In Figure 2.45, the Q-factor is plotted as a function of resonance frequency. Since we have assumed constant capacitance and hence inductance, Q is only dependent on the ratio between the frequency and the radiation and loss resistance of the antenna. Using solid wires, the Q is highest and fairly constant between 17 and 80 MHz. The rectangular antennas have an optimum frequency that is somewhat lower, and due to the higher wire loss, Q is lower than a circular

antenna with the same cross section area. Using Litz-wire, all the considered antennas have a peak in Q below 10 MHz.

As discussed above, a high Q can enhance the signal to noise ratio if the signal has a narrower bandwidth than $\Delta f = f_0/Q$, but will otherwise not affect the signal to noise ratio. Similarly, the signal strength from the resonant circuit will also be proportional to QR_r for a narrow band signal. Hence, we have plotted QR_r as a function of f_0 in Figure 2.46. The QR_r product is mostly an increasing function of f_0 . Hence, even the frequency with the lowest antenna induced noise is at $f_0 = 8.6$ MHz or lower, the optimum resonant frequency is higher than this if the noise induced in the amplification process is dominating. Note however, that once the bandwidth of the signal becomes larger than $\Delta f = f_0/Q$, higher Q no longer gives higher signal strength.

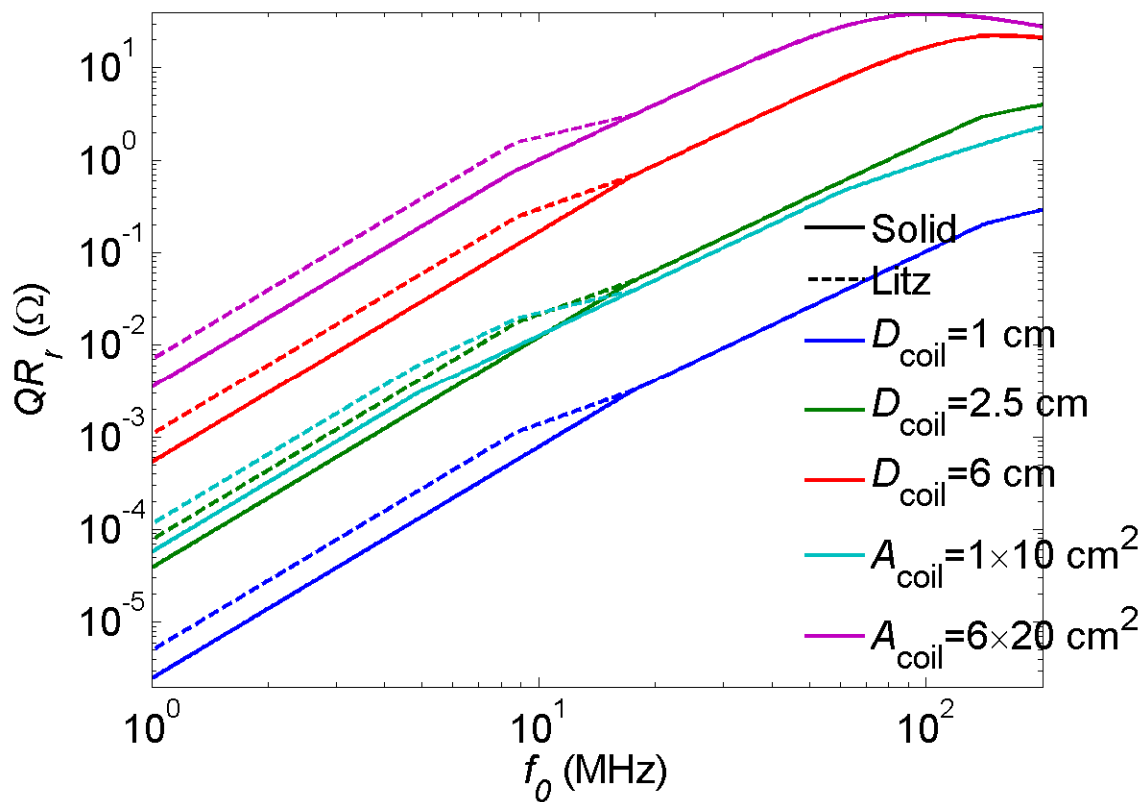


Figure 2.46 QR_r -product of magnetic air-core antennas plotted under the same conditions as Figure 2.42 and Figure 2.43

Magnetic ferrite rod antennas

A popular technique for increasing the radiation resistance of magnetic coil antennas is to place a material with high relative permeability inside the coil, as illustrated in Figure 2.47. The reason is that the radiation resistance from equation (2.82) is proportional to the relative permeability squared. The most common class of materials to use is ferrites, which are ceramic materials with iron oxides as one of the main components. Ferrite materials come with relative permeability values from around 20 to 2000. Unfortunately, the increase in permeability comes at the cost of increase loss, a loss which increases with frequency. This increase in loss is roughly

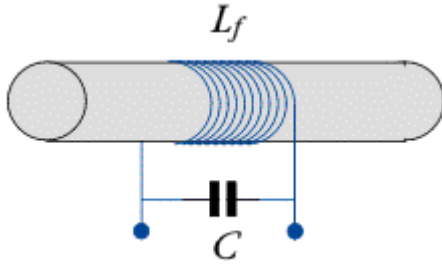


Figure 2.47 Illustration of a tuned loopstick/ferrite core antenna.

speaking caused by the work required to flip the magnetic domains in the ferrite material as the sign of the magnetic field changes. This loss is increasing with frequency and permeability of the material, and in practice this limits the useful permeability range to be used in our case to $\mu_r = 125$ and less. With increased permeability also the inductance will increase, which will limit the number of windings and hence radiation resistance. However, the net effect will still be an increase in radiation resistance.

There is generally no analytical expression for the radiation resistance, inductance and loss of a ferrite core antenna. With the invention of ferrite core antennas now being several decades ago, and their importance seemingly in decline since the switch from AM to FM radios, the information about optimization of ferrite core antennas now seems to be more in the domain of engineers and radio amateurs publications than refereed scientific publications [18-22] It is convenient to define the ferrite antenna radiation resistance and inductance the following way:

$$R_{r,f} = \frac{8}{3} \eta \pi^3 \left(\frac{\mu_{rod} N A}{\lambda^2} \right)^2 \quad (2.91)$$

$$L_f = \frac{\mu_{coil} \mu_0 N^2 A}{l_{rod}}. \quad (2.92)$$

Here we have defined a new set of parameters, the rod permeability, μ_{rod} , and the coil permeability μ_{coil} . Both these parameters are typically significantly less than the material relative permeability μ_i except for very long and thin rods. l_{rod} is the length of the ferrite rod.

μ_{rod} is mostly a function of μ_i and the rod length to the rod diameter ration, whereas the dependence on the length and location of the coil on the rod [18;23] is relatively weak. A plot of μ_{rod} as a function of the length to diameter ratio of the rod is given in Figure 2.48 for different values of μ_i . From the figure, it is evident that the length to diameter ratio of the road is more important than μ_i for relatively thick rods, especially considering that μ_i has large temperature dependence. Typically, commercially rods available in stock, for instance from Amidon[24], have a length to diameter ratio between 8 and 16, but rods with higher as well as smaller ratios may be custom ordered.

μ_{coil} is typically smaller than μ_{rod} , and as mentioned above, is dependent on the placement and length of the coil versus the rod. Reference [24] states that for a centered coil, $\mu_{coil} \propto \sqrt[3]{l_{rod}/l_{coil}}$,

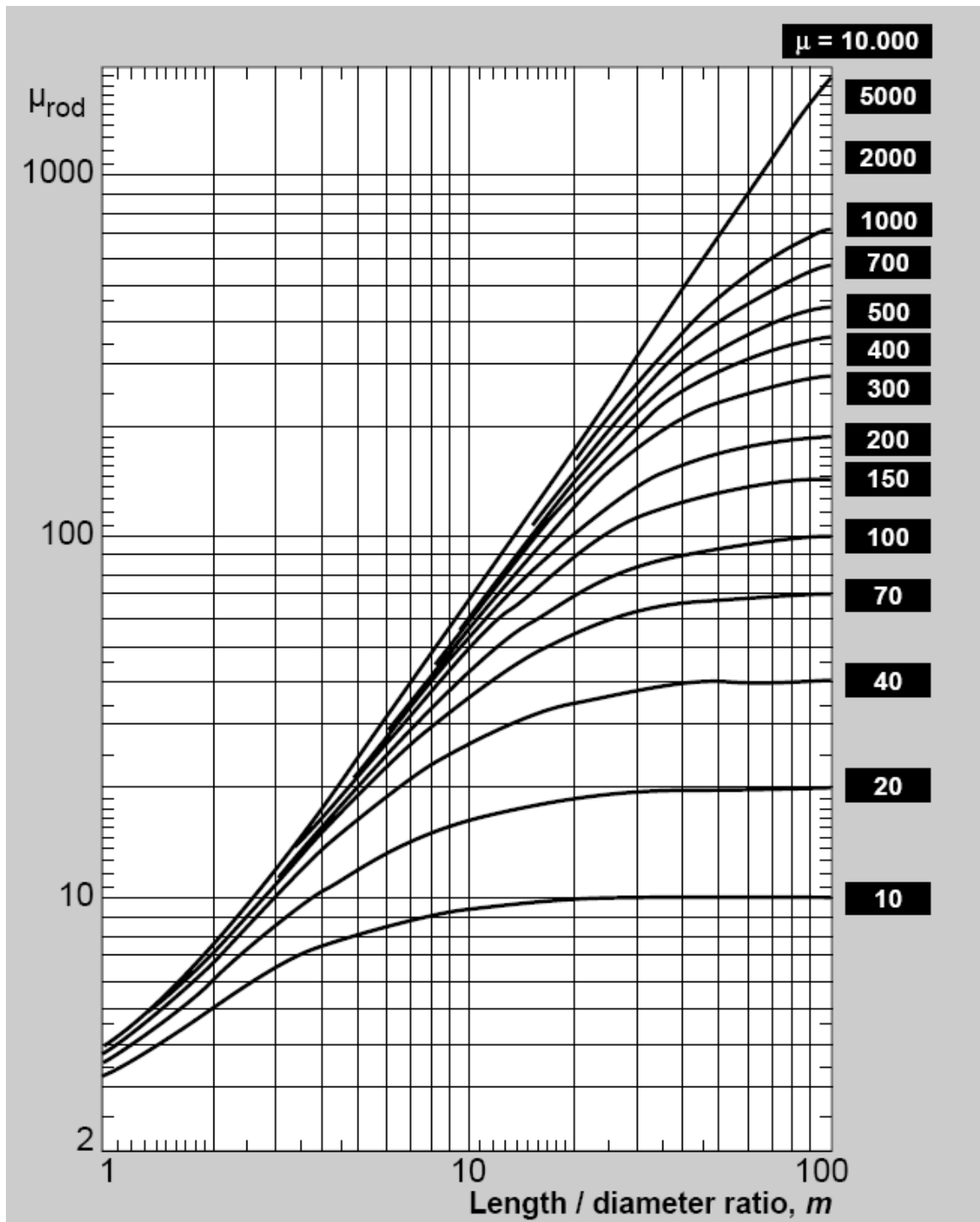


Figure 2.48 Rod permeability μ_{rod} as a function of ratio between rod length and diameter for different values of the relative ferrite material permeability μ_i . From [23;24].

but both experimental and simulation results indicate that this is not a very accurate approximation [18;20;21]. Both for simplicity, and because it probably gives the best performance of the antenna, we will in the following assume that the length of the coil equals the length of the rod, i.e. $l_{rod} \approx l_{coil}$. As the permeability of ferrite rods also varies greatly with temperature, and from batch to batch, magnetization history etc, we will also assume that $\mu_{coil} \approx \mu_{rod}$, although this is only completely true for long rods.

The additional resistivity induced by the ferrite material is approximately given by:

$$R_{l,f} = 2\pi fL_{\text{frod}} \frac{\mu''}{\mu'} = 2\pi fL_{\text{frod}} \tan \Delta \quad (2.93)$$

μ'' and μ' are the imaginary and real permeability, respectively, whereas $\tan \Delta$ is called the loss tangent of the material. Both μ'' and μ' and hence $\tan \Delta$ are frequency dependent material parameters, and as discussed above, the increase of μ'' at higher frequencies limits the efficiency at higher frequencies. A popular material with relatively low $\mu_r = 125$ is the so-called ferrite #61 marketed for instance by Amidon [24] and Fair-Rite [25]. Plots of the complex permeability of ferrite material #61, as well as the so-called material #67 with $\mu_r = 40$ and material #68 with $\mu_r = 20$ are given in Figure 2.49 - Figure 2.51. These plots are taken from the Fair-Rite product catalog [25]. It should be noted that the characteristic frequency where the complex permeability starts to rise increases with decreasing μ_r . Unfortunately, material #67 and especially material #68 are typically not stocked as well as material #61. Other producers with a wide range of ferrite rods available are MMG, where, in order of ideal operation frequency interval, materials F25, F28, F29, FXQ, and F31 are suitable [26], and Ferroxcube [27].

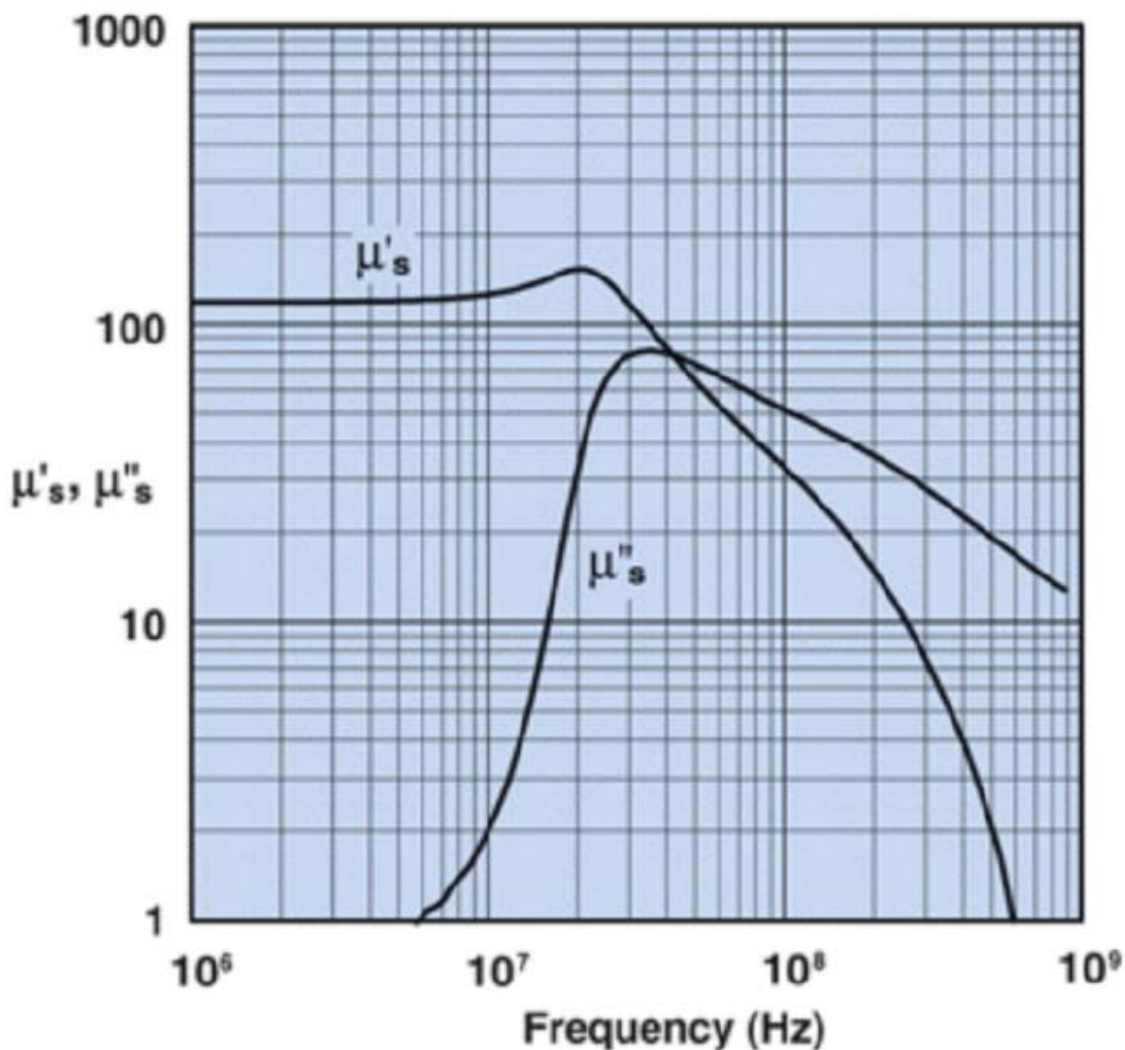


Figure 2.49 Complex permeability for ferrite material #61 [25]

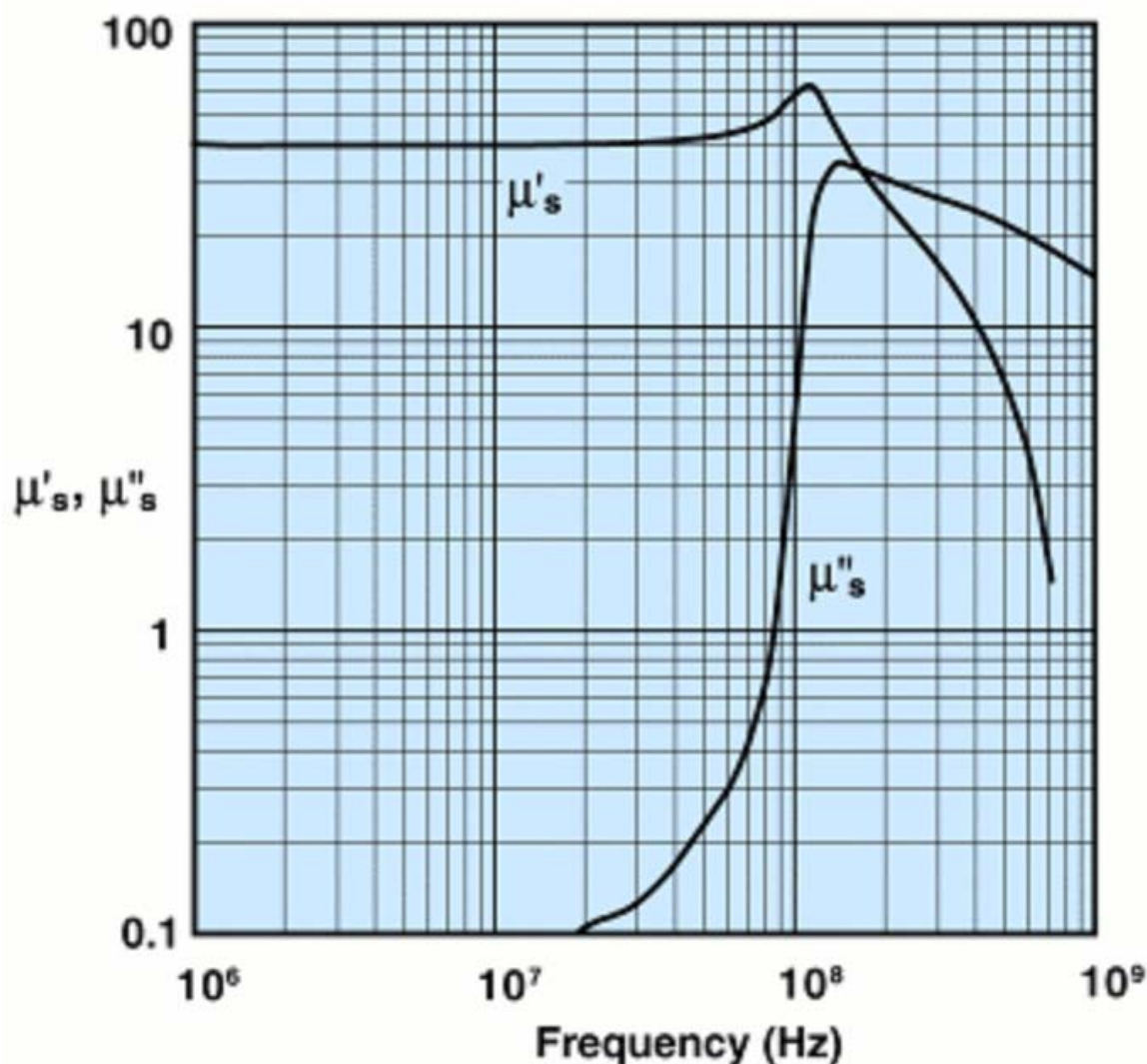


Figure 2.50 Complex permeability for ferrite material #67 [25]

A similar calculation of antenna performance has been done for antennas with ferrite rod core antennas as the magnetic air-core antennas. The results are summarized in Figure 2.52 - Figure 2.61. In Figure 2.52 - Figure 2.56 the various antenna parameters are plotted for different antennas constructed using material #61 from Fair-Rite/Amidon [24;25], as this is a material that seems to be widely available. The selected rod sizes are as specified in the Amidon catalog [24] (hence the use of inches), except size 1"x12.3", which is available as a plastic covered rod from www.stormwise.com [28]. Since all rods do have a limited cross section compared with the area of the biggest air core magnetic antenna discussed above, we have also considered an antenna with a core consisting of a bundle of 2x8 1"x12.3" antennas. This antenna will have a total cross section of $5.1 \times 20.3 \text{ cm}^2$, with holes, but with a total cross section similar to the biggest air core antenna. The effective ferrite cross section area to be used in formulas above is $A = 16\pi(0.5")^2 = 81 \text{ cm}^2$. No reference has been found that gives the rod permeability of such a bundle of rods nor a slab/plate of ferrite, but for simplicity, we find the value from Figure 2.48 assuming that we have a circular rod with a radius/length ratio of roughly 3. This is probably a conservative (i.e. low) estimate.

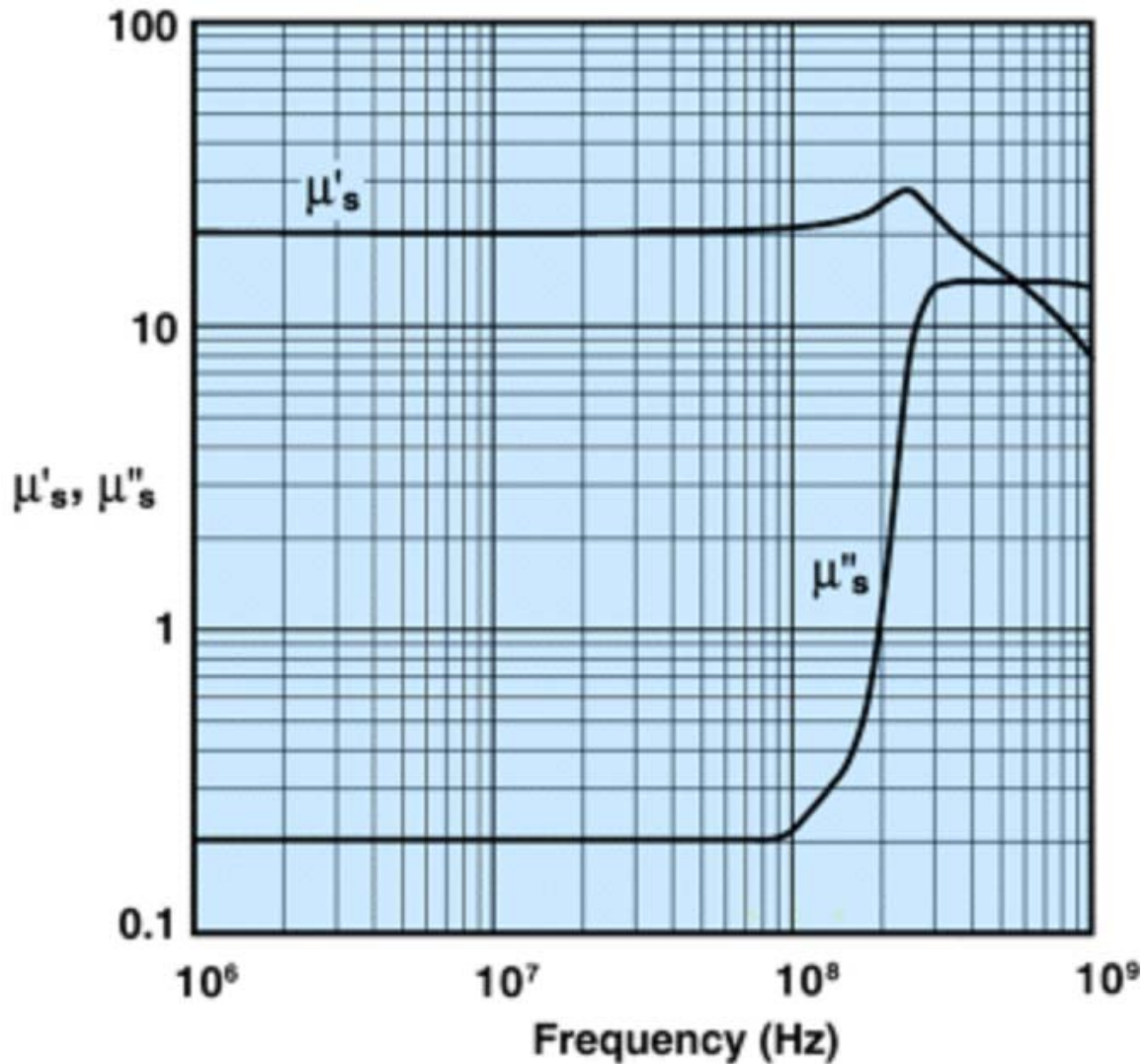


Figure 2.51 Complex permeability for ferrite material #68 [25]

In Figure 2.52, the required number of turns for the various material #61 ferrite antennas is given. Considering the high rod permeability, it comes as no surprise that the required number of turns is significantly less than for air core antennas of similar dimensions. It is of course meaningless to speak of a solenoid antenna with ~ 1 turns or less, and hence except the thinnest rod, it will not be possible to make an antenna with a material #61 core rod for frequencies above roughly 100 MHz.

In Figure 2.53 the considered loss resistance contributions and radiation resistance is plotted as a function of frequency. Compared with the resistance values for the air core antennas plotted in Figure 2.43, the radiation resistance values as expected is much higher, but the wire loss resistance is in fact a bit lower, because fewer turns are required. However, the wire loss resistance is dwarfed by the loss from the ferrite, $R_{l,f}$, particularly above 10-20 MHz, where this loss becomes several decades higher than the wire loss. Below 10 MHz, the total loss of the ferrite core antennas is similar or lower than corresponding air-core antennas.

In Figure 2.54, the resulting noise figure F is plotted. The optimum frequency is for all the ferrite

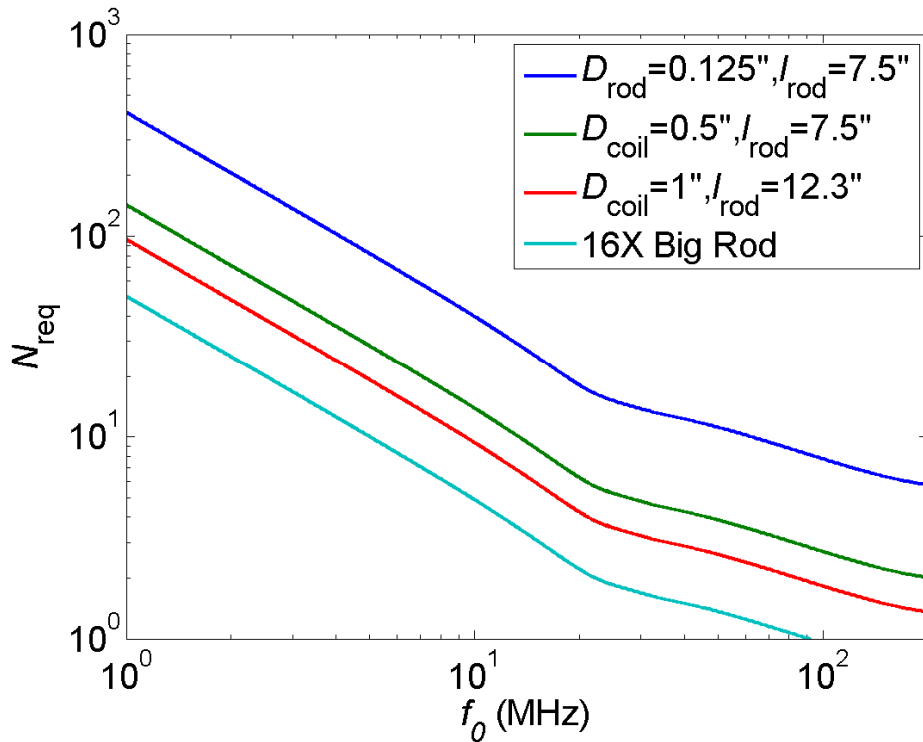


Figure 2.52 Required number of turns, i.e. as Figure 2.42, but for various ferrite material #61 core alternatives. The last antenna is a bundle of 2x8 "big rods" of dimension $D_{\text{coil}} = 1''$, $l_{\text{rod}} = 12.3''$. Details are given in the main text.

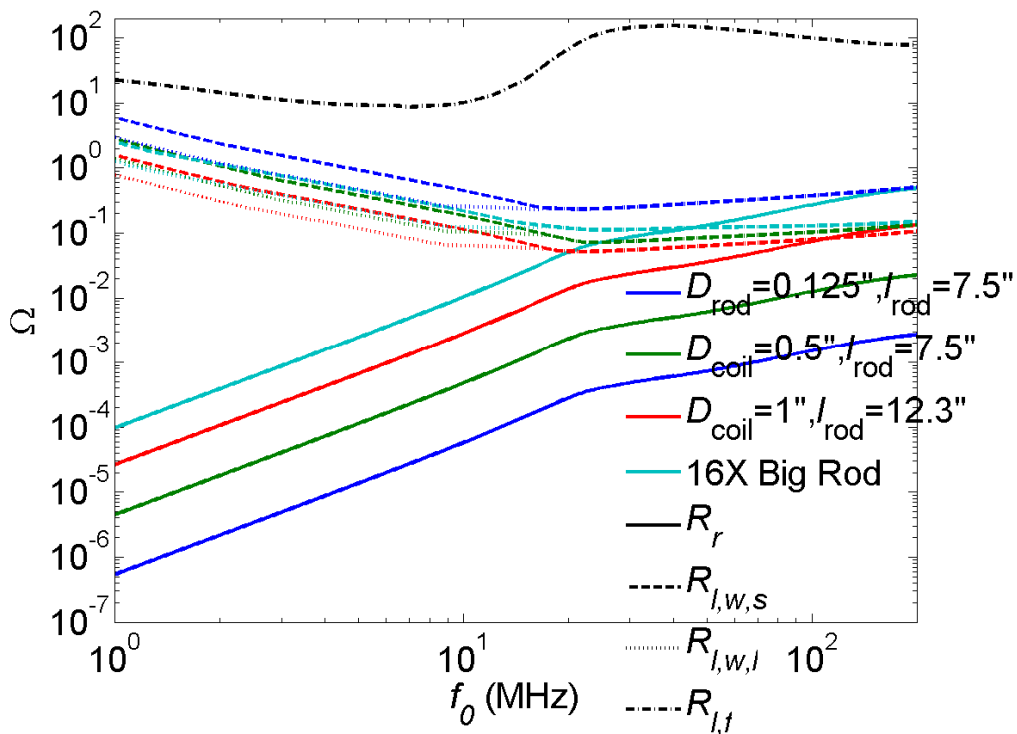


Figure 2.53 Similar to Figure 2.43, i.e. loss resistance contributions and radiation resistance as a function of operation frequency, but for various ferrite core material #61 antennas as in Figure 2.52.

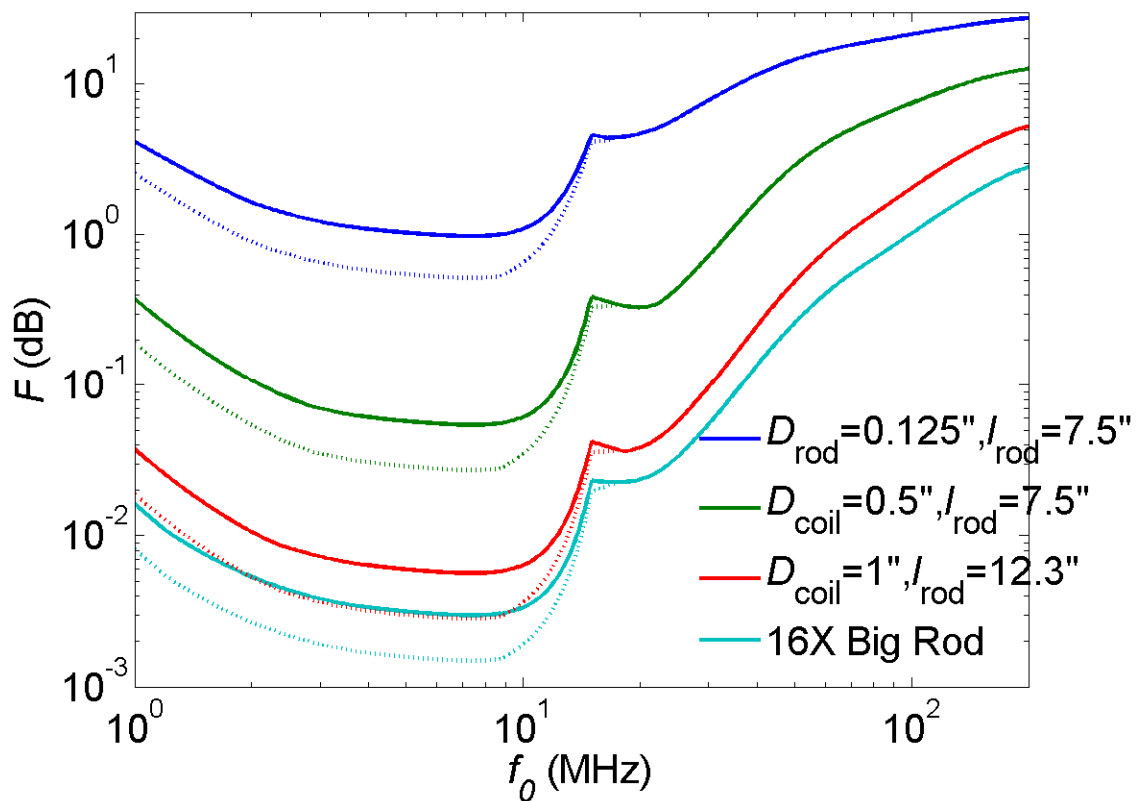


Figure 2.54 Similar to Figure 2.44, but for the same ferrite core antennas as in Figure 2.52.

material #61 antennas around 7.3 MHz, i.e. slightly lower than the air core antennas. The noise figure is typically lower than for the air-core antennas of similar dimensions, but the noise figure curves are characterized by an increase of the noise figure above 20 MHz that is caused by the ferrite loss and hence is not found for the air-coil antennas. Still, for the “big rod”, 1”x12.3”, the noise figure is only $F \approx 2$ at 100 MHz. The noise figure curves otherwise share the kink at around 15 MHz with the air core antenna noise figure curves, a kink that stems from the estimated equivalent noise temperature from Figure 2.40. It is interesting to note that there is not an apparent advantage to go from the single “big rod” to the bundle of 16 rods. It should be emphasized, however, that the estimate of the rod permeability of the bundle is very uncertain.

In Figure 2.55, the Q-factor for the ferrite considered antennas with ferrite material #61 cores are plotted. Since the resistance is dominated by the ferrite contributions, which is material dependent and proportional to the inductance, the Q-factor is almost independent of the shape of the antenna rod. At all frequencies the Q-factor is less than the bigger air core antennas considered in Figure 2.45, and above 10 MHz, the Q-factor drops rapidly. At around 40 MHz, the Q-factor drops below 1, which means that antenna hardly can be considered resonant any more.

In Figure 2.56 the product between the radiation resistance and the Q-factor is plotted. Note that this plot has limited relevance above around 40 MHz when the antenna no longer is resonant. Comparing for instance the 1”x12.3” ferrite rod antenna with the 2.5x30 cm² air core antenna, we

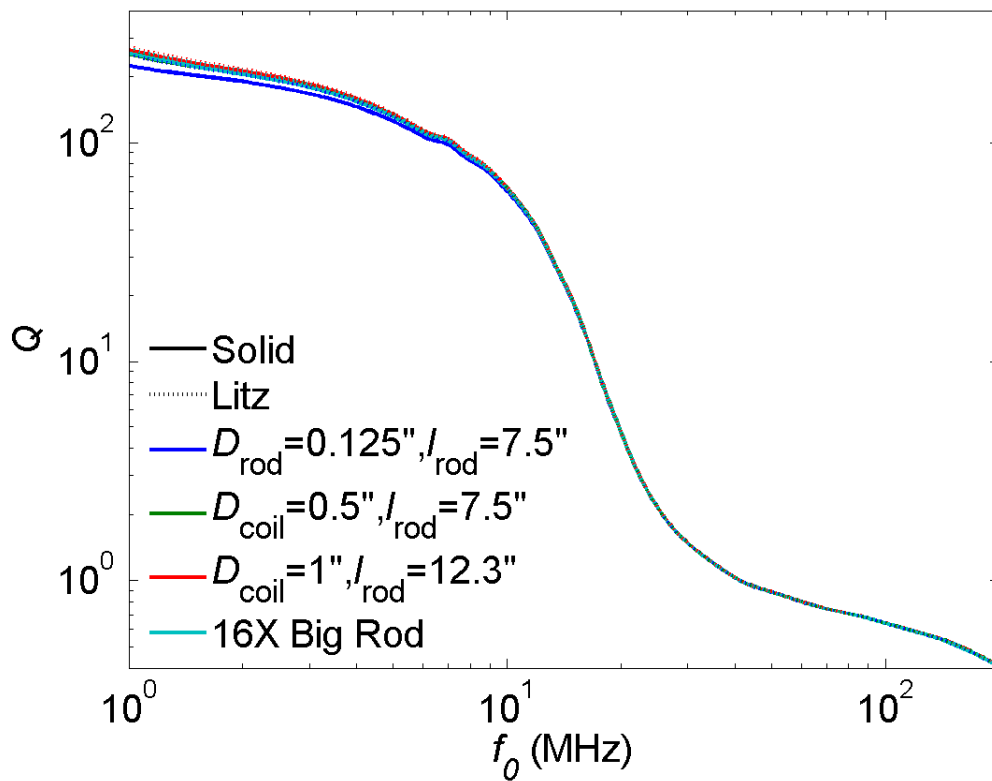


Figure 2.55 Similar to Figure 2.45, but just as for Figure 2.52 the plot of Q -factors is given for different types of ferrite core antennas.

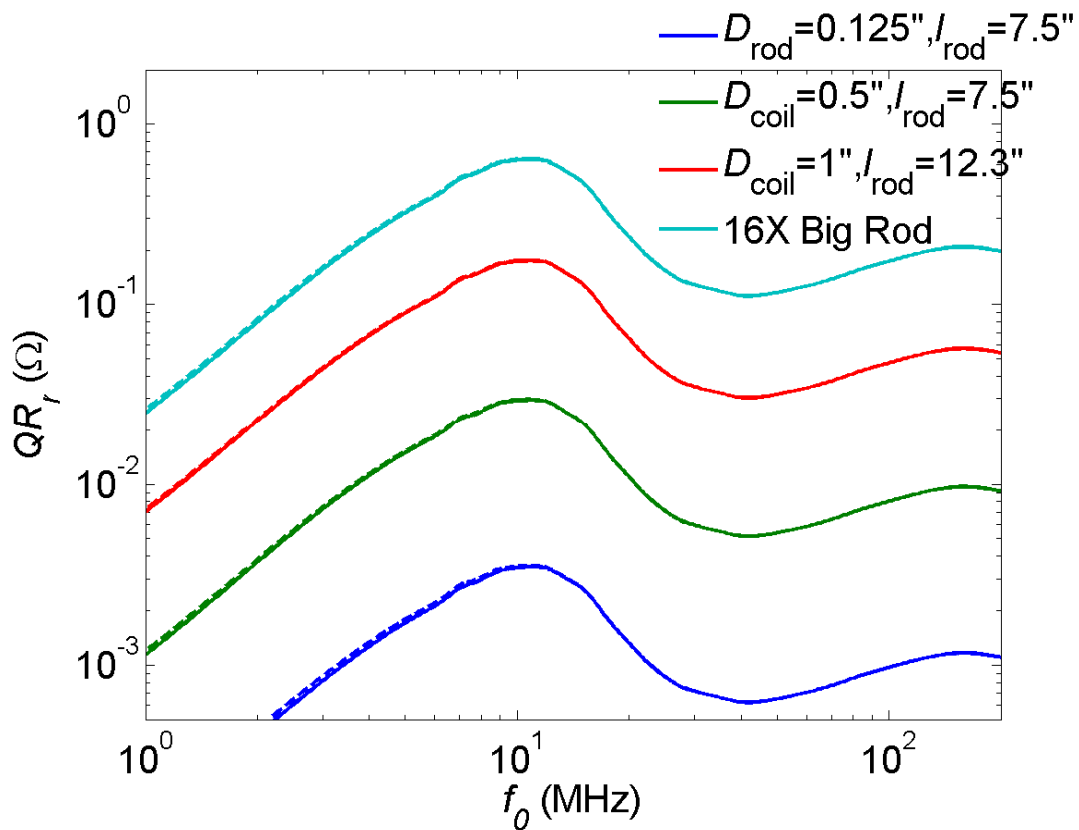


Figure 2.56 Similar to Figure 2.46, but for the same ferrite core antennas as in Figure 2.52.

see that the ferrite material #61 core antenna has a higher QR_r product than the similarly sized air-core antenna below 20 MHz.

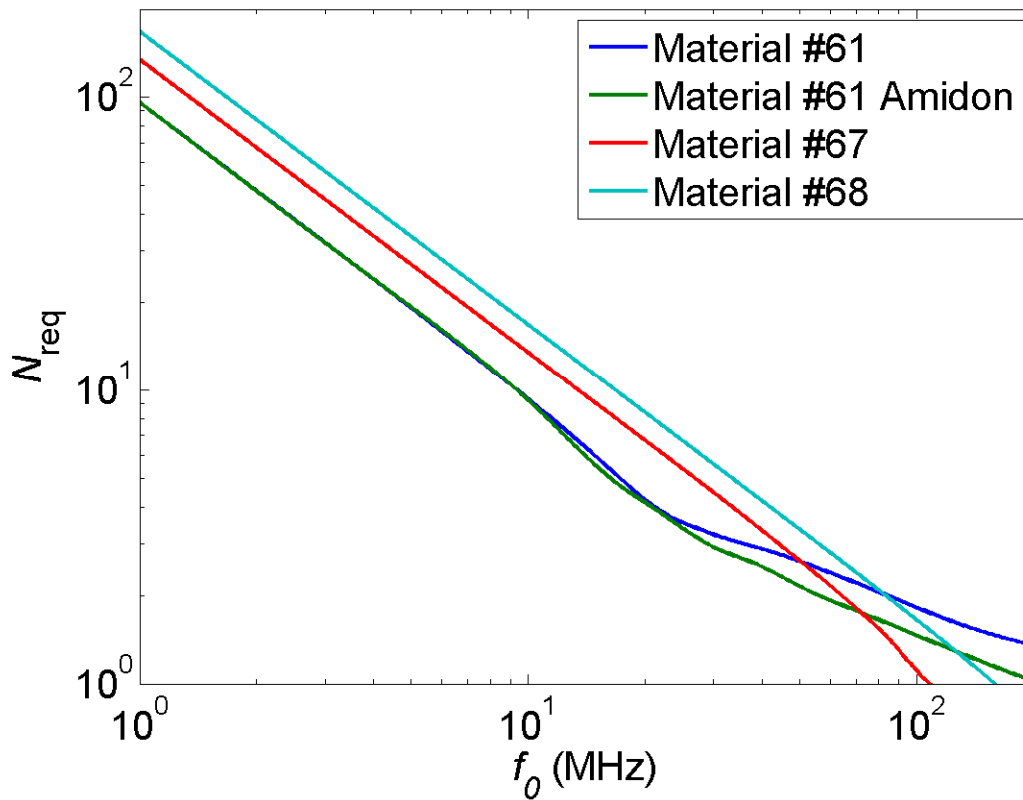


Figure 2.57 Required number of turns of ferrite core antennas of dimension $D_{\text{coil}} = 1''$ and $l_{\text{rod}} = 12.3''$, i.e. similar to Figure 2.42, but for different ferrite materials in the core.

In Figure 2.57 - Figure 2.61 the resistance values, the noise figure, the Q-factor and the QR_r product are compared between different Amidon / Fair-Rite rod antennas. From the above discussion regarding the material #61 antennas, the longest and biggest rod with dimension $D_{\text{coil}} = 1''$ and $l_{\text{rod}} = 12.3''$ is selected for this comparison between the ferrites. The bundle of rods had slightly higher performance, but the estimates for this antenna type were far more insecure. As mentioned above, the properties of the ferrite vary significantly with temperature, and mechanical history and make of the rod. Also the data sheet performance values vary quite a bit. Data sheet from the Amidon and Fair-Rite catalogs [24;25] are used to calculate the curves of Figure 2.57 - Figure 2.61. Amidon only provides plots of the relative loss factor, $\tan \Delta/\mu'$, and they do not extend as far up in frequency as the plots provided by Fair-Rite. The μ'' -data from Fair-Rite, on the other hand does extend as far down in frequency as the Amidon data. For the material #61, both the Amidon and Fair-Rite data covers the whole region of interest between 1 and 200 MHz. The data from the two catalogs are hence plotted as separate curves in the figures. For material #67 and #68, the Fair-Rite data plotted in Figure 2.50 and Figure 2.51 is used, but the Amidon data is used at the lower frequencies that the Fair-Rite catalog does not cover.

In Figure 2.57 the number of turns are plotted for the different materials, which of course shows that the materials with the lower permeability and hence inductance also needs the highest number of turns. Except at high frequencies, where the material is not very useful anyway, the Amidon and Fair-Rite data indicate similar permeability and hence required number of turns.

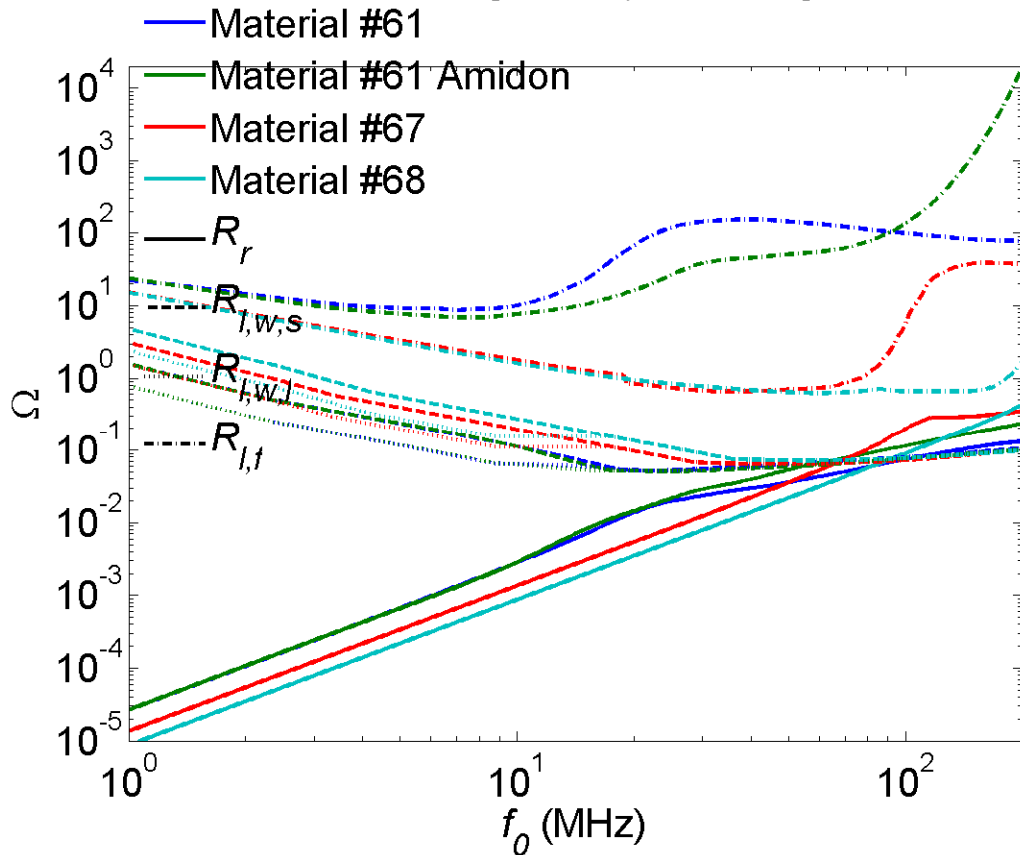


Figure 2.58 Antenna resistance values similar to Figure 2.43, but for different ferrite core antennas as in Figure 2.57

In Figure 2.58 the resistance values of the different material is plotted. At the lower frequencies, the ferrite loss of material #67 and #68 is similar, and lower than the ferrite loss of material #61. At around 80 MHz, the material #67 has a rapid increase to a higher loss regime. The similar transition of material #68 has only just started at 200 MHz, and thus has lower ferrite resistance than the other materials at the highest frequencies. For material #61, there is a slight difference in ferrite resistance from 8 MHz and above. Compared with the other ferrites, the radiation resistance is highest for material #61 below around 50 MHz, whereas the antenna with material #67 and eventually material #68 has the highest radiation resistance above 50 MHz.

The noise figure F plotted in Figure 2.59 has a similar trend. Material #61 has the lowest F -value below around 50 MHz, but the other materials have lower F above 50 MHz.

The Q-factor of the ferrite rod antennas made of different materials is plotted in Figure 2.60. Material #67 and material #68 has similar and constant Q-factors around 370 at most frequencies and higher Q-factor than material #61. Due to the increase in ferrite loss, the material #67 Q-

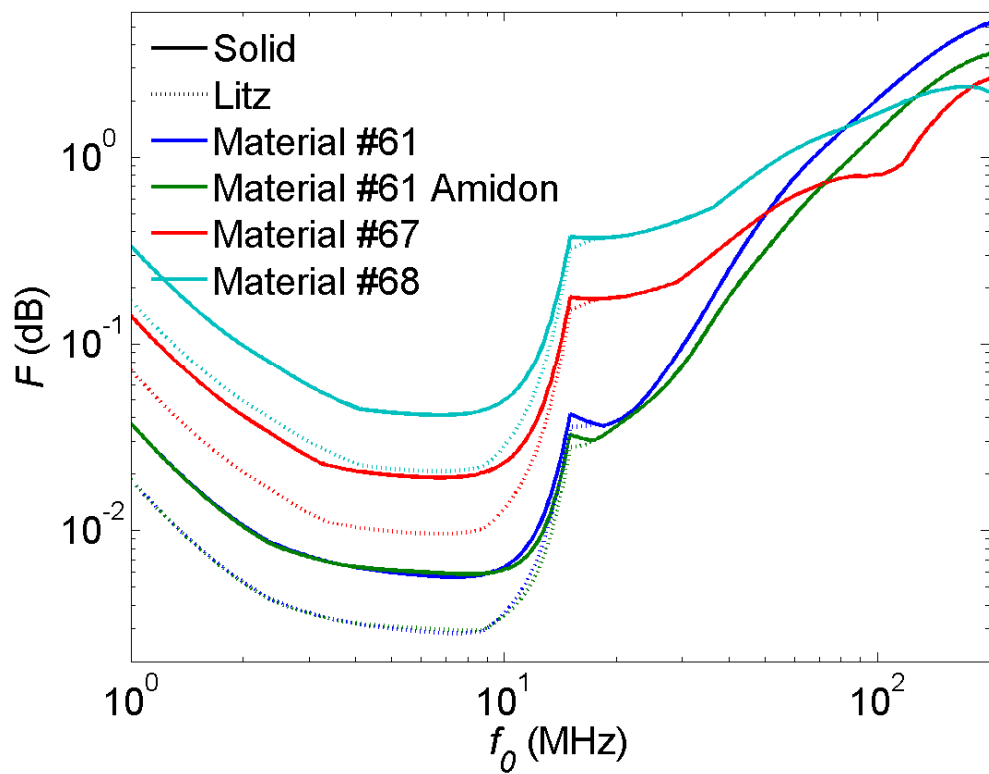


Figure 2.59 Antenna noise figure similar to Figure 2.44, but for different ferrite core materials as in Figure 2.57.

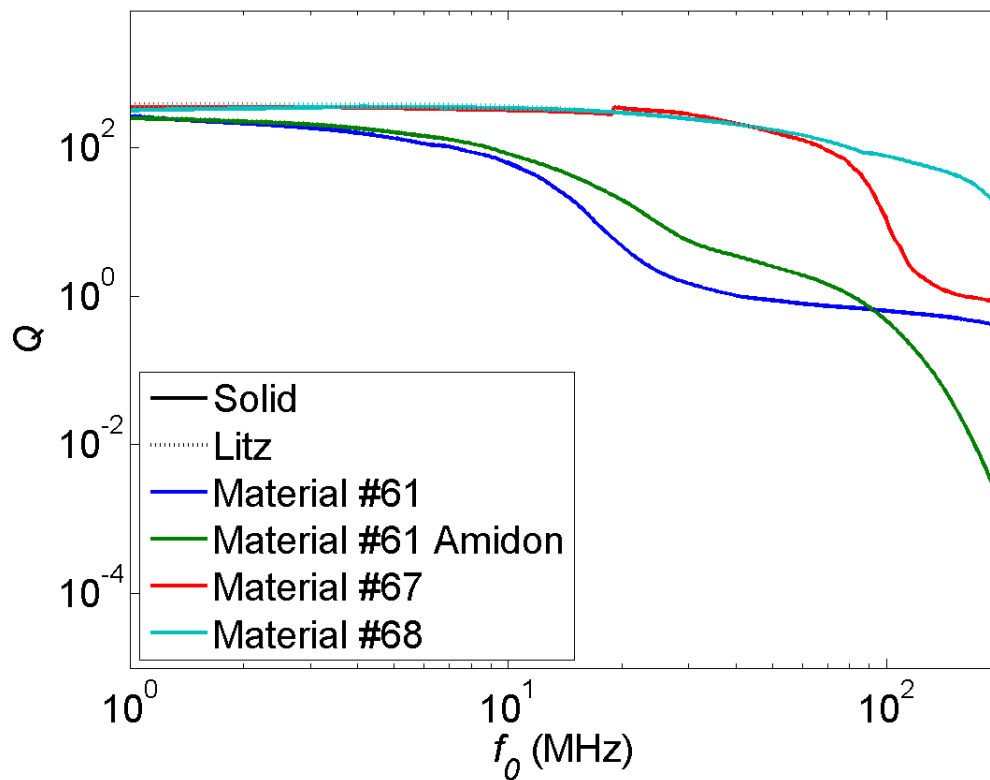


Figure 2.60 Antenna Q factors as in Figure 2.45, but for different ferrite cores as in Figure 2.57.

factor however starts to decline around 80 MHz, and becomes less than 1 around 160 MHz. Also the Q-factor of material #68 starts to decrease above around 170 MHz.

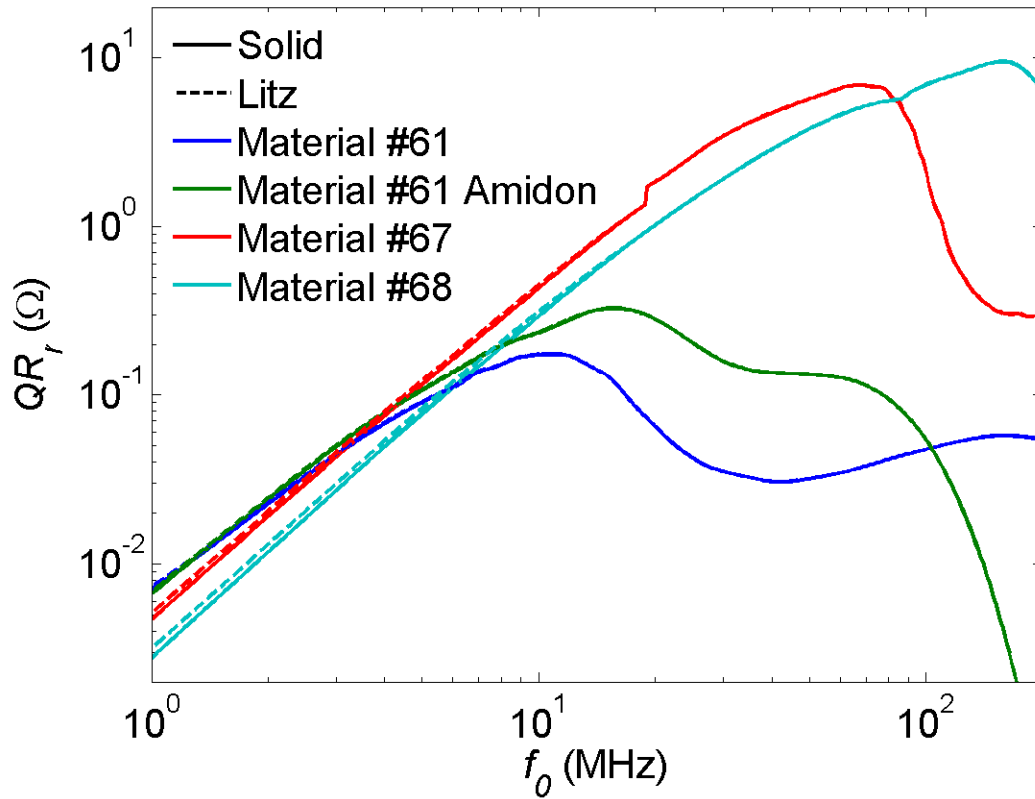


Figure 2.61 Antenna radiation resistance and Q-factor product, as in Figure 2.46, but for different ferrite core antennas as in Figure 2.57.

In Figure 2.61, the QR_r product of antennas made with different ferrite materials are compared. Again, we see that material #67 has acceptable performance at higher frequencies than material #61, and that material #68 works best at the highest frequencies in the range. Comparing with the similarly sized 2.5x30 cm circular air-core antenna, we see that the antenna made with ferrite material #68 works better than the air-core antenna at our whole frequency region of interest between 1 and 200 MHz. In most of the frequency interval, antennas with material #67 cores work better than antennas with material #68, but this is not the case above around 90 MHz.

Monopole Antenna

As discussed above, the alternative to a magnetic antenna with the solenoid axis in the shell plate is to have a monopole electric antenna perpendicular to but still behind the shell plate. A realistic maximum length of such antenna is only $l_{\text{monopole}} = 10$ cm, however. The radiation resistance of a simple monopole antenna is given by[29;30]:

$$R_{r,\text{monopole}} = \frac{\eta}{3\pi} \left(\frac{l_{\text{monopole}}}{\lambda_0} \right)^2 = 40 \left(\frac{\pi f_0 l_{\text{monopole}}}{c} \right)^2 \quad (2.94)$$

Here λ_0 is the wavelength of the radio wave and c is the speed of light. In Figure 2.62, the radiation resistance of a 10 cm long monopole antenna and a selection of other antenna types

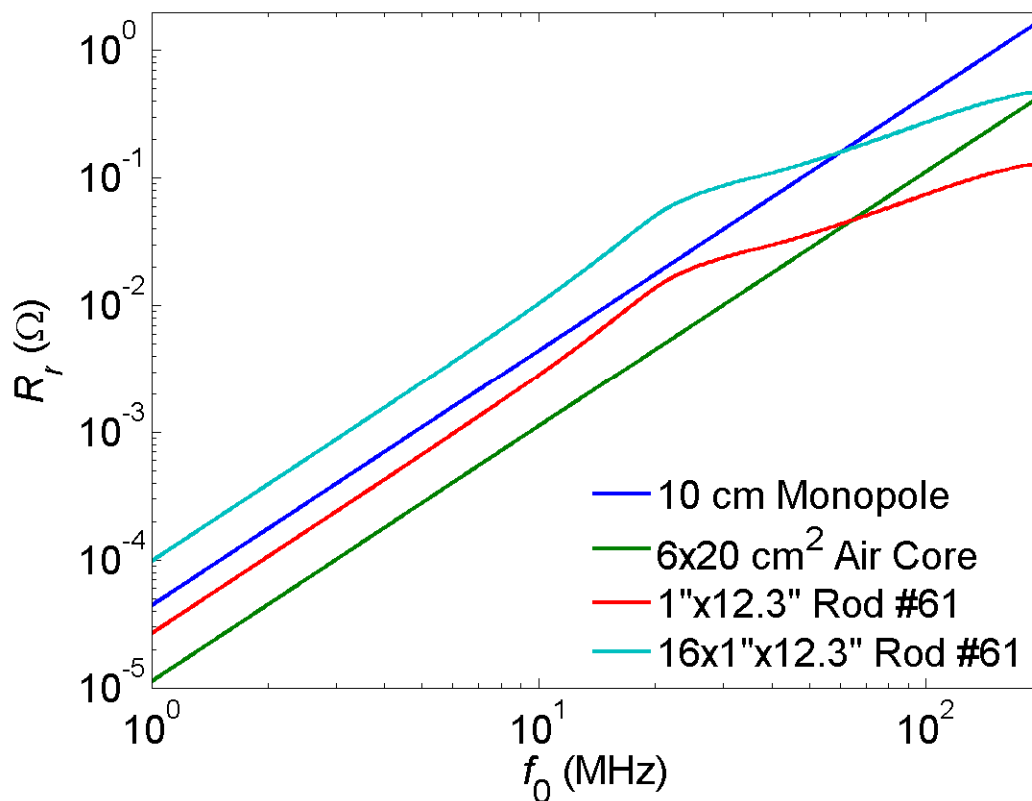


Figure 2.62 Radiation resistance of different compact antenna

of antennas discussed above is plotted as a function of frequency. Up to about 20 MHz, the radiation resistance of the monopole antenna is about half the radiation resistance of the magnetic antenna with a core consisting of a bundle of ferrite material #61 rods, about 50 % larger than the single ferrite rod antenna, and about 4 times larger than the largest air core magnetic antenna. However, the radiation resistance of a monopole antenna can be enhanced by capacitive top loading [22;29;30]. The losses of such antennas are dependent on the ground plane resistance, resistance in the surrounding dielectric and receiver circuitry, and time has not allowed for a detailed analysis of the performance of such antennas within this preliminary study, although a Q-factor as high as the magnetic antennas is probably not obtainable. An advantage with electric monopole antennas could however be that the availability of commercial antennas probably is better.

Transmitter Antenna

Whereas the receiver antennas along the hull have some space restrictions in all dimensions, these do not apply for the transmitter antenna on top of the bow. The simplest solution would probably be to use one of the receiver antennas also for transmitting, or to use some other commercial available antenna. It should be noted however, that ferrite materials are saturated and less efficient at high field strengths, such that the permeability of decreases. Thus ferrite rod antennas are only good transmitting antennas at low power levels. Regardless of the chosen antenna type, the antenna should be oriented in such that the transmitted signal matches the polarity of the antennas, i.e. with the magnetic field oriented parallel to the hull surface and of course

perpendicular to the desired transmission direction. I.e. for a loopstick antenna that means that the axis of the solenoid should be parallel to the sea and hull surface, whereas a whip antenna should be oriented parallel to the sea surface but orthogonally to the shell plates. Care should also be taken such that the antenna does not impair the stealth characteristics of the Skjold class. This may mean that the antenna should be placed behind the Skjold shell or deck plates.

2.4.2 Experimental Investigations

Preliminary tests of the principle were performed using various small AM and FM receivers, as well as avalanche rescue transceivers operating around 500 kHz. The receivers and transceivers were placed between the back of our Skjold class plate sample and a metal plate. The presence of the sea was simulated by placing a metallic surface against the other side of the shell plate. The receivers were listening passively to external signals. Both when testing the AM radio, which contained a ferrite antenna, and the FM receivers, the quality of the signal declined when sandwiched between the metallic plates. For the FM radio, operating around 100 MHz, this test was however quite difficult since the audio level is not proportional to the radio signal level. The investigated avalanche rescue transceiver, Mammut Pulse Barryvox, could both operate as a transmitter and receiver at 457 kHz. The units used ferrite antennas, and by operating in the so called analog mode, a direct indication of the received signal levels could be obtained. We tested a set of two such transceivers, the transceiver “buried” between the Skjold shell plate and the conducting back screen acted as a transmitter. The metal surfaces used in this test had an area of roughly 2 square meters, and the signal level detected at the receiving hand set was reduced by more than a factor of four when placing the transmitter between the two metal plates and the shell plate. Although these preliminary tests were promising, a more comprehensive test should be made using sea water at the other side of a much bigger section of shell plate, and using the preferred 1-200 MHz frequency range. Such a test could most easily be performed on board a ship from the Skjold class, but such a test is behind the scope of the current project.

2.4.3 Signature of the proposed sensor system

For use on the Oksøy/Alta class the major concern would be of magnetic signature. The air-core magnetic antenna and electric monopole antenna would not have any magnetic signature, but the high permeability of ferrite rod could be a problem. Consequently, a ferrite rod was sent to Magnetisk målestasjon, Skrogkontoret, FLO, in order to investigate the magnetic signature. An easily available rod was sent, Ferroxcube ROD10/200 4B1 with $D_{\text{rod}} = 200$ mm, $l_{\text{rod}} = 5$ mm and $\mu_r = 250$. Although the rod was more or less permanently magnetized by a saturating field, the magnetization was probably within acceptable limits [31], assuming that an array of roughly 10 rods would be used. By knocking a bit on the rod, however, the magnetization decreased with 50%. In a real system, the initial permeability, and hence magnetization, would be less by a factor of 2-25. At the same time, more ferrite material than anticipated in this characterization is needed if the biggest ferrite antennas discussed above. The question of magnetic signature should thus be investigated further

For the Skjold class, the radio signature is of more concern than the magnetic signature. However, at least for the first few km, the intensity of the radio signals decreases at least

inversely proportional to the square of the distance from the transmitter. I.e., at 5 km distance, the signal power is a factor 250 000 smaller than 10 m away from the transmitter. Hence, with reasonably efficient antennas in the receiving array, the transmitting signal can be turned down to a level where it is very difficult to detect at a distance. To further reduce the risk of enemy location of the emitter, a spread spectrum signal can be used. Finally, of course, the system may be switched off entirely in alert and warfare situations. In conclusion, we believe installation of the suggested system does not need increase the risk of location of the vessel by an enemy.

2.4.4 Alternative Configurations

So far only a configuration with a single transmitter and multiple receivers along the hull has been considered. An alternative configuration could for instance be to use an array of transmitter instead, which are switched on one at a time, and using a receiving antenna on top. The receiver antenna would not have the same space restrictions and could thus be made more sensitive, and by avoiding as much as possible to switch on radio transmitters above the sea water. Hence such a system could perhaps minimize the radio signature even further.

2.4.5 Conclusions Regarding Radio Attenuation Detection Array

Measuring the relative wave using a radio attenuation detection array as lined out above has several advantages compared with induction based system, in that we measure a signal produced by a first order rather than second order process. This means that the required transmitted power is significantly less, and the tolerances when constructing the receiver system significantly larger for the radio attenuation array vs. an induction based system. To cover all possible operation scenarios, the chosen frequency should be between 1 and 200 MHz. Considering the space constraints, maximum sensitivity, and hence minimum transmitted signal level, can probably being realized using some sort of magnetic loop antenna, although further studies and experience particularly regarding the electric antenna is needed. A magnetic antenna's performance may be enhanced using a ferrite core, but the ferrite has to be fitted to the chosen operation frequency. Further, even with careful packaging, the reliability of antennas with quite brittle ferrite components can be questioned. Probably none of the proposed realizations of radio attenuation detection arrays have a significant effect on the vessel signature. A possible exception is massive use of ferrite cores which may impair the magnetic signature of the Oksøy/Alta class vessels.

2.5 Directive RF/microwave reflectivity sensor

A well known technique to measure tank levels is to detect reflections from an RF/microwave transmission line along the tank wall. The difference in permittivity between air and water (or any other liquid) leads to a step in the capacitance, and hence impedance, of the transmission line, which again leads to a reflection of the RF/microwave signal. Conceptually, this measurement principle is not much different from the commercial microwave altimeters that have previously been tested in the project. However, when using a transmission line rather than free space to transmit the signal, you are guaranteed that the reflected wave is guided back to the detector.

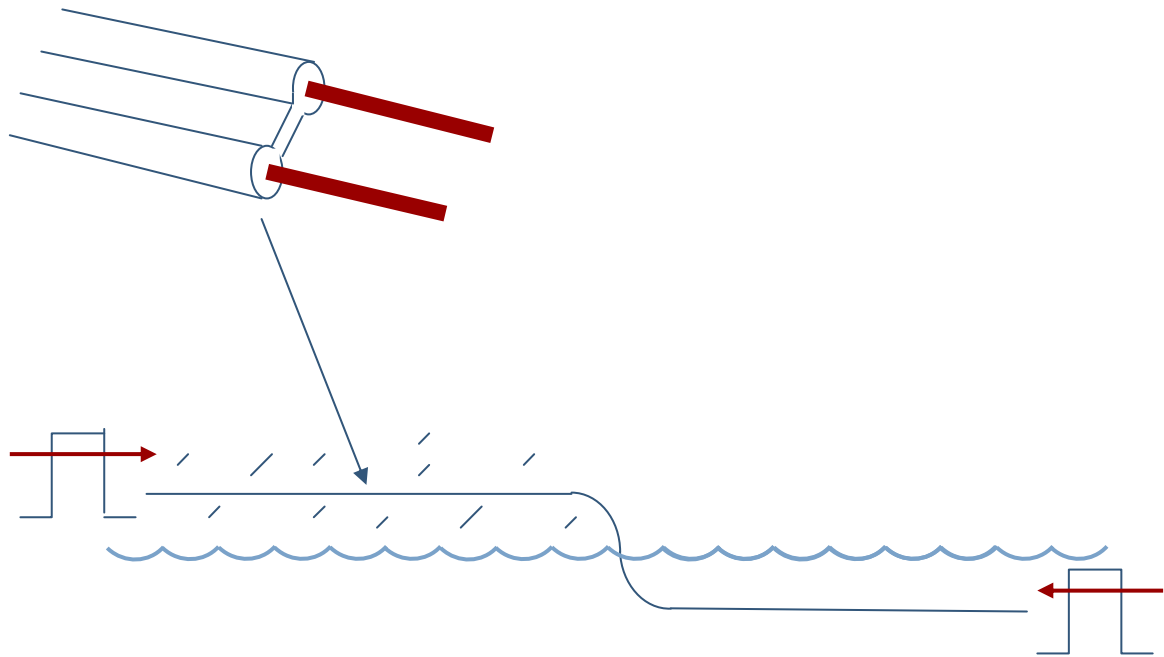


Figure 2.63 Measurement of the relative wave height using an RF/microwave transmission line. Left, the signal is transmitted (and reflection measured) from the air side of the water surface. Right, the signal is transmitted (and reflection measured) from wet side of the water surface.

In order to have a resolution of say $\Delta h \approx 20$ cm, the signal RF frequency needs to be higher than $c/\Delta h \approx 1.5$ GHz. The result can be obtained using either a pulsed techniques, which requires a rise time of less than 1 ns and corresponding high-speed electronics, or for instance a frequency modulation/mixing technique similar to the one used in the microwave altimeters from for instance Miros [1]. In any case, the distance between the conductors of the transmission line cannot be very large. Thus, following a similar argument as in Subsection 2.1.1, this measurement technique will to a certain degree be prone to measurement errors due to sea spray etc.

This technique was experimentally evaluated by partially submerging a dual wire ribbon cable into a plastic water pan, and interrogated using a commercial time-domain reflectometer for transmission line testing. It was confirmed that wetting the cable above the water surface may infer the measurements.

In conclusion, it seems that this technique does not have any obvious advantages compared to for instance a simple conductivity tests, but since the distance between the transmission line conductors is limited, this technique may be more inaccurate in difficult conditions.

3 Techniques based on static and acoustic pressure

3.1 Pressure sensor array

The idea here is to detect whether a point is above or below the water surface from a local pressure measurement. The pressure below the water surface around the bow is the sum of the hydrostatic pressure, given by water height above the point of measurement, and the stagnation pressure. The stagnation pressure is caused by the force exerted by the bow in order to accelerate and push away water as the ship is moving forward.

Mathematically, the hydrostatic pressure p_{hs} is simply given by:

$$p_{hs}(h-z) = \rho_w g \times (h-z) \approx 9.81 \text{ kPa/m} \times (h-z) \quad (3.1)$$

Here ρ_w is the density of water, g is the acceleration due to the gravity of earth, and h and z is still defined as in Figure 2.1. Hence, when the ship is at rest, a resolution of around 1 kPa is required by the pressure sensor in order to resolve a depth of $h-z = 0.1$ m.

The stagnation pressure is of course much harder to calculate, and would be a function of hull design, vessel velocity and the dynamic interplay between the ship and the sea waves. Fireco AS indicates that the stagnation pressure could be up to 250 kPa, and during wave slamming up to 1 MPa [32]. Thus, the stagnation pressure will probably dominate over the hydrostatic pressure in most sailing situations. Since the stagnation pressure value is not proportional to the water depth, the only reliable way we can measure the relative wave height is to use an array of discrete on/off sensors, which needs to have a resolution of around 1 kPa, but at the same time be able to sustain 1 MPa or more. Probably some low-pass filtering is needed in order to filter out sea spray impact.

Due to the relative high pressures involved and to avoid compromising the strength and stealthiness of the hull, the area of the pressure sensor exposed to the sea should be small. We suggest two ways of implementing a pressure sensor array. One solution is to use a similar technique as discussed in Subsection 2.1.2.2, and drill a hole through the hull right behind the sacrificial bow. This proposal is illustrated in Figure 3.1. Sensors with diameter of 1 cm and less with the required accuracy (1 kPa) as well as mechanical robustness (1 MPa) are available for instance from Kyowa. Even with an exposed sensor area of only 1 cm, 1 MPa however translates to a force of 78.5 N. Thus, in order to avoid that the pressure transducer is pressed through the plate, the sensor has to be anchored. One solution could be to mount the pressure sensor in a much bigger sleeve resting on the outside of the shell plate. However, such a sleeve needs to have quite a large diameter and would thus probably not be compatible for instance with the stealth specifications of the Skjold class. A better alternative is probably to anchor the sensor to an interior transverse bulk head, for instance the inner wall of the sacrificial bow as illustrated in Figure 3.2

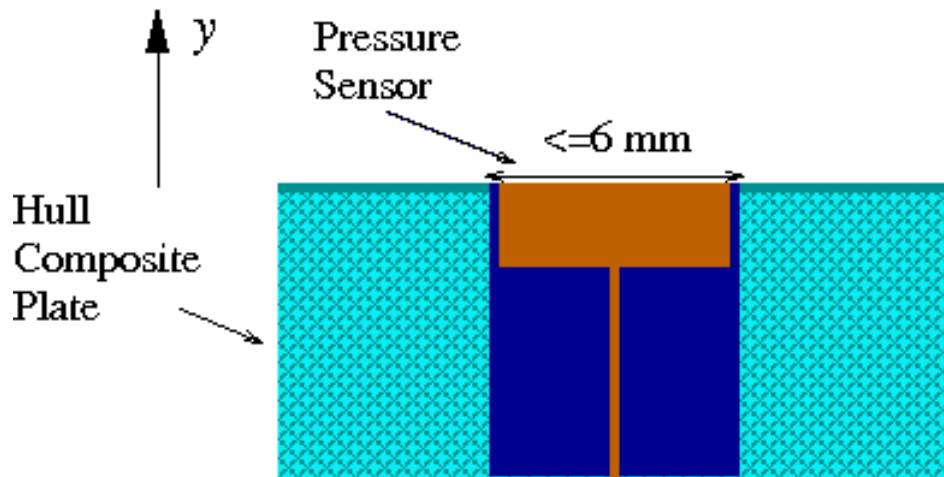


Figure 3.1 Example of pressure sensor embedded in the shell plate

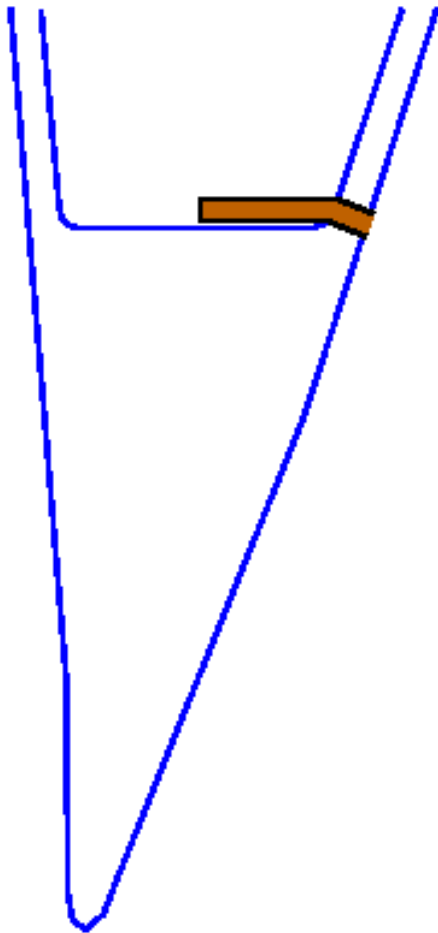


Figure 3.2 Anchoring of a pressure sensor right behind the sacrificial bow.

One disadvantage with mounting the pressure sensor through a shell plate behind the sacrificial bow as illustrated in Figure 3.1-Figure 3.2, is that the sensor would be exposed to the bow wave. Since the sensor, at least when using the simplest form of signal processing which flips from “above water” to “below water” at a pressure increase of only 1 kPa, the sensor would probably not measure the through relative wave but the rather unstable level of the bow wave at the hull

surface. An alternative pressure sensor method is thus illustrated in Figure 3.3. Here a whole is drilled through the sacrificial bow and lined by a pipe in order to protect the composite core material from water intrusion. The sensor itself is placed behind the sacrificial bow. As suggested by Fireco AS [33], the pipe should preferably be made in copper in order to avoid growth in the pipe. Since the pressure is measured at the front of the bow, the bow wave will not perturb the measurement to the same degree. The pipe will however introduce additional mechanical impedance between the sensor and the sea. There will probably also be some hysteresis in the system because the impedance will be different depending on the pipe water/air filling fraction. The mechanical impedance of the pipe will probably cause a delay as well as a reduction in bandwidth of the measurement. On the bright side, the maximum pressure levels at the sensor will probably also be reduced. The mechanical properties of such a pipe need to be studied further before a test installation of this system is made.

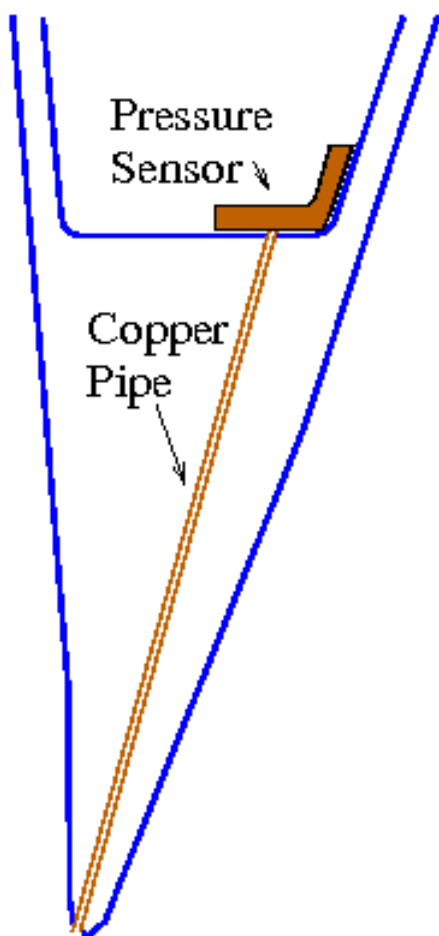


Figure 3.3 Pressure measurement behind the sacrificial bow with fluid mechanical contact with the front of the bow via a copper pipe.

Placing the pressure sensor inside the hull opens up the possibility for alternative measurement techniques. In some early studies of the project, some demonstrators of fiber optic pressure sensors were made. A typical example is illustrated in Figure 3.4. The wet side of sensor has a flexible membrane. As the pressure increases, the membrane is forced inwards, and the optical fiber behind the membrane is stretched. If there is a Bragg grating in the fiber, this strain can be

measured by the strain measurement instrumentation already available on both the Skjold and Oksøy/Alta class ships. The strain can be concentrated on the FBG by mechanical means, for instance by mounting the FBG on a flexible bridge that is narrowest around the grating. Although this is an interesting idea, it would probably be cheaper to commercially available pressure sensors instead of developing a custom one. More details about the fiber pressure sensor demonstrators can be found in reference [34]

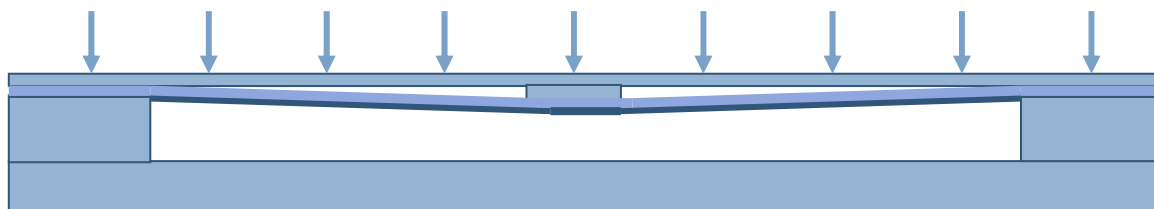


Figure 3.4 A demonstrated fiber optic pressure sensor [34]. The fiber is drawn in dark blue color.

A third type of measuring the pressure could be to mount new types of ultrathin pressure sensors shaped as tapes. Such solutions are supposedly under development in the JRP7, “Intelligent materials and production methods”, of the European network of excellence “Hydrotechnology Alliance” [35;36]

3.2 Subsurface acoustic techniques

A couple of commercial instruments for measuring distance in air has been tested and discussed in [1]. The major problem with acoustic sensors above air is robustness and that the signal will be screened by sea spray. Below water, acoustic transducers can be made more robust, i.e. with stiffer and sturdier membranes, and still maintaining good acoustic contact with the water, and below water the sea-spray problem will be eliminated. Just like an optical lidar system discussed below, an acoustic measurement probably should have a pulsed source. The pulse length should be around .2 ms or shorter, which means that the source probably should operate in the ultrasound domain. Since acoustic sources have much larger divergence than a laser, an acoustic antenna is probably needed in order to find the correct relative wave height. Although there is considerable competence in this area at FFI, the development of such a system probably would have a considerable expense. Another potential issue with such a sensor system when used on the Oksøy/Alta class is its acoustic signature.

4 Optical techniques

4.1 Reflectivity sensor

This technique was developed early in the project and utilized the fact that when light propagates through a material of high refractive index towards a material with lower refractive index, all the light will be reflected if the angle of incidence is larger than the so called critical angle, α_{crit} .

This critical angle is given by the well known formula derived from Snell’s law of refraction:

$$\sin \alpha_{\text{crit}} = \frac{n_2}{n_1} \quad (4.1)$$

Here n_1 and n_2 are the refractive indices of the material in which the incident beam propagates and behind the material interface, respectively. Thus, by measuring the critical angle, we can calculate the refractive index ratio between the materials. Since air has a refractive index $n_{\text{air}} \approx 1$ and water has a refractive of $n_{\text{sw}} \approx 1.33$ we can detect the presence of water by measuring the degree of reflection when the angle of incident is between the critical angles corresponding to air and water.

This simple principle was used to detect the presence of water. Small plastic prisms were used as reflective surfaces. A light beam was directed into the material by using multimode polymer fiber, as illustrated in Figure 4.1, and a similar fiber was used to collect reflected light at the other side of the prism. The core of the chosen fiber had a diameter of almost 1 mm. In the current context, the big advantage from using such a fiber is that the beam from the fiber is fairly collimated and has much larger core area than a conventional communications fiber, such that a sizeable amount of light reaches the sensing fiber in case of total reflection. In comparison, fiber transmitted from a cleaved surface of a conventional communication fiber has a high degree of divergence. An additional advantage of a polymer fiber is that it can easily be cut with an ordinary sharp knife, whereas special equipment is needed in order to cleave a conventional fiber optic glass fiber.

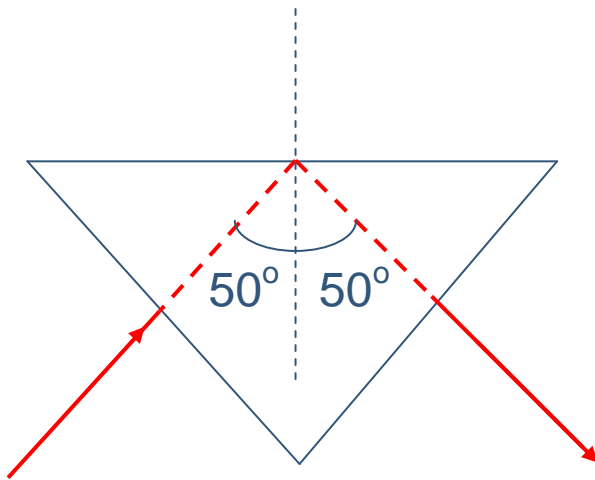
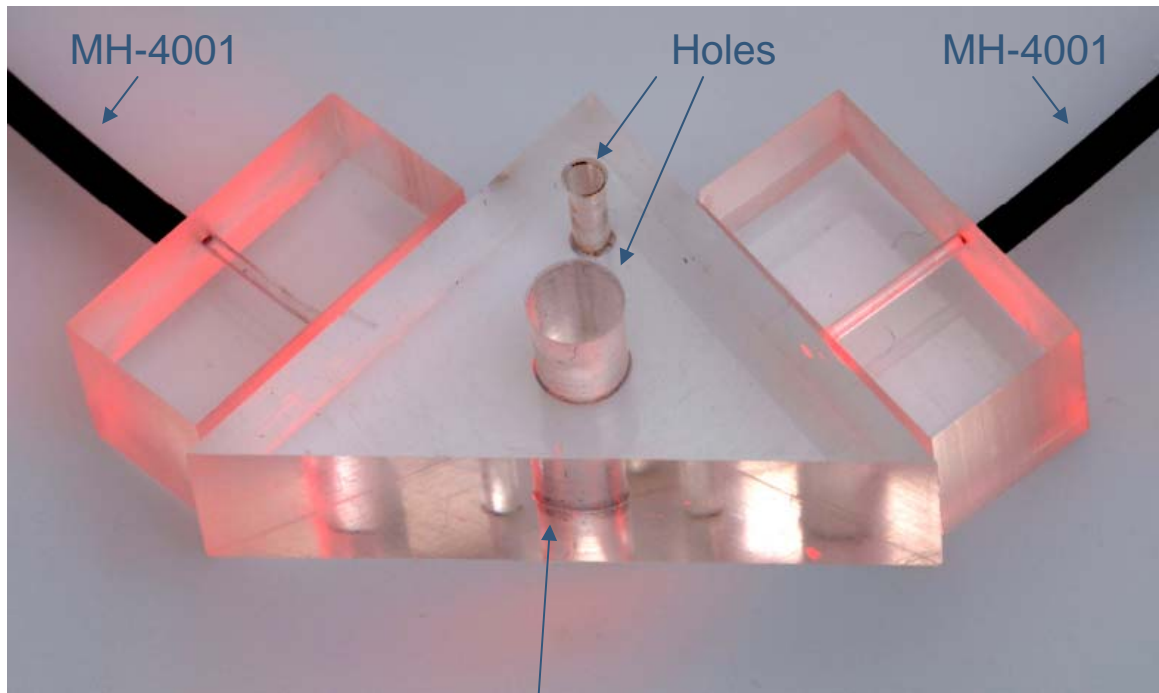


Figure 4.1 Sketched of the measurement principle suggested for the total reflection water sensor.

In Figure 4.2 a photo of one of the prisms is shown. In this case the plastic prism is made of polymethyl methacrylat (PMMA), which has a refractive index around $n_{\text{PMMA}} \approx 1.49$. The critical angle of a PMMA/water surface is thus $\alpha_{\text{crit}} \approx 63^\circ$, but only $\alpha_{\text{crit}} \approx 42^\circ$ at the interface between PMMA and air. Thus, the prism was made in such a way that the angle of incidence was around 50° , which in theory should give total reflection if there is air outside the reflective surface, but have a significant (and polarization dependent) transmission if the prism was below water. Several other prism shapes, as well as a different material (polycarbonate) was used. As is

evident in Figure 4.2, red light (650 nm wavelength) was used in the experiment. This is a convenient wavelength, as inexpensive diodes are available. At the same time, both the fiber polymere (PMMA) and sea water has relatively low loss at this wavelength.



Reflection Surface

Figure 4.2 A PMMA demonstrator total reflection water sensor.

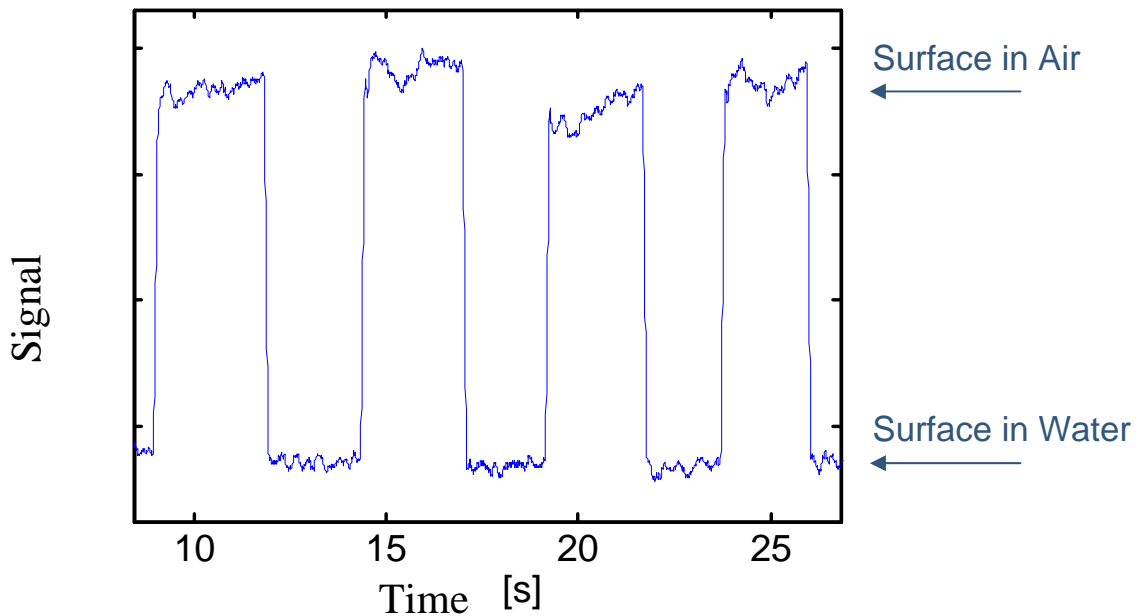


Figure 4.3 Measured detector signal of the PMMA prism illustrated in Figure 4.1-Figure 4.2. The prism is taken in and out of the water at a period of around 5 s, and the surface of the prism is scratched. The measurement is originally sampled at 200 Hz, and then downsampled to 10 Hz.

In Figure 4.3, a plot of the received signal at the output of the receiver circuit is plotted. The reflective surface of the sample under test was purposely scratched in order to simulate wear. The signal voltage with no light at the detector (bias) is between 10-20 mV, so the voltage level plotted in Figure 4.3 is approximately proportional to the optical power. As is evident from the plot, there is a decrease in received signal level when the prism is submerged in water, and the switching time is very short. That means that the sensor works even if the surface is wet, as in this case the outer surface of the water film act as the reflector. Both simple theory and experiments indicate that the use of smaller prisms give higher contrast. Further, the contrast may be increased somewhat by using increasing the diameter of the receiving fiber. More details about these experiments, also involving other prism shapes and materials, can be found in [37].

Even though this principle seemed to work both in theory and in the lab, the reliability of such a reflective sensor can be questioned, as the reflectivity of the surface probably will degrade as it is more worn, and particularly if it gets dirty or foul. Also the strength of the sensor from impact could be an issue, although they can probably be protected in a similar manner like the electrodes of the conduction sensors discussed in Subsection 2.1.2.2. These reliability of the sensors and possible enhancements of it thus has thus to be investigated further before we can conclude on the viability of the total reflection sensors. A further issue with these sensors is that it emits light at a relatively wide angle, which may compromise the stealth capabilities of the sensors. However, relatively little light is needed, and in bad weather, when the sensors are needed the most, the optical visibility is rather low. If needed, the relative wave sensors can of course be switched off at need or even automatically in nice weather.

In [38], a similar idea was presented to measure liquid levels in tanks, where the transmission was measured through a POF that was bent and side polished at several locations. This approach, however, cannot be directly used for the current application without some modifications.

4.2 Lidar

Lidar, also known as ladar, is a laser system equivalent to radar, where laser light is used for mapping and area or volume. Basically, it consists of a pulsed laser and a fast detector. By measuring the roundtrip time of reflected pulses, distances can be measured. Hence, the resolution of the lidar is given by the pulse length and detector bandwidth. In our case, where the desired resolution probably is around 0.2 m, the pulse length preferably should be shorter than roughly 1.3 ns and the detector should have a correspond bandwidth above 0.75 GHz. The maximum dynamic range and measurement frequency are inversely proportional to each other and is given by the pulse repetition rate. The dynamic range will of course in practice also be limited by the amount of light that is backscattered to the detector. Instead of just a point measurement, a line or an area can be mapped by scanning the laser beam, for instance by using an acousto-optic modulator. Thus, unlike all the other techniques discussed so far, it is possible using a lidar to get a complete mapping of the relative wave function in front of the bow, instead of just a point measurement.

There are many commercial available laser instruments that measure the distance and speed of objects, for instance the instruments used by the police world-wide in order to clamp down on speeding. However, most of these instruments, which typically are meant to operate in air, cannot easily be used to measure relative waves. The main reason is that sea spray easily will obscure the view of the instrument. To a certain degree it could in most cases be possible to “see through” the sea spray by using an algorithm that looked for the last reflective surface (i.e. sea surface) and by scanning the beam. Just like for the microwave altimeters tested previously by FFI [1], shallow reflective angles may be another problem, however, since most of the light then would be directed away from the ship and the detector. This problem can partly be solved by using green light which is scattered by plankton and other small particles and air bubbles of the sea [39]. Above water, water on the optical surfaces may impair the lidar performance.

The best technical solution for a lidar system would in our case probably be to place the lidar at the bow close to the keel, and direct the laser beam towards the surface and scan it in a line in front of the vessel. Then sea spray will no longer be an issue, as little light will penetrate the sea surface twice. Further, even if the angle of the sea surface is such that there is no specular reflection back to the detector, there will still be back-scattering from plankton, other particles, and air bubbles below the sea surface, particularly when using green light. Thus, making robust algorithms to measure the distance to the sea surface is probably much easier if the lidar is placed under water instead of above it. A further benefit with using an underwater lidar is that light leakage will be minimum and probably not detectable by other vessels.

There are several lidar systems in service around the world that are used for sea and wave surveillance [40;41]. However, almost all of these systems are airborne, where sea-spray is not a big issue and the laser beam has close to orthogonal incident to the sea surface. The only exception that was found was the 532 nm system described in [39]. However, according to the University of Exeter who developed this lidar, their system is not applicable for our requirement (short range/high resolution). There are a few providers of submarine lidar systems, notably [41]. However, in the end, a lidar used for relative wave measurement probably has to be tailor made by a commercial lidar company or developed at FFI. There has for many years been lidar activities at FFI, so the latter may be the most cost-efficient solution. In any case, such a lidar would require a relative extensive effort in hardware and software/algorithm development. In addition, the component cost would be quite high. Only a pulsed 532 nm laser, for instance as presented in [42;43], will cost between 70 000 and 150 000 NOK.

4.3 Triangulation

4.3.1 Triangulation above surface

It has been suggested to use triangulation, where the detector and for instance a scanning laser beam is placed some distance from each other. The distance down to the water surface is thus found by measuring the laser angle where the detected light is maximized. This idea has not been pursued any further because it may suffer from the same problems regarding sea spray and

specular reflection away from the ship as the lidar and ultrasound, but without the possibility like in lidar to filter away for instance sea spray and find the real surface.

4.3.2 Triangulation below surface

One commercial solution has been found for subsurface triangulation, the Tritech Typhoon VMS [44]. It is based on a set of 5 red laser diodes and a video camera. However, according to Tritech, there is no way that this instrument could operate at the frequencies we need in order to measure relative waves, as a measurement may take minutes. Of course, under water we can also use the same technique as described in Subsection 4.3.1. However, such a system would in both cases have the same problems when the light is reflected away from the ship.

5 Conclusions

Wave diving may pose a serious risk to crew safety and hull integrity on the new Skjold class fast patrol boats. The plan is to develop a warning system to prevent such incidents by analyzing data from the inertial navigation system (INS). However, it is expected that measurements of the distance between the wet deck and sea surface, i.e. the relative wave, will improve the reliability of such a warning system.

We have explored a range of different techniques for measuring the relative wave in front of the Skjold- and Oksøy/Alta class ships, utilizing the electromagnetic, mechanical, and optical properties of sea water. The techniques have been evaluated both regarding their technical potential, signature, and complexity/price. The techniques that seem most promising from a technical point of view is the measurement of conductance between pairs of electrodes, measurement of radio attenuation profile using an array of antennas, measurement of pressure along the hull and submarine lidar. Of these techniques, lidar is the only technique that is capable of measuring the whole wave profile in front of the ship, but the development of a lidar system is probably way to expensive for the current application. If a relative wave sensor is needed, we instead recommend further experimental investigations, including sea trials with one of the Skjold class ships, with two of the other techniques, pressure sensors and radio attenuation array. As a start, it would of course suffice to only use a limited number of sensors instead of a full array.

None of the most promising techniques mentioned in the preceding paragraph are expected to be detrimental for either the Skjold- or Oksøy/Alta class. The biggest worry is perhaps if ferrite has to be used in the antennas of the radio attenuation profile measurement system, as these have very high permeability and hence could affect the magnetic signature of the Oksøy/Alta class. Preliminary investigations however indicate that the magnetic signature still will be within acceptable limits.

References

- [1] S. W. Løvseth, H. E. Torkildsen, A. Kleivstul, and A. Skaugen, "Air gap measurements between the wet deck of SES vessels and sea surface using microwave and ultrasound altimeters," FFI Report 2007/02067, Sept.2007.
- [2] G. W. C. Kaye and T. H. Laby, *Tables of physical and chemical constants*, 16 ed. Harlow, United Kingdom: Longman, 1995.
- [3] A. Pfaffling, "Electromagnetic Methods to Measure Sea-Ice Thickness," Bremerhaven, Germany: Alfred-Wegener-Institut für Polar- und Meeresforschung, http://www.awi.de/fileadmin/user_upload/Research/Research_Divisions/Climate_Sciences/Sea_Ice_Physics/pdf_poster/apfaffling_2003_1.pdf, 2003.
- [4] "QProx™ QT113 / QT113H CHARGE-TRANSFER TOUCH SENSOR," Quantum Research Group Ltd., http://www.qprox.com/assets/downloadablefile/qt113_105_15457.pdf, 2008.
- [5] A. V. Räsänen and A. Lehto, "Transmission Lines and Waveguides," in *Radio engineering for wireless communication and sensor applications* Boston, MA, USA: Artech House, 2003.
- [6] L. A. Klein and C.T.Swift, "An improved model for the dielectric constant of sea water at microwave frequencies," *IEEE Trans. Ant. Prop.*, vol. 25, no. 1, pp. 104-111, 2008.
- [7] J. Johnson, "Thermal Agitation of Electricity in Conductors," *Phys. Rev.*, vol. 32, p. 97, 1928.
- [8] H. Nyquist, "Thermal Agitation of Electric Charge in Conductors," *Phys. Rev.*, vol. 32, p. 110, 1928.
- [9] G. H. Tan and C.Rohner, "The Low Frequency Array active antenna system," in *Proc.SPIE*, vol. 4015, SPIE Conf. on Radio Telescopes: Munich, Germany, 2008.
- [10] P. L. Dowell, "Effects of eddy currents in transformer windings," *Proceedings IEE*, vol. 113, no. 8, pp. 1387-1394, Aug.1966.
- [11] X. Nan and C.R.Sullivan, "An improved calculation of proximityeffect loss in high frequency windings of round conductors," vol. 2, 34th Annual IEEE Power Electronics Specialist Conference: IEEE, 2003, pp. 853-860.
- [12] X. Nan and C.R.Sullivan, "Simplified High-Accuracy Calculation of Eddy-Current Loss in Round-Wire Windings," vol. 2, 35th Annual IEEE Power Electronics Specialists Conference: IEEE, Aachen, Germany, 2004, pp. 873-879.
- [13] E. Fraga, C. Prados, and D.-X. Chen, "Practical Model and Calculation of AC Resistance of Long Solenoids," *IEEE Trans Magnetics*, vol. 34, no. 1, pp. 205-212, Jan.1998.
- [14] A. W. Lotfi and F. C. Lee, "A high frequency model for Litz wire for switch-mode magnetics," vol. 2, 1993 IEEE Industry Applications Society Annual Meeting: Toronto, Canada, 1993, p. 1175.

- [15] C. R. Sullivan, "Optimal Choice for Number of Strands in a Litz-Wire Transformer Winding," *IEEE Trans Magnetics*, vol. 14, no. 2, pp. 283-291, Mar.1999.
- [16] "Effect of Parasitic Capacitance in Op Amp Circuits," Texas Instruments, 2000.
- [17] G. Grandi, M.K.Kazimierczuk, A.Massarini, and U.Reggiani, "Stray Capacitances of Single-Layer Solenoid Air-Core Inductors," *IEEE Trans Industry Appl.*, vol. 35, no. 5, pp. 1162-1168, Sept.1999.
- [18] R. H. M. Poole, "Ferrite Rod Antennas for HF?," BBC R&D White Paper, British Broadcasting Corporation,WHP 091, July2004.
- [19] B. H. Tongue, "About Maximizing the Q of solenoid inductors that use ferrite rod cores, including charts of magnetic flux density and flux lines, with some actual Q and inductance measurements from simulations in FEMM," Ben Tongue technical papers, <http://www.bentongue.com/xtalset/29MxQFL/29MxQFL.html>, 2008.
- [20] R. L. Cross, "Ferrite Rod Receiving Loop Antenna Analysis and Modeling," http://raylcross.net/murod_mm/index.html, 2007.
- [21] D. McGillis, "Calculating the Inductance of a Ferrite Rod-Cored Coil and Selecting a Wire Size," Visitors Technical Articles. Dave Schmarder's home made radios, http://www.schmarder.com/radios/tech/files/Ferrite_Rod_Inductance.pdf, 2006.
- [22] *The ARRL Antenna Book*, 18 ed. Newington, Connecticut, USA: American Radio Relay League, 1997.
- [23] "Ferrite Rod Antennas for RF-identification Transponders," Application Note Philips Magnetic Products, Philips Components,2008.
- [24] "Iron-Powder and Ferrite Coil Forms.....," Amidon Associates, 2000.
- [25] "Online Catalog," Fair-Rite Products Corp., <http://fair-rite.com/cgibin/catalog.pgm>, 2008.
- [26] "Online Product Catalogue," MMG Canada, <http://www.mmgca.com>, 2008.
- [27] "Soft Ferrites and Accessories," Ferroxcube International Holding B.V., <http://www.ferroxcube.com>, 2004.
- [28] "Long and Thick Ferrite Rods," www.stormwise.com, <http://www.stormwise.com/page26.htm>, 2008.
- [29] H. A. Wheeler, "Fundamental Limitations of Small Antennas," *Proc. IRE*, vol. 35, no. 12, pp. 1479-1484, Dec.1947.
- [30] T. L. Simpson, "The Disk Loaded Monopole Antenna," *IEEE Trans. Ant. Prop.*, vol. 52, no. 2, pp. 542-550, Feb.2004.
- [31] T. Ingebregtsen, "E-mail: Magnetiske målinger av ferittstav ifm. optisk skrogovertvåkning mineryddere,". S. W. Løvseth, Ed. 2007.
- [32] A. E. Jensen, "E-mail,". S. W. Løvseth, Ed. 2007.
- [33] Jensen A.E., "Personal communication," 2007.

- [34] Kleivstul, A., "Braggitterbasert sensor for registrering av trykkendringer", Powerpoint presentation available from FFI at request, 2007
- [35] K. A. Hegstad, "Private communication," 2007.
- [36] "Hydrotechnology Alliance - European network of excellence," www.hta-noe.eu, 2008.
- [37] Kleivstul, A., "Snellsensorer", Powerpoint presentation available from FFI at request, 2007
- [38] M. Lomer, A. Quintela, M. López-Amo, J. Zubia, and J. M. López-Higuera, "A quasi-distributed level sensor based on a bent side-polished plastic optical fibre cable," *Measurement Science & Technology*, vol. 18, pp. 2261-2267, June 2007.
- [39] J. M. K. Horwood, R. W. F. Thurley, M. R. Belmont, and J. Berg, "Shallow Angle LIDAR for Wave Measurement," vol. 2, *Oceans - Europe 2005: 2005*, pp. 1151-1154.
- [40] "Optech - a leading company in the lidar industry," www.optech.ca, 2008.
- [41] "Areté Associates," www.arete.com, 2008.
- [42] "High Peak Power High Repetition Rate Sealed Q-switched 1064 & 532nm Microchip Laser - SNP/SNG series," teem photonics, www.teemphotonics.com, 2008.
- [43] "High Peak Power High Repetition Rate Sealed Q-switched 1064, 532 & 355nm PowerChip Laser - **PNP/PNG/PNV series**," teem photonics, www.teemphotonics.com, 2008.
- [44] "Typhoon VMS Video Measuring System," Tritech International Limited, www.tritech.co.uk, 2008.